Fermilab

FERMILAB-THESIS-2002-17

Theodore Vidnovic III

108 Words

Di-Neutral Pion Production in the Triplet P-Wave States of Charmonium

Fermilab experiment E835 has used proton-antiproton annihilations to perform a search for charmonium in the $\pi^0\pi^0$ final state in the triplet P-wave region (3340-3570 MeV). States with even total angular momentum and positive Parity and C-parity have access to the $\pi^0\pi^0$ final state. An enhancement in the $p\bar{p} \to \pi^0\pi^0$ cross section was observed at the χ_{c0} resonance. The enhancement was found to be a factor of 20 larger than the expected resonant cross section and was attributed to interference between the χ_{c0} and the large non-resonant continuum. The general helicity structure of the $\pi^0\pi^0$ differential cross section was studied and the product of the branching fractions, $Br(p\bar{p} \to \chi_{c0}) \times Br(\chi_{c0} \to \pi^0\pi^0) = (5.09 \pm 0.81_{stat} \pm 0.25_{sys}) \times 10^{-7}$ was measured.

UNIVERSITY OF MINNESOTA

This is to certify that I have examined this bound copy of a doctoral thesis by

Theodore Vidnovic III

and have found that it is complete and satisfactory in all respects and that any and all revisions required by the final examining committee have been made.

Professor Roger W. Rusack
(Faculty Adviser)

GRADUATE SCHOOL

Di-Neutral Pion Production in the Triplet P-Wave States of Charmonium

A THESIS
SUBMITTED TO THE FACULTY OF THE GRADUATE SCHOOL
OF THE UNIVERSITY OF MINNESOTA
BY

Theodore Vidnovic III

IN PARTIAL FULFILLMENT OF THE REQUIREMENTS
FOR THE DEGREE OF
DOCTOR OF PHILOSOPHY

December, 2002

Di-Neutral Pion Production in the Triplet P-Wave States of Charmonium

by Theodore Vidnovic III

Under the supervision of Professor Roger W. Rusack

ABSTRACT

Fermilab experiment E835 has used proton-antiproton annihilations to perform a search for charmonium in the $\pi^0\pi^0$ final state in the triplet P-wave region (3340-3570 MeV). States with even total angular momentum and positive Parity and C-parity have access to the $\pi^0\pi^0$ final state. An enhancement in the $p\bar{p} \to \pi^0\pi^0$ cross section was observed at the χ_{c0} resonance. The enhancement was found to be a factor of 20 larger than the expected resonant cross section and was attributed to interference between the χ_{c0} and the large non-resonant continuum. The general helicity structure of the $\pi^0\pi^0$ differential cross section was studied and the product of the branching fractions, $Br(p\bar{p} \to \chi_{c0}) \times Br(\chi_{c0} \to \pi^0\pi^0) = (5.09 \pm 0.81_{stat} \pm 0.25_{sys}) \times 10^{-7}$ was measured.

Dedication

For Pappap, Mom, Dad, and Kat

Acknowledgements

First, I would like to thank my advisor, Roger W. Rusack for the advice and guidance he provided throughout my graduate school career. Roger gave me the opportunity to explore new places and learn new things as well as allowing me the freedom I needed to develop into a scientist. For that, I will always be grateful. I would also like to thank Dieter Dehnhard for giving me, a new graduate student, a summer research assistantship, before you ever met me.

The people who put their hearts and souls into E835 have also helped me tremendously over the years. Particularly, I would like to thank Stephen Pordes, Jason Kasper, Keith Gollwitzer, Michelle Stancari, Rosanna Cester, Paolo Rumerio, and Jerry Rosen. Without your guidance and friendship, the completion of this work would not have been possible. Additionally, Margherita Obertino, Nadia Pastrone, Roberto Mussa, Giulio Stancari, Claudia Patrignani, Matteo Negrini, Gianluigi Cibinetto, Wander Baldini, Peter Zweber, and David Joffe have all become trusted colleagues and great friends. Although I have left many names out, the entire E835 collaboration is a credit to science and I hope to have the opportunity in the future to work with people as dedicated as you all are.

Thanks also goes to the other members of my group. Over the years, Matt Graham and Seon Hee Seo have helped me really understand what it is that I was doing. Without having to explain my work and learn about your work, I would have been lost in the quagmire of my analysis. Additional thanks goes to Long Duong, who has been a wonderful sounding board. Without Kenichi Torikoshi, Ágnes Mócsy, Aaron Wynveen, Henry Juengst, and Jefferson Bjoraker, I would have never been able to make it through my first few months, let alone 4+ years in graduate school. You guys are the best office mates that anyone could ever wish for. My graduate school experience would also not have been the same without

Luis Hernandez, Heather Brown, Alex Smith, Ron McNabb, Ben Bousquet, and Emily Maher.

I would like to thank my all of my professors at The University of Minnesota and St. Vincent College for the education that they provided. Especially, M. Anis Maize, John Smetanka, Michael Gainer, Douglas Smith, Fr. Thomas Hart, Ben Bayman, Yutaka Hositani, Misha Voloshin, Arkady Vainstein, Misha Shifman, Ken Heller, Oriol Valls, Keith Olive, John Urheim, and J. Woods Halley.

Throughout my life I have encountered many great people who I have learned a great deal from. The most important of these people were present and active in my life during a difficult and awkward time. I will never forget the many words of encouragement that you have spoken to me over the years, so thank you P. George Zober, Dennis Gaal, Maureen Fleck, and especially Andy and Bonnie Kasic.

What can I say about the fellas? Whenever I need a reality check you are always ready, willing, and able, even though the hangovers hurt more than they used to. My Real Team: Cecil H. Jarmon II, Square, Kosmo, Kitsko, The Gimp, and Larry G. Thanks guys.

My grandfather, Theodore Vidnovic Sr. was never afraid to do what he though was right, no matter what other people thought. Pappap, even though I didn't get to know you very well, I not only carry your name, I also carry your spirit. For this and so much more, I give credit to my parents, Maureen and Theodore Vidnovic Jr. You are always there to pass on your innate ability to think your way through any situation, good or bad. You support and believe in me, even when I didn't believe in myself. The basic common sense that I learned from you I have always credited as my most precious possession. Furthermore, you have spent your lives making mine better, for this, thanks is not enough.

The support that my wife Katrina has given me in the last 4+ years has made all the work of graduate school well worth it. I am indebted to Kat for the logistical support that she provided during my preparation for the oral exam and during the writing of this dissertation. The moral support that she continues to give me is invaluable. Above all else, having you to spend my life with is what I'm most grateful for. I never dreamed I would find somebody that would completely understand me, but you have.

Curriculum Vitae

Education

2002	**University of Minnesota, Minneapolis, Minnesota** Ph. D. in Physics *Dissertation:* "Di-Neutral Pion Production in the Triplet P-Wave States of Charmonium" *Advisor:* Roger W. Rusack
1998	**St. Vincent College, Latrobe, Pennsylvania** B.S. in Physics *Senior Thesis:* "The Bound to Bound State Contribution to the Electric Polarizability of a Relativistic Particle" *Advisor:* M. Anis Maize

Publications

S. Bagnasco *et al.* [Fermilab E835 Collaboration], "New Measurements Of The Resonance Parameters Of The $\chi_{C0}(1^3P_0)$ State Of Charmonium," Phys. Lett. B **533**, 237 (2002).

C. Patrignani, *et al.* [E835 Collaboration], "E835 At Fnal: Charmonium Spectroscopy In Anti-P P Annihilations," Nucl. Phys. A **692**, 308 (2001).

Presentations

"Di-Neutral Pion Production in the $\chi_c 0(^3P_0)$ State of Charmonium," Speaker: Fifth International Conference on Quark Confinement and the Hadron Spectrum, Gargnano, Italy, September, 14, 2002.

"E835: The Charmonium Experiment at Fermilab," Contributed poster at a United States Department of Energy Review, Batavia, Illinois, March 2001.

"Charmed," Speaker: Department of Physics Colloquium, St. Vincent College, Latrobe, Pennsylvania, January 2001.

"The Bound to Bound State Contribution to the Electric Polarizability of a Relativistic Particle," Contributed poster at Joint APS/AAPT Meeting, Columbus, Ohio, April 1998.

Professional Activities

Research Assistant, University of Minnesota, 1998,2000-Present
Teaching Assistant, University of Minnesota, 1998-2000
Teaching Assistant, St. Vincent College, 1995-1998
Director, St. Vincent College Planetarium, 1997-1998
Assistant Director, St. Vincent College Planetarium, 1995-1997
Student Member, American Physical Society, 1995-Present

Table of Contents

List of Tables

List of Figures

Chapter 1

Introduction

More than two millenia ago, the ancient Greeks believed that while you could divide matter in half many times you would ultimately reach a point where the remaining matter was indivisible. The search for this *atomos* (atom) became one of the cornerstones of the scientific movement and has led physicists throughout the ages to seek out the fundamental constituents of matter. By the 18^{th} century, the fundamental building blocks of matter were thought by Newton to be tiny, indestructible spheres. Newton's theory was successful in describing the kinetic theory of gases but ultimately failed with the coming of the industrial revolution and the scientific knowledge acquired during it.

In the search for the fundamental particles of nature, the physics introduced during 20^{th} century proved to be of utmost importance. At the dawn of the 20^{th} century, atoms were no longer indestructible and Maxwell's theory of electromagnetism could not explain the particular nature of light. The discovery of X-rays in 1895 began the age of using accelerated particles to probe matter. By the 1920s, the development of quantum mechanics was essential to explain the interaction between the Rutherford atomic nucleus and the electron.

Further study and technological development in the mid-20^{th} century led to the development of theories describing the forces inherent in the interactions between the constituents of the nucleus and beta decay. Furthermore, the discovery, in cosmic ray and particle accelerator experiments, of a whole menagerie of previously unknown particles led to the postulation of an even more fundamental particle, the *quark*. Although strong experimental evidence supported the quark model, verification wasn't brought until the 1974 discovery of the J/ψ, which directly led to the development of the *Standard Model*.

The Standard Model has successfully predicted particle properties and has unified the electromagnetic and weak nuclear forces into a single $electro-weak$ force. Though it is a very successful theory, the Standard Model is incomplete. The particle believed to be responsible for mass generation, the Higgs boson, has yet to be discovered. Additionally, other problems afflict the Standard Model (*eg.* the hierarchy problem) and the search is ongoing for a more complete theory to solve the problems of the Standard Model as well as include the fourth fundamental force, gravitation. Nevertheless, the study of the Standard Model continues to be of great importance in the understanding of the nature of the physical world.

The Standard Model uses quantum field theories in an attempt to explain three of the fundamental forces of nature; electromagnetic, weak, and strong nuclear (see Figure 1.1). Grouped within the Standard Model are 25 particles, 12 fermions and 13 bosons. The fermion sector of the standard model consists of quarks and leptons, particles with 1/2 spin. The physical interactions between the quarks and leptons are governed through the exchange of the bosons. The massless photon (γ) carries the electromagnetic force, the very massive weak vector bosons ($Z^0, W^{\pm}$) carry the weak nuclear force, and the 8 massless gluons (g) carry the strong nuclear force.

Individual particles interact differently within the framework of the Standard Model. The quarks have fractional electromagnetic charge, carry color charge, and participate in all three interactions. Furthermore, specific quark combinations are the constituents of mesons ($q\bar{q}$) and baryons (qqq) (*eg.* the proton (uud)). The lepton sector consists of electron-like particles and neutrinos. The electron-like (e, μ, τ) particles have integer electromagnetic charge and participate in electromagnetic and the weak interactions. Neutrinos (ν_e, ν_μ, ν_τ) carry no electromagnetic charge and only interact via the weak interaction.

The study of charmonium, a system consisting of a charm and an anticharm quark, is essential to the understanding of the strong nuclear force, the theory describing it (Quantum Chromodynamics), and the Standard Model. Fermilab experiment E835 is dedicated to making high precision measurements of charmonium by utilizing proton-antiproton annihilations.

This dissertation describes the search for charmonium in the $\pi^0\pi^0$ channel at

FERMIONS matter constituents spin = 1/2, 3/2, 5/2, ...

Leptons spin = 1/2

Flavor	Mass GeV/c^2	Electric charge
ν_e electron neutrino	$<1\times10^{-8}$	0
e electron	0.000511	−1
ν_μ muon neutrino	<0.0002	0
μ muon	0.106	−1
ν_τ tau neutrino	<0.02	0
τ tau	1.7771	−1

Quarks spin = 1/2

Flavor	Approx. Mass GeV/c^2	Electric charge
u up	0.003	2/3
d down	0.006	−1/3
c charm	1.3	2/3
s strange	0.1	−1/3
t top	175	2/3
b bottom	4.3	−1/3

BOSONS force carriers spin = 0, 1, 2, ...

Unified Electroweak spin = 1

Name	Mass GeV/c^2	Electric charge
γ photon	0	0
W$^-$	80.4	−1
W$^+$	80.4	+1
Z^0	91.187	0

Strong (color) spin = 1

Name	Mass GeV/c^2	Electric charge
g gluon	0	0

Figure 1.1: Standard Model particle properties [1]. The Higgs boson is not listed.

experiment E835. The possible quantum numbers of the $\pi^0\pi^0$ final state imply that only the χ_{c0} and χ_{c2} states of charmonium may be seen. Moreover, due to a large non-resonant continuum, interference may play a role in the search.

In this chapter, the history of the charm quark and the discovery of charmonium is discussed. Additionally, the experimental and theoretical foundations of $c\bar{c}$ spectroscopy are surveyed. Finally, the potential for the study of the $\pi^0\pi^0$ final state as it relates to charmonium is presented.

Beginning with a description of the technique of resonance scanning, chapter two presents the experimental method employed by E835. A discussion of the method of stochastic cooling utilized in the Antiproton Accumulator is followed by an examination of the detector system, with an emphasis on the Pb-glass, electromagnetic calorimeters.

Chapter three provides a description of the data acquisition system used by E835. The data reduction techniques used by E835 are presented with an emphasis on the neutral hardware trigger, the most significant piece of the data acquisition system for the $\pi^0\pi^0$ analysis.

The determination of the $\pi^0\pi^0$ differential cross sections in the P-wave region of charmonium is discussed in chapter four. Explanations of the event selection, background subtraction, acceptance, and efficiency determinations are all included.

Results of the search for charmonium in the $\pi^0\pi^0$ channel is presented in chapter five, following a derivation of the $\pi^0\pi^0$ angular distribution. With the use of the large statistical sample ($\mathcal{L}=$ 32.8 pb^{-1} at the χ_{c0}), a measurement of $Br(\chi_{c0} \rightarrow p\bar{p}) \times Br(\chi_{c0} \rightarrow \pi^0\pi^0)$ was made. Finally, the systematic errors associated with the $\pi^0\pi^0$ analysis are discussed.

Chapter 6 compares the results of the $\pi^0\pi^0$ analysis with previous experimental results. Additionally, there is a discussion of a few theoretical models used to predict the individual branching fractions, $Br(\chi_{c0} \rightarrow p\bar{p})$ and $Br(\chi_{c0} \rightarrow \pi^0\pi^0)$. Finally, comparisons between these predictions and the results of the $\pi^0\pi^0$ analysis are made.

1.1 Historical Overview

In 1964, Murray Gell-Mann [2] and George Zweig [3] independently developed theories postulating that the many mesons and baryons discovered during the explosion of particle physics research in the mid-20th century were composed of new particles, quarks. The quark model was a logical extension of a theory that found patterns when particles with similar characteristics were grouped together. This "eight-fold way" [4] arranged baryons and mesons in terms of their charge and strangeness into groups (octets, decuplets), was successful in predicting the existence of new particles ($\Omega^-, \Delta^{++}, etc...$), and hinted at some unknown underlying symmetry later explained by the quark model.

If this quark model reflected nature, the hadronic interaction would be point-like. Strong experimental evidence for the hadronic interaction's point-like nature came from the comparison of the e^+e^- hadronic cross section to the point-like $e^+e^- \rightarrow \mu^+\mu^-$ cross section. The fairly constant ratio between the two supported the contention that the interactions were similar.

In the early stages of the quark model's development, only three quarks (*up*, *down*, *strange*) were necessary to explain the isospin and strangeness symmetries

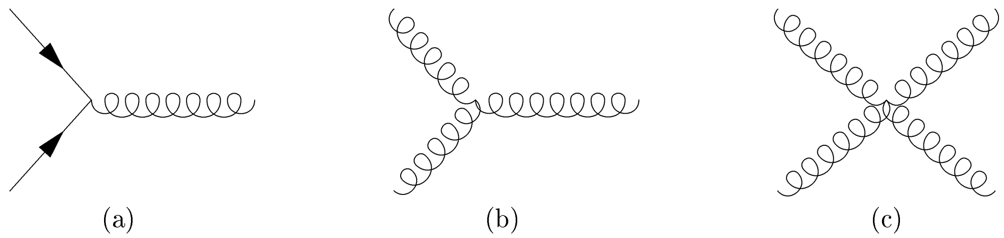

Figure 1.2: The interactions of QCD.

evident in the meson and baryon octets. However, the quark model's description of the baryon decuplet was insufficient. According to the quark model, the corner members of the baryon decuplet had to contain 3 identical quarks, *eg.* uuu for the Δ^{++}. With quarks having half-integer spin, the Pauli principle would have been violated, unless a new quantum number was introduced.

The new quantum number was called color and it's introduction into the quark model brought the age of Quantum Chromodynamics (QCD). Every quark was assigned one of three colors ($red, green, blue$) and the antiquarks were given one of the anticlolors ($\overline{red}, \overline{green}, \overline{blue}$). These colored quarks were only permitted to group together if the composite state was colorless[1]. Additionally, similar to the photon exchange in QED, interactions between quarks were governed through the exchange of colored gluons. However, unlike the photon in QED, gluons interact with one another. These gluon-gluon interactions (Figure 1.2b,c) are of great interest and introduce much of the complexity associated with QCD.

1.1.1 A 4^{th} Quark

In 1963, as a result of experimental observations, Cabibbo [7] developed a theory incorporating strangeness changing weak interactions into the quark model. Cabibbo postulated that the three known quarks formed a rotated isospin doublet

[1] $red + green + blue = \overline{red} + \overline{green} + \overline{blue} = white$ and $red + \overline{red} = green + \overline{green} = blue + \overline{blue} = white$.

for the weak interaction[2]:

$$\begin{pmatrix} u \\ d_c \end{pmatrix} = \begin{pmatrix} u \\ d\cos\theta_c + s\sin\theta_c \end{pmatrix}$$

Where θ_c is the Cabibbo angle, whose experimentally determined value is ~ 0.25. Calculating the matrix element for the charged and neutral current interactions with this Cabibbo rotated doublet, one finds the strangeness changing neutral currents are non-zero:

$$\underbrace{u\bar{u} + (d\bar{d}\ \cos^2\theta_c + s\bar{s}\ \sin^2\theta_c)}_{\Delta S=0} + \underbrace{(s\bar{d} + \bar{s}d)\ \sin\theta_c\ \cos\theta_c}_{\Delta S=1} \tag{1.1}$$

Cabibbo's result provided the theoretical motivation for what had been observed in charged current weak interactions ($W^{\pm}$ exchange). However, subsequent data disagreed with the Cabibbo theory when a suppression of the strangeness changing behavior in neutral current weak interactions (Z^0 exchange) became apparent.

Concurrent with the success of the Cabibbo theory and the quark model's description of the underlying symmetries evident in the mesons and baryons, Hara [5] along with Bjorken and Glashow [6] postulated the existence of a fourth quark (*hypercharge – center* or *charm*). This fourth quark would pair the four known leptons ($e,\ \nu_e,\ \mu,\ \nu_\mu$) with four quarks ($u,\ d,\ c,\ s$) in an approximate $SU(4)$ symmetric theory. Although the contention of Hara, Bjorken, and Glashow was weakened by a lack of experimental evidence, Glashow, Illiopoulos, and Maiani [8] used the idea of the charm quark to explain the suppression of the strangeness changing neutral current weak interactions in 1970. The "GIM" mechanism introduced an additional weak isospin doublet to the Cabibbo theory to create the desired suppression. The two doublets are:

$$\begin{pmatrix} u \\ d_c \end{pmatrix} = \begin{pmatrix} u \\ d\cos\theta_c + s\sin\theta_c \end{pmatrix} \qquad \begin{pmatrix} c \\ s_c \end{pmatrix} = \begin{pmatrix} c \\ -d\ \sin\theta_c + s\ \cos\theta_c \end{pmatrix}$$

This new doublet's contribution to the second term in equation 1.1 allowed the $\Delta S = 1$ part of the matrix element to cancel exactly, providing the required

[2]Using modern notation.

strangeness changing neutral current suppression:

$$(s\bar{d} + \bar{s}d - \bar{s}d - s\bar{d})\sin\theta_c \ \cos\theta_c = 0 \tag{1.2}$$

The GIM mechanism's success provided strong theoretical support for the existence of the charm quark. Experimental conformation would have to wait until 1974.

1.2 Charmonium

In November, 1974, independent groups led by S. Ting (BNL) [9] and B. Richter (SLAC) [10] simultaneously discovered a sharp resonance near 3.1 GeV. The Brook-haven group discovered the resonance (which they dubbed J) by studying the e^+e^- invariant mass spectrum from the reaction $p + Be \rightarrow e^+e^- + X$. The resonance was named ψ by the SLAC group where they were studying $e^+e^- \rightarrow leptons/hadrons$. Due to the simultaneous but independent discovery, the new particle was named the J/ψ.

Also in November, 1974, T. Appelquist and H.D. Politzer predicted the existence of narrow spikes in the e^+e^- annihilation cross section into hadrons [11]. These spikes were composed of a bound state of the charm quark and it's anti-particle. By April, 1975 the J/ψ and the ψ' (discovered 2 weeks after the J/ψ at SLAC [12]) were postulated to be members of this family of $c\bar{c}$ resonances [13].

This explanation was due to the extremely long lifetimes of the J/ψ and ψ'. Typical heavy hadron lifetimes are 50-1000 times longer than these particles. If the J/ψ and the ψ' consist of a $c\bar{c}$ bound state, when the particles decay the quantum number "charm" must be conserved. The J/ψ and the ψ' are not massive enough to decay into two charmed mesons ($2 \times M_D \sim 3.73\ GeV$) and must decay via a flavor changing annihilation. However, this decay is suppressed due to the weak coupling between quarks and hard gluons [3, 14, 15]. This "OZI" suppression directly leads to the extremely long lifetimes of charmonium.

Conformation of the charmonium hypothesis came less than a year after the discovery of the J/ψ and ψ'. Additional narrow resonances (χ's) were discovered by studying the radiative decays of the ψ' via e^+e^- annihilations at SLAC [16] and DESY [17]. The discovery of the J/ψ and the subsequent conformation of the

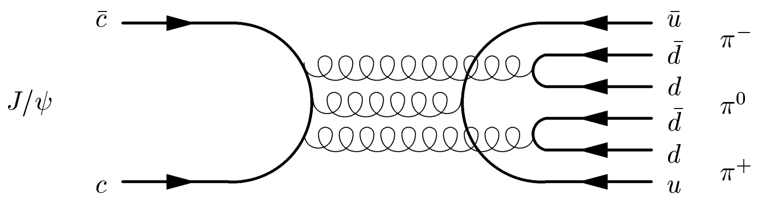

Figure 1.3: OZI suppressed decay of J/ψ to $\pi^+\pi^-\pi^0$.

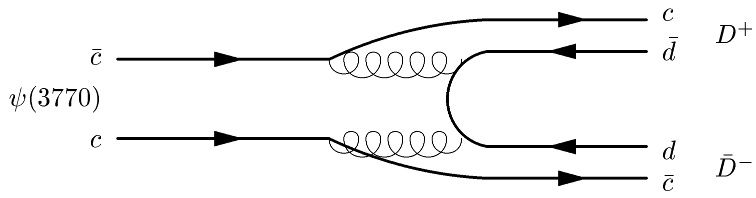

Figure 1.4: OZI allowed decay of $\psi(3770)$ to two charged D mesons.

charmonium hypothesis was an extremely important event in particle physics and as a tribute, the J/ψ's discovery has become known as the November Revolution.

1.2.1 Charmonium Spectrum

Figure 1.5 is a schematic of the family of particles known as charmonium. The vertical axis shows the mass or expected mass for the charmonium bound states as a function of their J^{PC} quantum numbers. J is the total angular momentum ($J = L \oplus S$), the parity is given by $P = (-1)^{L+1}$, and the charge conjugation is $C = (-1)^{L+S}$. The identification of each state is given by it's name and each states spectroscopic notation ($n^{2S+1}L_J$) is in parentheses; where S is the spin of the particle, L is the relative angular momentum between the charm and anticharm quark, and n is the radial excitation quantum number[3].

Other features of Figure 1.5 include the common decay channels for each of the particles, as well as the decay widths represented by the thickness of the lines that the states appear at. Due to the η_c, η_c', and h_c's quantum numbers (see Figure

[3]In the ground state $n = 1$.

1.5) they prove to be the most difficult charmonium states to observe and study. Despite the difficulties of producing and identifying these singlet states, the η_c has been studied, and both the h_c and η_c' have been seen, but are still awaiting conformation. Furthermore, the D-states, above the open charm threshold, have also been seen but will not be discussed here.

1.2.2 Theoretical Background

Following the discovery of the charmonium system and similarities between it's spectrum and positronium's, attempts were made to understand the strong interaction by using techniques developed for the study of the electromagnetic interaction (*ie.* potential models). The best known potential model used in the study of the charmonium spectrum incorporates the Cornell potential [18]:

$$V(r) = -\frac{4}{3}\frac{\alpha_s}{r} + kr \tag{1.3}$$

Where α_s is the strong coupling constant, r is the distance between quarks, and $k \sim 1\ GeV$ is a force constant. The first term in this potential is governed by single gluon exchange, provides the asymptotic freedom associated with QCD, and is analogous to the Coulomb potential of QED. The $\frac{4}{3}$ is called the "color factor" and is directly related to the requirement that composite quark systems are colorless. The second term represents multiple gluon exchange and is called the "confinement" term. As the distance between the quarks increase the confinement term becomes dominant. Additionally, the absence of free quarks in nature is attributed to the confinement term.

The Cornell potential is sufficient for predicting the spin-averaged charmonium spectrum. However, without modifying the Hamiltonian, there are no spin-dependent terms to predict the fine and hyperfine structure of the charmonium system, *ie.* the spacing between the χ states (fine structure) and the χ/ψ (h_c/η_c) hyperfine splitting.

The existence of both pseudoscalar and vector charmonium states led Pumplin *et. al.* [19] and Schnitzer [20] to postulate that the potential is governed by two exchange terms, scalar and vector ($V(r) = V_s(r) + V_v(r)$). Additionally, the technique used to incorporate spin dependent terms into the QED Hamiltonian for

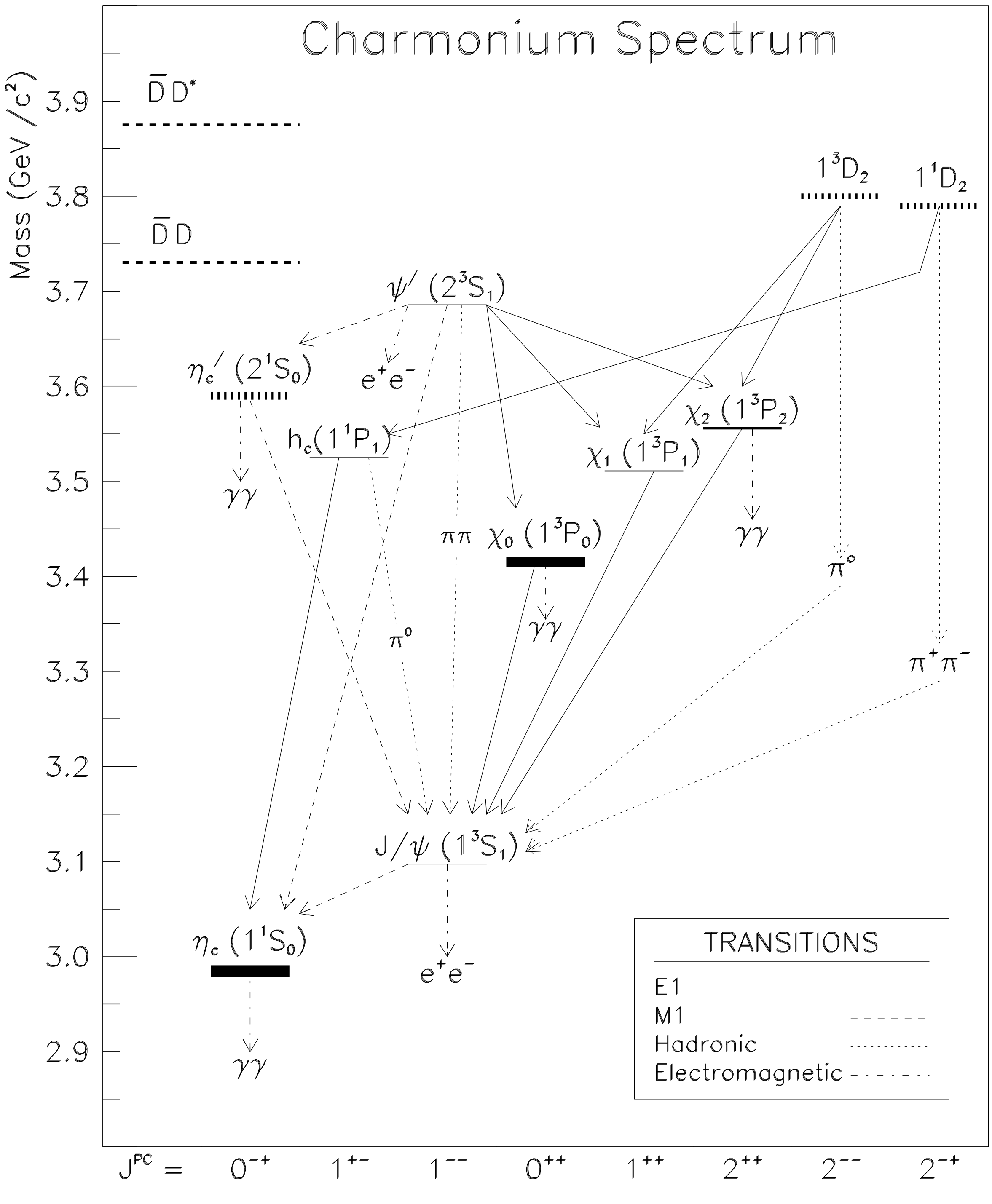

Figure 1.5: The charmonium spectrum.

positronium was used by assuming the heavy quark binding is governed by single-gluon exchange.

The Briet-Fermi Hamiltonian (as used for positronium) was expanded, perturbatively, to first order, in terms of $\frac{v^2}{c^2}$:

$$H = H_0 + H_1 = \left[2m_c + \frac{p^2}{m_c} + V_s(r) + V_v(r)\right] + \left[-\frac{p^4}{4m_c^3} + H_{SI} + H_{SO} + H_T + H_{SS}\right] \tag{1.4}$$

Where m_c is the mass of the charm quark and H_1 contains the following interaction terms:

- Spin-Independent:

$$H_{SI} = \frac{1}{4m_c^2}\left[\frac{2L(L+1)}{r}V_v' + \left[p^2, V_v - rV_v'\right] + 2\left(V_v - rV_v'\right)p^2 + \frac{1}{2}\left(\frac{8}{r}V_v' + V_v'' - rV_v'''\right)\right] \tag{1.5}$$

- Spin-Orbit:

$$H_{SO} = \vec{L} \cdot \left(\vec{S}_1 + \vec{S}_2\right)\frac{1}{2m_c^2 r}\left(3V_v' - V_s'\right) \tag{1.6}$$

- Tensor:

$$H_T = \left[\left(\vec{S}_1 \cdot \hat{r}\right)\left(\vec{S}_2 \cdot \hat{r}\right) - \frac{\left(\vec{S}_1 \cdot \vec{S}_2\right)}{3}\right]\frac{1}{m_c^2 r}\left(V_v' - rV_v''\right) \tag{1.7}$$

- Spin-Spin:

$$H_{SS} = \left(\vec{S}_1 \cdot \vec{S}_2\right)\frac{2}{3m_c^2}\nabla^2 V_v \tag{1.8}$$

Where $\vec{L}$, $\vec{S}_1$, and $\vec{S}_2$ are the orbital and spin angular momenta and the primes indicate single derivatives of the given potential with respect to r. The Coulomb-like term in equation 1.3 is contained within $V_v(r)$. The manifestation of the confinement term is in $V_s(r)$, but an additional vector-like component may be folded into $V_v(r)$ [21].

Although this non-relativistic Hamiltonian has been successful in predicting the charmonium spectrum, the higher order terms in $\frac{v^2}{c^2}$ remain important. Consider the viral theorem:

$$\langle T \rangle = \frac{1}{2} \left\langle \vec{r} \cdot \vec{\nabla} V(\vec{r}) \right\rangle \tag{1.9}$$

If one assumes the average radius of charmonium is approximately linear in r, then the binding energy of charmonium is thrice it's kinetic energy, $E_b = 3\langle T \rangle$, from $2\langle T \rangle = \langle V \rangle$. Using the non-relativistic expression $\langle T \rangle = 2\left(\frac{1}{2}\right) m_c \langle v^2 \rangle$, the expectation for the square of the velocity is:

$$\left\langle v^2 \right\rangle = \frac{E_b}{3m_c} \tag{1.10}$$

Now, taking the estimate of $m_c = 1.5\ GeV$ and the $J/\psi, \psi'$ mass difference as the binding energy (673 MeV):

$$\left\langle v^2 \right\rangle = 0.15c^2 \tag{1.11}$$

This simple calculation shows that the charmonium system is semi-relativistic. Thus, higher order terms in the perturbation theory can not be completely neglected.

The semi-relativistic nature of charmonium provides a good laboratory for studying the interface between perturbative and non-perturbative QCD. Other charmonium-like systems are also used to study properties of the strong interaction. The mesonic bound states of the light quarks (u, d, s), light-quarkonia, are highly relativistic and are not inhibited by OZI suppression. Also, the nearly equal light-quark masses along with the short lifetime of light-quarkonium often causes confusion in particle and constituent identification, see Figure 1.6. Nevertheless, light-quarkonium is a sufficient testing ground for non-perturbative effects inherent in the strong regime of the Standard Model. Additionally, due to the large mass of the bottom quark, excellent conditions for the study of perturbative QCD exist in the non-relativistic bottomonium system ($b\bar{b}$ bound state).

1.2.3 Charmonium Production and Spectroscopy

Charmonium is typically studied using e^+e^- or $p\bar{p}$ colliders. With these colliders four production methods are available; e^+e^- annihilation, $\gamma\gamma$ fusion, partial, and total $p\bar{p}$ annihilation.

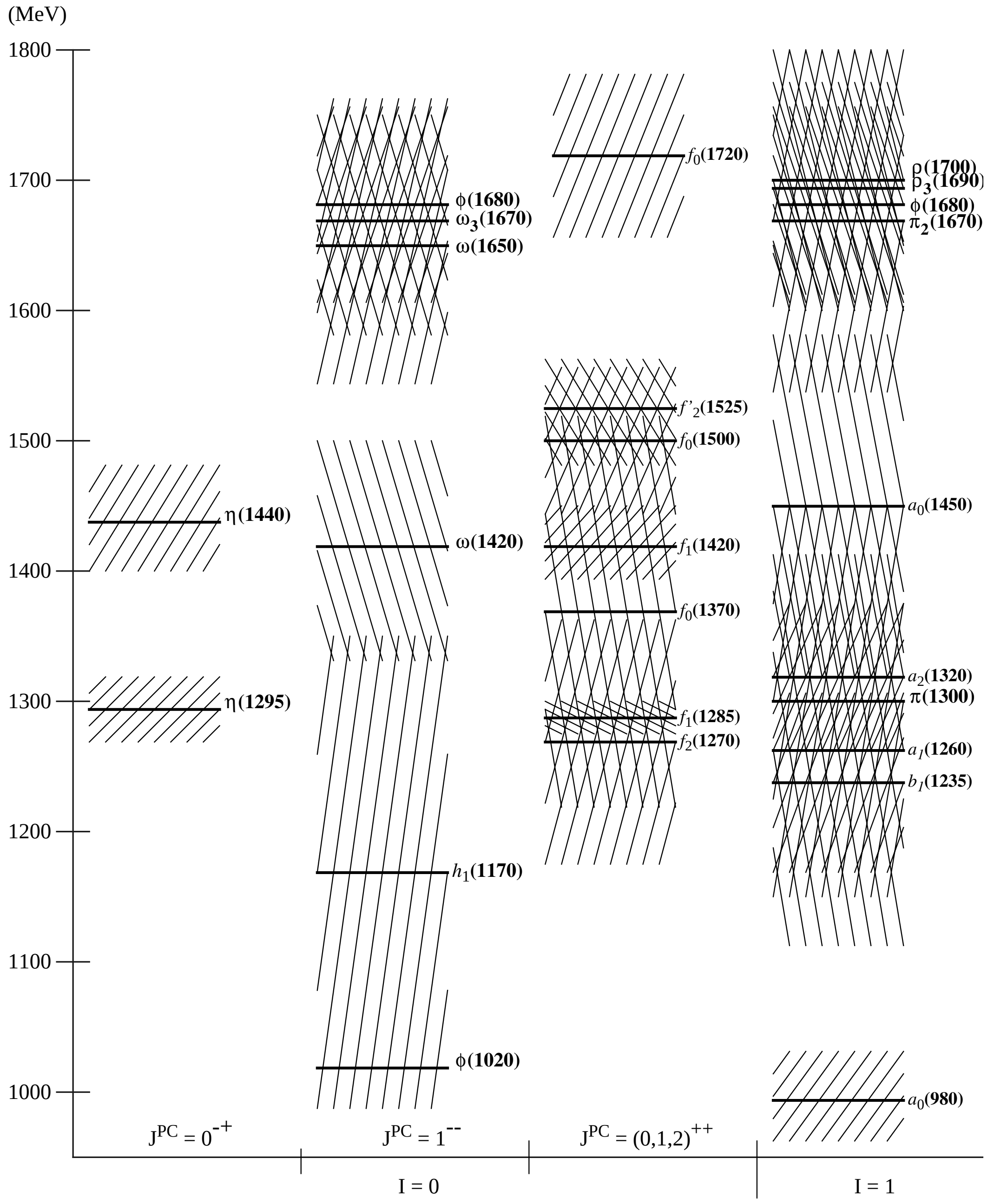

Figure 1.6: The light quarkonia spectrum [22]. The width of the state is represented by hash marks.

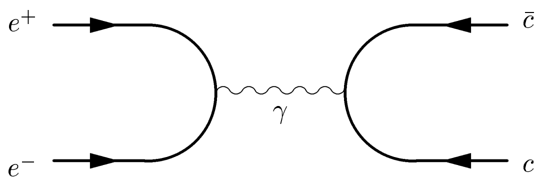

Figure 1.7: Charmonium production through a virtual photon in e^+e^- annihilation.

The majority of early charmonium spectroscopy was performed by using e^+e^- annihilation at SLAC with the Mark I, II, III, and the Crystal Ball detectors. The main disadvantage to using e^+e^- annihilations (Figure 1.7) is that only charmonium states with the same quantum numbers as the photon ($J^{PC} = 1^{--}$) can be directly produced. Nevertheless, other charmonium states are studied through the detection of radiative decays, *eg.* $\psi' \to \gamma\chi_{cJ}$. The ability to detect the radiated photon is of chief importance, but typically poor detector resolution along with large beam energy spreads, due to Bremsstrahlung radiation, makes direct measurements of resonance widths impossible. Instead, widths are measured by calculating the area under the final-state particle's excitation curve. This method has the undesirable effect of introducing acceptance and efficiency dependence into the width measurement.

Direct production of the C-even states, η_c, η_c', and the χ's, is possible in e^+e^- machines through the $\gamma\gamma$ fusion process (Figure 1.8). But, this process proceeds through two intermediate photons, introducing an additional factor of α^2 in the production rate. This additional factor causes the $\gamma\gamma$ fusion production rate to be 10^{-4} smaller than the e^+e^- annihilation rate.

With the development of stochastic cooling in the late 1970s [23], high-precision charmonium spectroscopy was opened up to $p\bar{p}$ interactions at antiproton storage rings and hadron colliders. Proton-antiproton machines have several possible charmonium production mechanisms available and they are classified according to the number of participating valence quarks:

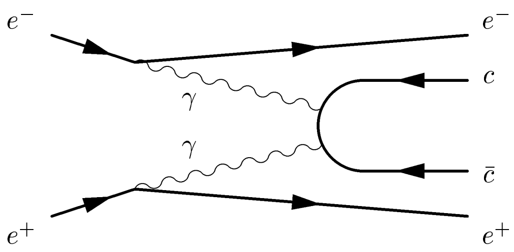

Figure 1.8: Charmonium production through two intermediate photons in an e^+e^- interaction ($\gamma\gamma$ fusion).

1. Class 0: Zero quarks annihilate. Rearrangement may occur, *eg.* $p\bar{p} \to \Delta\bar{\Delta}$. Furthermore, proton-proton interactions at the LHC may form charmonium though pure gluon fusion.

2. Class 1: Two quarks annihilate, four are spectators. Charmonium formed through this process is studied at high energy hadron colliders such as the Tevatron at Fermilab.

3. Class 2: Four quarks annihilate, two are spectators.

4. Class 3: All six valence quarks annihilate... total $p\bar{p}$ annihilation.

The most successful method for high precision charmonium spectroscopy utilizes the final class of $p\bar{p}$ interactions, total annihilation. A stochastically cooled antiproton beam scanning the charmonium energy region eliminates many problems encountered at e^+e^- machines. Total annihilation may proceed through either two or three gluons[4], allowing direct formation of all charmonium states. Furthermore, due to the much smaller radiative corrections needed for the precise determination of the center of mass energy (from $m_p \gg m_e$), $p\bar{p}$ annihilations allow direct resonance width measurements.

[4] Color conservation forbids single gluon annihilation.

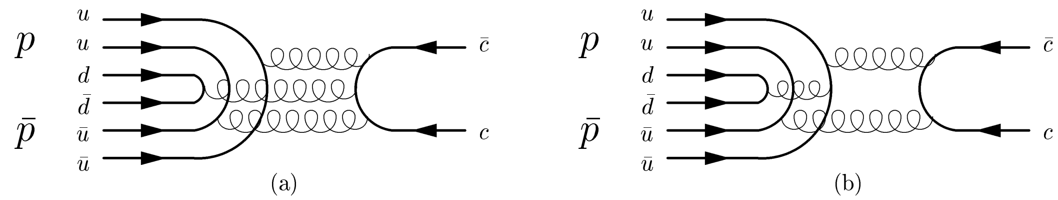

Figure 1.9: Charmonium production from $p\bar{p}$ annihilations via 3 (a) and 2 (b) gluons.

However, there is one problem that is inherent in studying charmonium with $p\bar{p}$ interactions; the $p\bar{p}$ hadronic cross section in the charmonium energy region is about 70 mb, while the charmonium production cross sections are at the picobarn and nanobarn levels. In order to separate the hadronic background from the charmonium production, electromagnetic final states are tagged as charmonium formation, drastically increasing the signal-to-background ratio.

The earliest study of charmonium using total $p\bar{p}$ annihilation was made at the CERN ISR. Experiment R704 used a hydrogen gas jet target to perpendicularly intersect a cooled antiproton beam and a two-armed spectrometer to detect the direct production of the η_c, χ_{c1} , and χ_{c2} for the first time [24, 25, 26].

On the heels of R704's success, Fermilab commissioned an experiment located in the Antiproton Accumulator to perform spectroscopy of the charmonium system. Borrowing from R704, E760 used a perpendicularly intersecting hydrogen gas jet. E760 also featured a cylindrically symmetric spectrometer with two Pb-glass calorimeters. E760 and it's successors E835 and E835$'$ accumulated $\sim 280\ pb^{-1}$ of data in three periods, '91/92, '96/97, and 2000. With this data in hand E760/E835 continues to make high precision measurements of charmonium resonances below the open charm threshold [27].

Branching Fraction	Value ($\times 10^{-3}$)
$Br(\chi_{c0} \rightarrow \pi^0\pi^0)$	$3.1 \pm 0.4 \pm 0.5$ [29]
	$2.65 \pm 0.30 \pm 0.58$ [30]
$Br(\chi_{c2} \rightarrow \pi^0\pi^0)$	$1.1 \pm 0.2 \pm 0.2$ [29]
	$0.87 \pm 0.24 \pm 0.50$ [30]
$\frac{1}{2}Br(\chi_{c0} \rightarrow \pi^+\pi^-)$	2.5 ± 0.35 [28]
$\frac{1}{2}Br(\chi_{c2} \rightarrow \pi^+\pi^-)$	0.76 ± 0.13 [28]

Table 1.1: Current measurements of charmonium decaying into 2 pions.

1.3 $\pi^0\pi^0$ Production

The π^0 is the lightest known meson and is one of the best know particles in physics. Consisting of a $u\bar{u}$ and $d\bar{d}$ mixed state, the π^0 meson decays primarily to 2 photons ($\sim 98\%$), and has a mass of 135 MeV [28]. Utilizing e^+e^- annihilation and the radiative decays of the ψ', there has been some success in detecting charmonium in the $\pi^0\pi^0$ channel [29, 30]. The current measurements of charmonium production through the $\pi^0\pi^0$ state is listed in table 1.1. Additionally, through the use of the properties of isospin symmetry, estimates of the charmonium production rates in the $\pi^0\pi^0$ channel can be made from measurements of $\chi_{cJ} \rightarrow \pi^+\pi^-$. As also can be seen from table 1.1, current estimates utilizing $Br(\chi_{cJ} \rightarrow \pi^0\pi^0) = \frac{1}{2}Br(\chi_{cJ} \rightarrow \pi^+\pi^-)$ are in reasonable agreement with the e^+e^- measurements.

The detection of charmonium in the $\pi^0\pi^0$ final state is non-trivial in $p\bar{p}$ annihilations. The $\pi^0\pi^0$ state can be accessed through even momentum states with positive parity and charge conjugation ($J^{PC} = even^{++}$). Through partial $p\bar{p}$ annihilation (Figure 1.10) all possible $\pi^0\pi^0$ quantum numbers are accessible to the $p\bar{p}$ initial state. The result is a large non-resonant continuum. Resonance production, on the other hand, only accesses the $\pi^0\pi^0$ final state through the angular momentum state of the resonance in question, eg. $J = 0$ for the χ_{c0} . Furthermore, for the S-wave χ_{c0} , there is no angular dependence to boost $\pi^0\pi^0$ production at large $\cos\theta^*$. Without constructive interference playing a role, the presence of the resonance would be washed away by the forward peaked incoherent continuum.

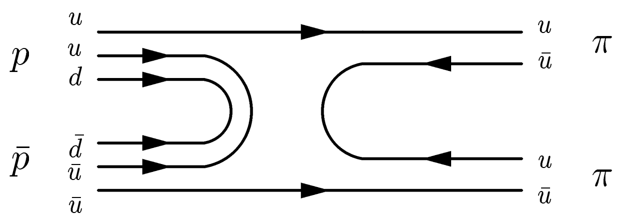

Figure 1.10: Non-resonant $\pi^0\pi^0$ production (class 2).

Chapter 2

Experimental Apparatus

Experiment E835 studied charmonium formed in proton-antiproton interactions at Fermi National Accelerator Laboratory. The hadronic background for proton-antiproton interactions at charmonium energies is ~ 70 mb. The E835 detector was optimized to extract pb and nb cross sections from this background by tagging electromagnetic final states. E835 consisted of an antiproton ring, a hydrogen gas jet, and a detector which featured 2 lead-glass calorimeters. Paramount in the investigation of charmonium with this apparatus was the ability to precisely determine the interaction energy. This determination required precise knowledge of the antiproton beam's parameters, especially the momentum spread and the beam's position.

2.1 Experimental Technique

Charmonium resonances were studied at E835 by varying the center of mass energy in steps while measuring the cross section at each step. The excitation curve that was measured (see Figure 2.1) is a convolution of the $\bar{p}$ beam energy spectrum and the Briet-Wigner cross section:

$$\sigma(E_{cm}) = \int_0^\infty \sigma_{BW}(E')G(E' - E_{cm})dE' \tag{2.1}$$

where $G(E)$ is the beam energy distribution at energy E and:

$$\sigma_{BW}(E) = \frac{4\pi}{k^2}\frac{2J+1}{(2S_1+1)(2S_2+1)}\frac{\Gamma_{in}\Gamma_{out}}{4(E - M_{res}c^2) + \Gamma_{res}^2} \tag{2.2}$$

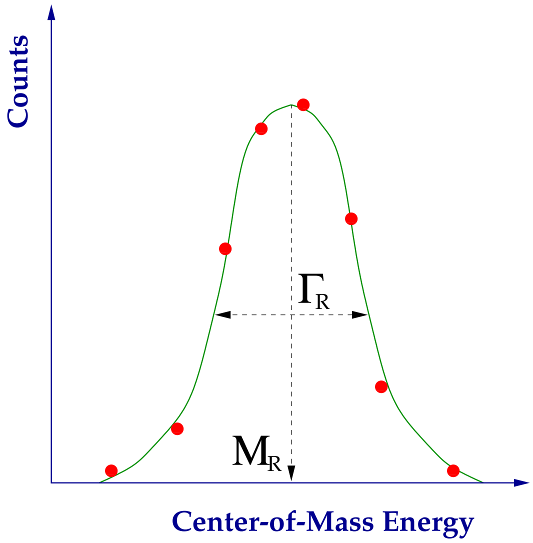

Figure 2.1: Model of a measured excitation curve in E835.

where k is the momentum of the antiproton in the collision, J is the spin of the resonance, and $\Gamma_{in(out)}$ is the partial decay rate of the resonance into the initial(final) state. The resonance parameters, M_{res} and Γ_{res} as well as the product $\Gamma_{in}\Gamma_{out}$ are extracted with the knowledge of the beam energy distribution. This technique of measuring resonance parameters as well as partial widths is advantageous because the detector is not used for measuring the center-of-mass energy of the interaction. Thus, the energy determination is not dependent upon the finite resolution of the detector.

2.2 Antiproton Accumulator

The Antiproton Accumulator (AA) housed the E835 detector in one of its low dispersion sections, AP-50 (Figure 2.2). The AA is used to store large stacks of antiprotons, mostly for use in the Tevatron. Antiprotons are created by extracting bunches of 5×10^{12} protons at 120 GeV from the Main Injector with a frequency of about $\frac{1}{2}$Hz. These protons are incident on a cylindrical target composed of nickel and copper disks. The nickel disks provide the interaction which creates

$c\bar{c}$ State	Mass (GeV/c^2)	P_{beam} (GeV/c)
χ_{c0}	3417	5200
χ_{c1}	3511	5552
$^1P_1$	3526	5609
χ_{c2}	3556	5724
ψ'	3686	6232

Table 2.1: $\bar{p}$ beam momentum required for particular center of mass energies.

the antiprotons[1] while the copper disks provide thermal cooling. The target rotates about the disk's common axis in order to prolong the target's life. After interacting with the target the negative secondaries are focused by the Collection Lens Module, a cylindrical lithium conductor under an intense longitudinal current. After the target station, a pulsed magnet selects 8 GeV particles and bends them into the AP2 line which leads to the Debuncher. Particles not selected by the pulsed magnet are absorbed by a graphite core beam dump.

Antiprotons enter the Debuncher with a momentum spread of $\frac{\Delta p}{p} \sim 0.04$. The momentum spread is reduced in the Debuncher through RF bunch rotation and adiabatic debunching. To improve Debuncher-to-Accumulator transfer efficiency, the Debuncher uses the time between Main Injector cycles to further reduce the momentum spread via betatron and longitudinal momentum cooling.

Once the antiprotons are in the Accumulator, the momentum spread is further reduced to 0.1%. Antiprotons are stacked in the Accumulator for several hours until a desired beam density is reached, typically 50 mA ($\sim 5 \times 10^{10}$ $\bar{p}$s). A typical stacking rate is $\sim$ 3 mA/hr. When the desired stack size is reached, the antiprotons are decelerated from a momentum of 8.9 GeV to the momentum corresponding to the collision energy of interest (Fig. 2.1).

The beam energy distribution must be known precisely in order to study the narrow charmonium resonances. Resonant measurement precision is directly related to the average beam energy measurement. The beam energy is related to the revolution frequency by:

$$\beta c = f\mathrm{L} \tag{2.3}$$

[1] $1\bar{p}$ for every 10^6 p's on target.

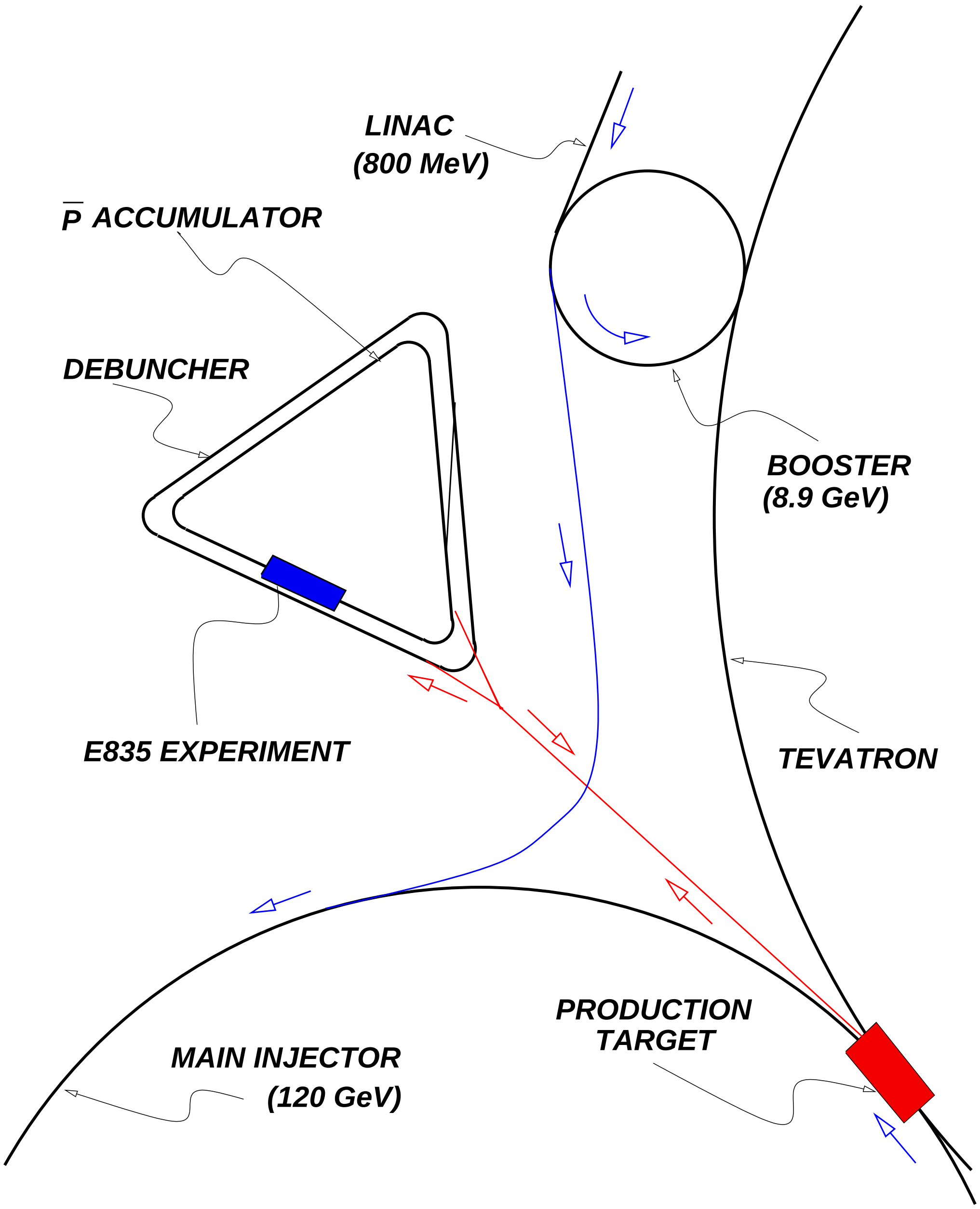

Figure 2.2: The FNAL accelerator complex

Where f is the revolution frequency, L is the orbit length and βc is the speed of the antiprotons. The mean revolution frequency of the antiprotons is ~0.6 MHz, which is measured with a precision of better than 1 Hz. The center of mass energy ($\sqrt{s}$) is measured with an error of ~100 keV and is dominated by the uncertainty in the orbit length, ~0.7 mm.

A reference orbit was used to measure changes in the orbit length. The beam position at the momentum corresponding to the mass of the ψ' resonance was used as the reference orbit. The ψ' was chosen as the reference orbit due to the precise knowledge of its mass, $\sigma_{M_{\psi'}} = 90$ keV. The length of the reference orbit is 474.05 m. As the beam momentum is changed, the change in the orbit length is measured with Beam Position Monitors (BPMs)[2]. This method of measuring the orbit length led to a systematic error on the measurement of the ψ' mass of 150 keV.

The revolution frequency distribution is measured by studying the Shottky noise spectrum. The number of antiprotons populating a particular frequency is related to the amplitudes of the Shottky bands. A quarter wavelength pickup is used to acquire the Shottky noise spectrum and the power spectrum is then determined with a spectrum analyzer using:

$$P(f) = 2\pi(ef)^2\frac{dN}{df} \tag{2.4}$$

The momentum distribution is then calculated from:

$$\frac{dp}{p} = -\frac{1}{\eta}\frac{df}{f} \tag{2.5}$$

where $\eta \equiv 1/\gamma_t^2 - 1/\gamma^2$ is the slip factor, for $\gamma = E_{beam}/m_p$. At the transition energy, $\gamma_t = \gamma$. The antiproton beam at the transition energy is unstable. Thus, deceleration of the beam across the transition must be done very carefully and with smaller beam currents to minimize losses.

2.3 Hydrogen Gas Jet Target

The target used in E835 was a molecular hydrogen gas jet that intersected the antiproton beam perpendicularly [32]. The gas jet was located just upstream

[2]There are 42 vertical and 48 horizontal BPMs in the AA.

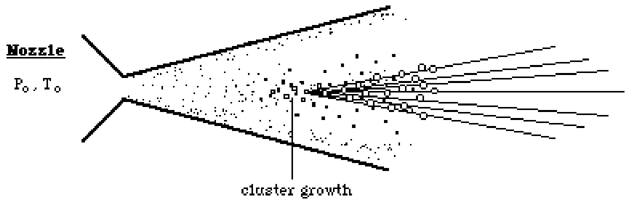

Figure 2.3: Schematic of cluster formation in the gas jet target.

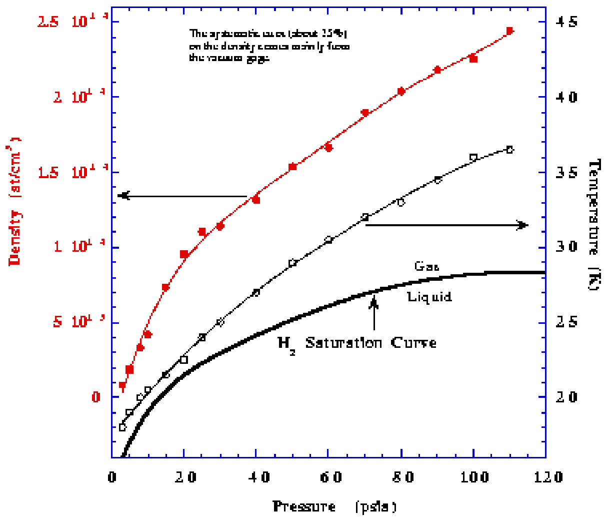

Figure 2.4: Variable temperature and pressure allowed the gas jet's density to be adjusted.

from the detector and had a trumpet shaped nozzle. The nozzle had an opening angle of 3.5° which encouraged growth of clusters as the molecular hydrogen gas adiabatically expanded into the beam pipe. As the hydrogen expanded, clusters of about 10^8 molecules formed. This cluster formation is depicted in Fig. 2.3.

Due to the ~1 MHz interaction rate with target and residual gases in the beampipe, the antiproton beam degraded over time, and the temperature and pressure of the gas jet was adjusted to keep the interaction rate constant (Figs. 2.4 and 2.5). The density range of the gas jet target was $(0.1-3.2)\times 10^{14}$ atoms/cm^3. A system of vacuum pumps was also incorporated in the target area to preserve the quality of the antiproton accumulator vacuum.

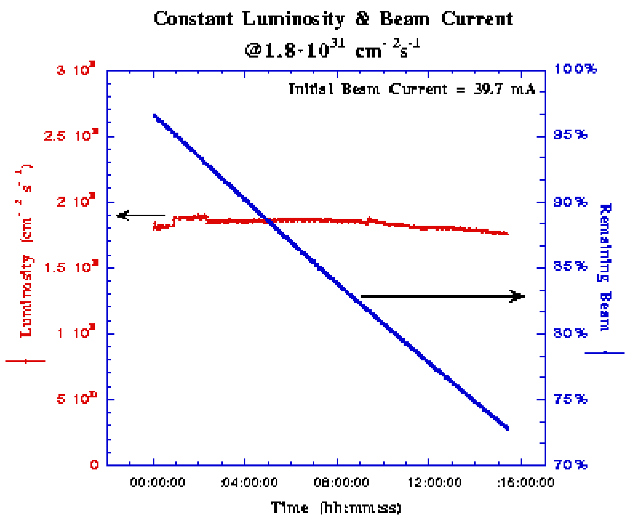

Figure 2.5: The gas jet density was increased in order to maintain a constant interaction rate as the antiproton beam degraded over time.

2.4 The E835 Detector

The detector (Fig. 2.6) consisted of 5 main subsystems: The Luminosity Monitor, Inner Detector, Čerenkov Counters, Central Calorimeter, and Forward Calorimeter. The Luminosity Monitor measured the rate of small angle elastic proton-antiproton scattering which was used to determine the beam-target interaction rate. The Inner Detector consisted of 8 components and was used to identify and track charged particles. The Central and Forward Calorimeters were arrays of lead-glass blocks and were used for measuring the positions and energies of final state particles.

2.4.1 Luminosity Monitor

The Luminosity Monitor was located just below the interaction region and was used to measure the integrated luminosity by taking advantage of the precisely measured small angle $\bar{p}p$ differential cross section [33]. The Luminosity Monitor's silicon detectors were located at an angle of 86.4° from the beam direction and counted the recoil protons from elastic $\bar{p}p$ scattering. The integrated luminosity

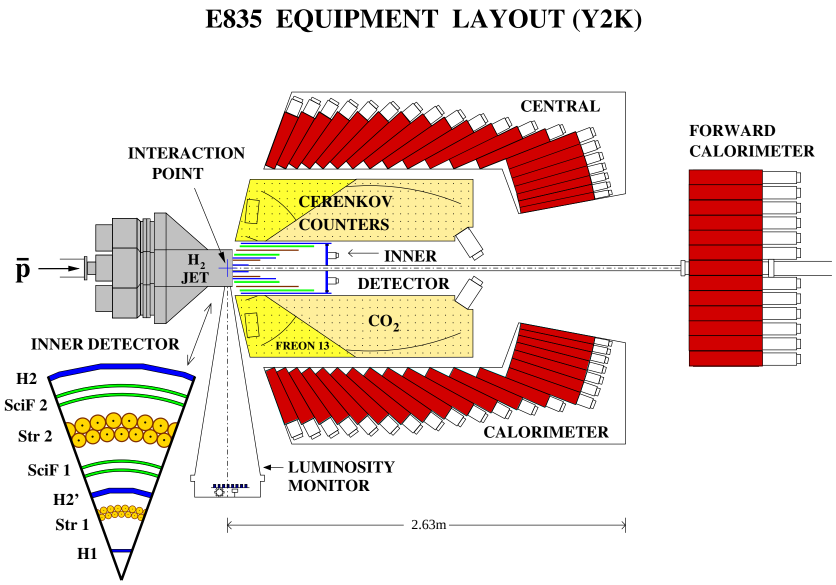

Figure 2.6: The E835$'$ detector.

was then obtained from:

$$N = \epsilon \int L dt \int \frac{d\sigma}{d\Omega} d\Omega \qquad (2.6)$$

where N is the number of observed recoil protons in the Luminosity Monitor, ϵ is the detector efficiency, and the integral is over the active area of the Luminosity Monitor's detectors. The systematic error associated with the Luminosity Monitor was determined to be 2.5% [58].

2.4.2 Inner Detector

There were eight charged particle identification systems located within the central calorimeter. These systems collectively make up the inner detector. The inner detector's main function was to tag and track charged particles and provide signals for the hardware triggers.

Scintillating Hodoscopes

Four plastic scintillator detectors, the hodoscopes, were used to detect charged particles and provide fast trigger signals. Three hodoscopes were arranged with cylindrical symmetry about the beam axis, the fourth was positioned perpendicular to the beam direction.

H1 was the innermost hodoscope and consisted of 8 elements. Each element was made of 1 mm thick Bicron 408 and was placed 5 cm from the center of the beam pipe. The polar coverage of H1 was from 9° to 65°. H2 was located at a radius of 15.8 cm from the center of the beam pipe and consisted of 32 elements, each of which was 2 mm thick. The polar coverage of H2 was from 15° to 65°. H2′ was situated between H1 and H2, at a radius of 7 cm, and consisted of 24 elements (2 mm thick).

The alignment of H1 and H2 was such that one H1 paddle coincided exactly with 4 H2 paddles. To reduce the inefficiencies due to the gaps between the counters, H2′ was positioned so that the center of the H2′ paddles were aligned with the common cracks in H1 and H2.

The Forward Charged Hodoscope (FCH) consisted of 8 elements each of which covered ∼50° in azimuthal angle. Adjacent paddles had about 2.5° of overlap. The polar coverage of the FCH was from 2° to 10° . The FCH was used to veto events with charged tracks in the forward direction and to identify energy deposits in the forward calorimeter. Each element of the 4 hodoscopes was light tight, coupled to their own light guides, and read out by a PMT[3].

Straws

Two cylindrical straw-tube chambers [34] measured the azimuthal coordinate, ϕ, of charged particle tracks. The chambers were located at 5.4 and 12.0 cm from the center of the beam pipe and had a polar coverage from 15° to 60°. Each chamber was positioned so that the two staggered layers of 64 straw tubes were parallel to the beam pipe. Providing a drift velocity of $\sim 40\mu$m/ns, the gas mixture used in straws, Ar : C_4H_{10} : $[(OCH_3)_2CH_2]$[4], both limited radiation damage and provided a high efficiency at low HV. Output signals from all of the 128 channels were sent to TDCs by Amplifier-Shaper-Discriminators (ASDs) mounted on the downstream end of the chambers.

[3] H1, H2, and the FCH were read out by Philips XP2982 PMTs, whereas H2′ utilized Hammamatsu R1398 PMTs.

[4] The proportions of the gas mixture was 82:15:3.

The detection efficiency of a track with hits in at least 2 layers of straws was 97%, with the efficiency of an individual layer at about 90%. This layer efficiency ranged from 100% near the anode wire to $\sim$80% near the tube wall (cathode). The angular resolution of a track was 9 mrad, measured with a clean two body sample, $J/\psi \to e^+e^-$.

Scintillating Fibers

Two cylindrical Scintillating Fiber Trackers (SCIFI) measured the polar coordinate, θ, of charged particles [35, 36]. The polar coverage for the inner (outer) tracker was 15°-55° (15°-65°). The SCIFI was also used in the level 1 trigger to select hadronic channels based on kinematics. Each tracker had 2 staggered layers of Kuraray SCSF-3HF-1500 multi-clad fibers wrapped around a support cylinder[5]. The support cylinders had average radii of 8.5, 9.7, 14.4, and 15.06 cm. The fibers had an outer diameter of 0.835 mm and a core diameter of 0.74 mm. The fibers were also aluminized at one end to improve homogeneity. The non-aluminized ends were thermally spliced to clear fibers which carried the light to the surface of the Visible Light Photon Counters (VLPCs) [35].

The VLPCs are solid state photo detectors and were housed in a cryostat operated at a temperature of 6.5-7.2 K. The VLPCs provided both pulse height and timing signals which were amplified and sent to ADCs, TDCs, and the level 1 trigger logic. The efficiency of the two SCIFI trackers was 90% for $\theta >40°$ and increased to 98% for smaller angles. The SCIFI detector had the best spatial resolution in the entire detector. The z coordinate resolution for a two layer hit was 0.5 ± 0.1 mm for $\theta >40°$, and 0.22 ± 0.07 mm for small angles.

2.4.3 Threshold Čerenkov Counter

The threshold Čerenkov counter was used to separate electrons and positrons from the large hadronic background in the charmonium energy region [37]. Good separation also allowed the Čerenkov detector to be used in the charged particle trigger. It was located between the Inner Detector and the Central Calorimeter. It had an inner radius of 17 cm and an outer radius of 59 cm. The detector contained

[5]The inner tracker had 480 channels whereas the outer tracker had 840 channels.

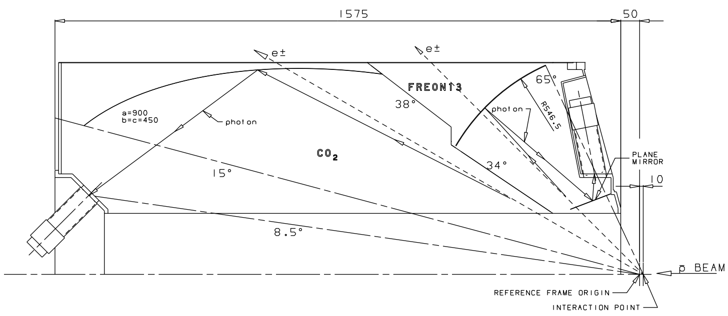

Figure 2.7: Schematic of the Čerenkov Counter. All dimensions are in mm.

two cells covering the full azimuth. The downstream (small angle) cell's θ coverage was from 15° to 38° and the upstream (large angle) cell covered 34°$< \theta <$65°.

Each cell was segmented into 8 sections covering 45° in azimuth and aligned with H1. A downstream and an upstream section are shown in Figure 2.7. Each downstream section contained an ellipsoidal mirror with one focus at the interaction region and the other at the PMT window. The ellipsoidal mirrors were constructed from a carbon fiber epoxy composite. The upstream sections contained spherical and plane mirrors to reflect light onto the PMT at the back wall of the cell. The plane mirrors were constructed from 1 mm thick aluminized glass mirrors with a MgF_2 protective coating. The spherical mirrors were manufactured by slumping 3 mm thick glass slabs onto a concave cast iron mold. An average photoelectron yield for the 2 in. diameter Hammamatsu R1332Q PMTs was 14-16 (9-10) for the downstream (upstream) cell. Signals sent from the PMTs were amplified, split, and sent to the charged trigger logic, ADCs, and TDCs.

To achieve a high electron detection efficiency and good electron to pion separation, the cells were filled with different gases, both maintained at room temperature and atmospheric pressure. The downstream cell contained carbon dioxide (CO_2) with an index of refraction of $n_{CO_2} = 1.00041$, and the upstream cell operated with Freon 12 (CF_2Cl_2) with $n_{CF_2Cl_2} = 1.00108$. The Čerenkov angle[6], θ_c, is given by $\theta_c = \frac{1}{\beta n}$, where $\beta = 1$ and n is the index of refraction of the medium that the particle is traversing. For CO_2, the Čerenkov angle is θ_c=1.64°, For Freon 12,

[6]The Čerenkov angle is the minimum angle subtended by the light emitted from the moving particle as it travels through a material faster than light travels through the same material.

θ_c =2.66°. The energy threshold, $E_{thresh.}$, given by:

$$E_{thresh.} = \frac{m}{\sqrt{1 - \frac{1}{n^2}}} \tag{2.7}$$

where m is the particle mass. Equation 2.7 gives the pion (electron) energy thresholds as 4.873 ($\sim$ 0.018) GeV and 3.003 ($\sim$ 0.11) GeV for CO_2 and CF_2Cl_2 respectively. The large difference in the energy thresholds is due to the small electron mass. Fewer than 0.5% of charged pions were mis-identified as electrons by the Čerenkov detector [38]. The total efficiency of the Čerenkov detector was calculated using clean samples of $\chi_{c2} \to J/\psi\gamma \to e^+e^-\gamma$ and $J/\psi \to e^+e^-$, and the efficiency was $(98.1 \pm 0.5)\%$.

2.4.4 Central Calorimeter

The central calorimeter (CCAL) was the main detector component in E835. The CCAL's function was to measure the position and energy of electromagnetic showers. Different views of the CCAL can be seen in Figures 2.8 and 2.9

Design and Readout

The CCAL was composed of 1280 Schott F2 type lead-glass blocks arranged in 20 rings of 64 blocks. lead-glass has a radiation length of 3.141 cm and a density of 3.61 g/cm^3. The blocks lengths varied from 12 to 16 radiation lengths, 38 to 50 cm. The variable block length allowed for a near constant shower containment throughout the calorimeter, $\sim$ 95%. The granularity of the detector was a compromise between maximizing the resolution of symmetric π^0 decays and minimizing the inert material between blocks.

Each ring had full azimuthal coverage at a common θ and was designed so the front face of each block was positioned perpendicular to a line connecting the interaction point to the center of the block. The blocks positioned at a common ϕ are called wedges. Each wedge had a theta range of 10.6° to 70° and contained 20 blocks. The azimuthal range of each wedge was 5.625°. Table 2.2 lists the length, central θ, distance from target, and other relevant parameters, of the CCAL blocks.

Block Number	Block Length (cm)	Central θ (deg)	Block Width (deg)	Distance from Target (cm)	PMT Diameter (inches)	Fractional PMT Coverage
01	37.80	67.387	5.226	72.44	3.0	0.473
02	38.65	62.259	5.031	75.87	3.0	0.475
03	39.88	57.342	4.803	80.07	3.0	0.476
04	41.50	52.664	4.552	85.08	3.0	0.478
05	43.54	48.246	4.284	90.96	3.0	0.479
06	46.03	44.101	4.007	97.79	3.0	0.481
07	48.98	40.234	3.728	105.62	3.0	0.482
08	50.00	36.644	3.451	114.54	3.0	0.497
09	50.00	33.327	3.183	124.66	3.0	0.520
10	50.00	30.273	2.925	136.07	3.0	0.544
11	50.00	27.472	2.679	148.89	3.0	0.568
12	50.00	24.908	2.449	163.26	3.0	0.593
13	50.00	22.567	2.233	179.34	3.0	0.617
14	50.00	20.434	2.033	197.28	3.0	0.641
15	50.00	18.493	1.848	197.29	2.5	0.546
16	50.00	16.730	1.678	197.29	2.5	0.664
17	50.00	15.130	1.522	197.30	2.0	0.527
18	50.00	13.679	1.380	197.30	2.0	0.644
19	50.00	12.364	1.250	197.30	1.5	0.443
20	50.00	11.174	1.131	197.30	1.5	0.543

Table 2.2: Length, width, θ position, distance to the interaction point, and PMT characteristics for the 64 blocks in each CCAL ring.

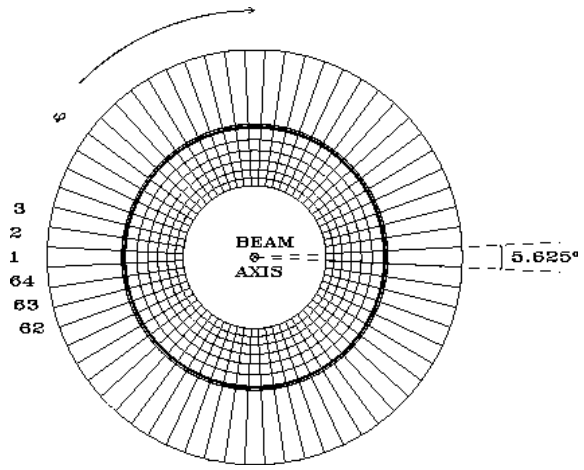

Figure 2.8: The Central Calorimeter; beam's eye view.

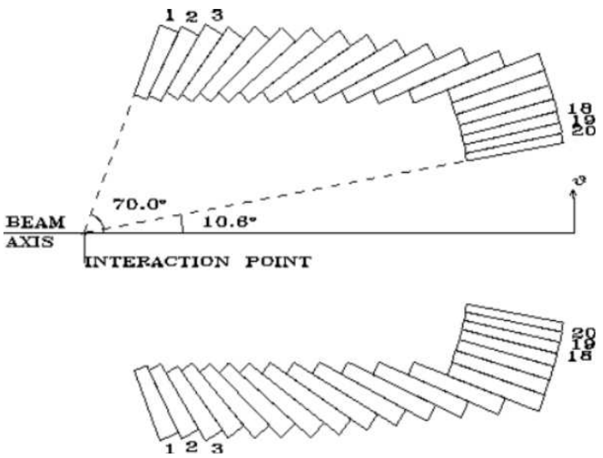

Figure 2.9: Central Calorimeter side view. This schematic shows 2 wedges of the CCAL separated by 180° in ϕ.

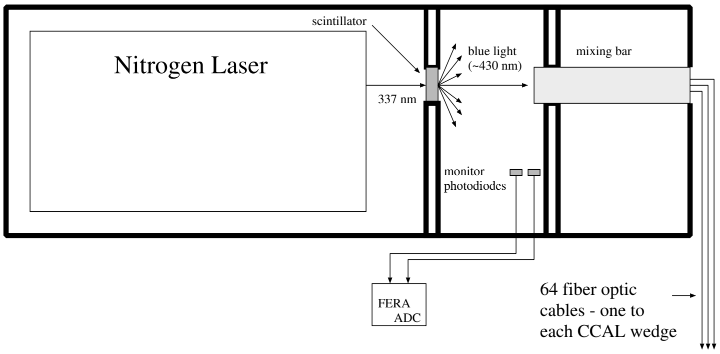

Figure 2.10: The Laser Monitoring System's layout.

Light from the lead-glass blocks was collected by Hammamatsu[7] PMTs glued to the back of each block. Different sized blocks required different sized PMTs to maximize light collection. Four sizes of PMTs were used with diameters ranging from 1.5 to 3 inches. For rings 1-14, 3" R3036-02 PMTs were used, rings 15 and 16 used 2.5" R3345-02, rings 17 and 18 used 2" R2154-04s, and rings 19 and 20 used 1.5" R580-13s. Each PMT was read out by a coaxial RG-174 cable with an intermediate connection at the wedge housing.

Laser Monitor System

The Laser Monitor system was designed as a quality control device for the calorimeters. At the back of each CCAL and FCAL block a plastic polymer fiber optic cable was inserted in order to monitor the gain of the PMTs and study the degradation of the lead-glass. Radiation damages lead-glass over time and degrades the readout signal. Injecting a fixed amount of light into the CCAL, triggered by a 10 Hz pulsar, allowed this damage to be studied. Figure 2.10 is a schematic of the Laser Monitor System.

A light-tight aluminum box contained a nitrogen laser[8], a scintillator, a lucite mixing bar, and 2 PIN diodes. The laser was chosen due its pulse stability ($\sim 4\%$), its short rise time (about 1 ns), and its narrow pulse width (3 ns). The narrow

[7]Hammamatsu Photonics, 1126-1 Ichino-Cho, Hammamatsu-City, Japan.

[8]Manufactured by Laser Science Incorporated. The model number was VSL-337ND

width allowed the data from the 10 Hz gate to be collected on a special trigger by the data acquisition system. The ultraviolet light emitted by the laser was used to excite a scintillator which shifted the incident light into the visible region (430 nm), which matches the transmission of the polymer fiber. The scintillation light then entered the primary mixing bar which distributed the light to the 64 wedges. Within each wedge the light was distributed to each block via a secondary mixing bar. The PIN diodes were used to monitor the pulse-to-pulse laser intensity during data taking.

Readout Electronics

To allow the trigger sufficient time to form the logical signal that was used to select events, the signals from CCAL's PMTs were delayed by 300 ns of cable. The coaxial cable used to delay the CCAL signals introduced a frequency dependent attenuation to the pulse shapes produced by the PMTs. The pulse tail was extended to over 600 ns. Even with a small FERA gate ($\sim$ 100 ns), as required by E835's running conditions, this long tail introduced extra clusters into events.

To eliminate these extra clusters, a passive filter was introduced between the PMTs and the FERAs. This filter reduced the tail of the signal by reshaping the pulses from the CCAL. The shaper circuit sent most of the signal to a FERA and a small part of the signal to a 6mV ($\sim$ 12 MeV) discriminator connected to a TDC.

There were 80 shaper boards for the CCAL, with each shaper board having 16 channels. Figure 2.11 shows one shaper channel and Figure 2.12 shows the traces for the reshaped pulse and the input pulse for a shaper circuit.

Clusterization

Each energy deposit in the CCAL was subjected to a clusterization algorithm to determine the energy and position information for the deposits. For every event, the CCAL was scanned for local maxima. Each local energy maximum, called a *seed*, was subjected to an analysis dependent energy threshold. If the seed was above this threshold the 3×3 grid, with the seed at the center, was called a *cluster*. The energy of the cluster was also subjected to a threshold. Analyses concerned with low energy photons, like the $\gamma\gamma$ analysis, used 5/20

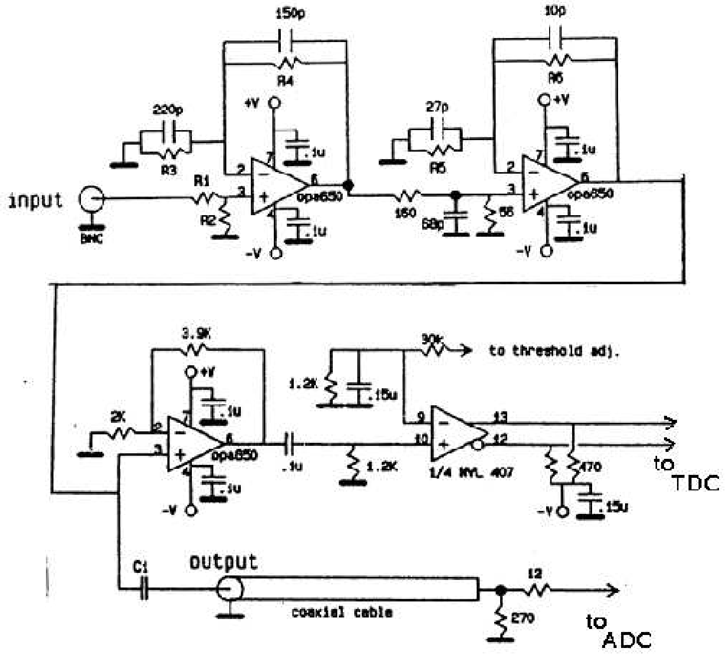

Tube diameter	R1	R2	R3	R4	R5	R6	C1
(3") 1	24	27	1.2K	1.0K	1.3K	1.3K	22nF
(2") 2	30	20	1.2K	680	820	1.5K	22nF
(1.5") 3	30	18	910	680	680	1.5K	18nF

Figure 2.11: A circuit diagram of the shaper. One channel is shown, along with the potentiometer that controls the discriminator threshold for all 16 channels and the power connection.

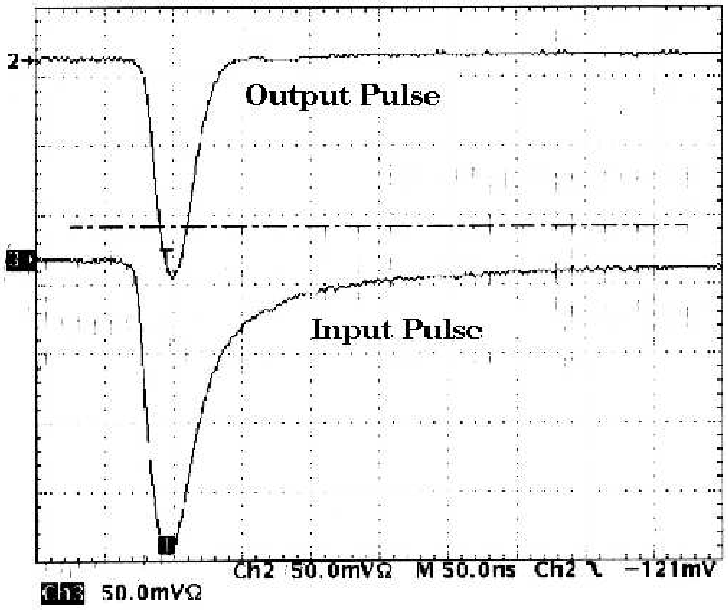

Figure 2.12: Oscilloscope trace showing the reshaped pulse (upper) and the input pulse (lower) of the shaper circuit. The pulse is from ∼1 GeV pulse from a 3 in. PMT in ring 10.

MeV (seed/cluster) thresholds, while most other analyses, including this one, used 25/50 MeV thresholds.

There were three categories of clusters, isolated, shared, and split. Each one required a different treatment. Isolated clusters had only one local maximum in the 5×5 grid with the seed at the center. A zeroth order cluster position was determined by the energy weighted average:

$$\bar{x} = \frac{\sum_i E_i x_i}{\sum_i E_i} \quad , \quad \bar{y} = \frac{\sum_i E_i y_i}{\sum_i E_i} \tag{2.8}$$

where E_i is the energy deposited in the i^{th} block in the cluster and x_i (y_i) is the distance in θ (ϕ) in block units from the seed, *ie.* $\bar{x}, \bar{y} \in \{-1, 0, 1\}$. The cluster energy was calculated as the sum of the energy deposited in the 3×3 grid of the cluster:

$$E_{sum} = \sum_{i=1}^{9} E_i \tag{2.9}$$

The support structure of the CCAL introduced cracks between the blocks. About 2% of the surface area in the ring (ϕ) and ~0.5% in the wedge (θ) direction was made of steel. Energy that was lost in these cracks lead to an incorrect calculation of the position and energy of the clusters. Both position and energy corrections were made to remedy the calculation.

The position of the center of the cluster was corrected by using:

$$x' = A_w(1 - e^{-\bar{x}/a_w}) + B_w(1 - e^{-\bar{x}/b_w}) \tag{2.10}$$

$$y' = A_r(1 - e^{-\bar{y}/a_r}) + B_r(1 - e^{-\bar{y}/b_r}) \tag{2.11}$$

where x' (y') is the distance in the wedge (ring) direction, in block units, from the center of the block. A clean sample of $J/\psi \to e^+e^-$ was used to empirically determine the functional form and the constants [39]. These constants are listed in table 2.3.

The corrected cluster energy is given by:

$$\begin{aligned} E &= f_{corr} E_{sum} \\ &= E_{sum} \left[(1 - C_{high(low)} e^{-|x^*|/c_{high(low)}}) \right. \\ &\left. \times (1 - D_1 e^{-|y^*|/d_1} - D_2 e^{-|y^*|/d_2}) \right]^{-1} \end{aligned} \tag{2.12}$$

A_r	724.4	a_r	0.03208
A_w	706.5	a_w	0.03969
B_r	123.6	b_r	0.1860
B_w	102.6	b_w	0.1715
C_{low}	0.0614	c_{low}	7.367
C_{high}	0.0857	c_{high}	19.690
D_1	0.14736	d_1	48.908
D_2	0.15935	d_2	12.761

Table 2.3: Constants used in the CCAL clusterization algorithm.

where x^* and y^* are the distances from the closest edges of the block. With staggered ring faces, the energy loss was different and was treated as such in the *higher* and *lower* θ directions. Using $J/\psi \to e^+e^-$ data, one can predict the energy of the particles that shower in the CCAL from the measured θ. Figure 2.13 is a comparison between the measured and predicted cluster energy, before and after the crack correction, as a function of the distance from the crack.

Clusters that were considered shared had two local maxima in a 5×5 grid. That is, shared clusters were identified as two separate clusters whose 3×3 grids overlapped. The energy in the common blocks would be shared and the two cluster's energies and positions would be calculated incorrectly by the isolated clusterization algorithm. An iterative process was developed to take into account shared clusters. The process is as follows:

1. The cluster positions and energies were calculated assuming they were isolated clusters. The energies in the shared blocks were counted twice.

2. These positions and energies were used to calculate the fraction of the energy shared, $f_{i,m}$, for each block, i, in each cluster, m. The fraction is given by:

$$f_{i,m} = \frac{E_m e^{-(|\delta_{x_{i,m}}|+|\delta_{y_{i,m}}|)/0.17}}{E_1 e^{-(|\delta_{x_{1,m}}|+|\delta_{y_{1,m}}|)/0.17} + E_2 e^{-(|\delta_{x_{2,m}}|+|\delta_{y_{2,m}}|)/0.17}} \tag{2.13}$$

   where E_m is the total energy of cluster m, the distances $\delta_{x_{i,m}}$ and $\delta_{y_{i,m}}$ were measured along the ring and wedge axis from the middle of the block respectively, and the constant, 0.17, was determined empirically from $J/\psi \to e^+e^-$ events. The form of Eq. 2.13 assumes that as the distance from the center

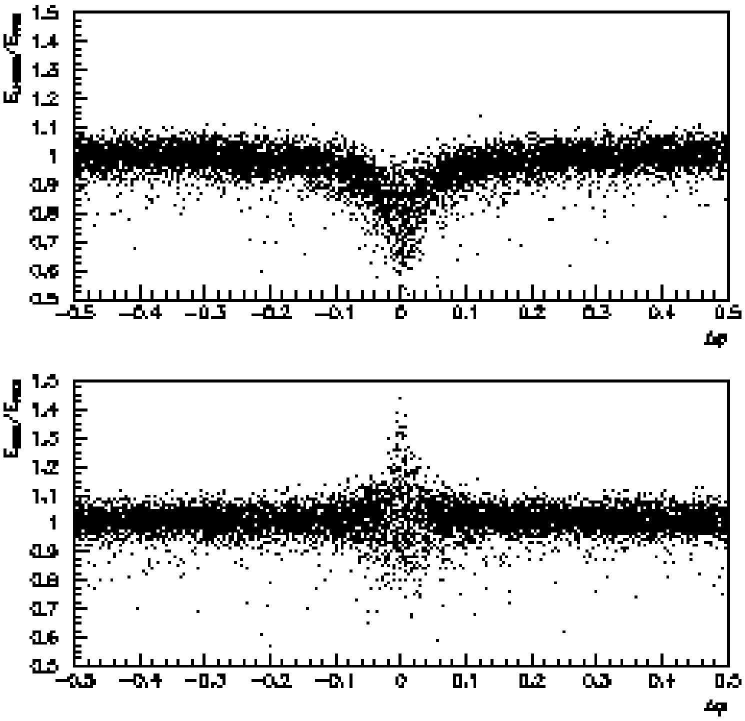

Figure 2.13: The ratio between the measured and predicted cluster energies as a function of the distance, in block units, from the crack. The data is from $J/\psi \to e^+e^-$ decays. Note: The energy resolution is much better near the center of the block

block increases the amount of energy deposited decreases exponentially in each direction. Finally, if the block under consideration was not contained in the 3×3 grid of cluster m, *ie.* the block only belonged in the other cluster, $f_{i,m} = 0$.

3. The energies and positions were recalculated with the following modifications made to equations 2.8 and 2.9:

$$\bar{x}_m = \frac{\sum_i f_{i,m} E_i x_i}{\sum_i f_{i,m} E_i} \quad , \quad \bar{y}_m = \frac{\sum_i f_{i,m} E_i y_i}{\sum_i f_{i,m} E_i} \tag{2.14}$$

$$E_{sum,m} = \sum_i f_{i,m} E_i \tag{2.15}$$

   With these updated positions and energies, the crack correction was recalculated.

4. Steps 2 and 3 were repeated until there was convergence.

Convergence of the sharing process was achieved when the total energy for each cluster changed by less than 30 MeV and the polar and azimuthal positions changed by less than 5 mrad each. Typically, convergence was achieved after 2-4 iterations. If a set of clusters reached the 10th iteration in the sharing algorithm, the process was terminated and the values calculated in the last iteration were retained.

Split clusters contained the energy from 2 particles, but there was only one local maximum in the 5×5 grid. These clusters were assumed to be from symmetrically decaying π^0s. At E835's highest energies, the minimum $\pi^0 \rightarrow \gamma\gamma$ opening angle was approximately 1.5 blocks wide. If a π^0 decayed symmetrically and the photons entered diagonal blocks, only one maximum would be produced. The difference between an isolated and a split cluster was its "mass". For each cluster, a quantity called the cluster mass was calculated:

$$M_{cl} \equiv \sqrt{\left(\sum_i E_i\right)^2 - \left(\sum_i \vec{p_i}\right)^2} \tag{2.16}$$

where the sum is over the 5×5 grid, E_i is the energy deposited in the i^{th} counter, and $\vec{p_i} = E_i \hat{r}_i$ where $\hat{r}_i$ is the unit vector from the interaction point to the center of the block. Figure 2.14 shows the cluster mass distribution for electrons

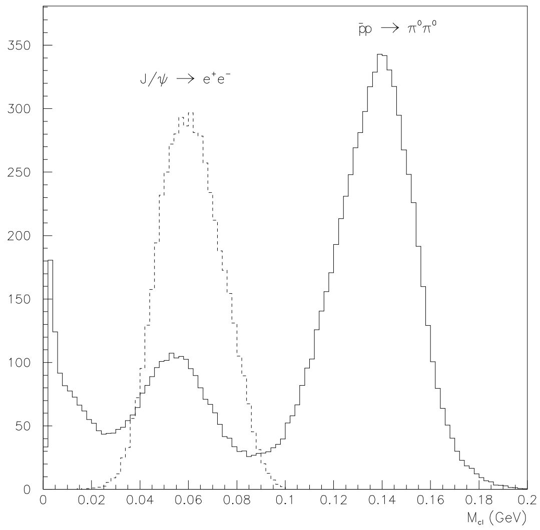

Figure 2.14: Cluster mass distributions for $\bar{p}p \rightarrow \pi^0\pi^0$ events (solid) and $J/\psi \rightarrow e^+e^-$ events (dashed). The large peak is from symmetrically decaying π^0s.

from $J/\psi \rightarrow e^+e^-$ events and from $2\pi^0$ events. The right hand peak in the $2\pi^0$ histogram is from symmetric π^0 decay where the two photons have merged into a single cluster. The small peak in the π^0 sample is from asymmetric π^0 decays where both photons form isolated clusters and were both in the calorimeter. In order to not affect the electrons, only clusters with $M_{cl} > 100$ MeV were split.

Clusters with $M_{cl} > 100$ MeV were split in order to calculate a more accurate position and energy, and thus identify events with symmetric π^0 decays. The sharing algorithm was difficult to use for clusters with a large overlap, therefore, the the sharing algorithm was modified. First, the block diagonal to the maximum with the highest energy deposit was defined as the second center (seed). Each seed was only included in the cluster that it belonged to when the sharing fractions, $f_{i,m}$, were calculated. Also, the sharing algorithm was extended to the 5×5 grid. Enlarging the grid maximized the information from the portion of the tail not masked by the other cluster. The remaining procedures of the sharing algorithm were carried out as already described. The splitting procedure allowed the recovery of π^0s that would otherwise have been removed on kinematical grounds, see Figure

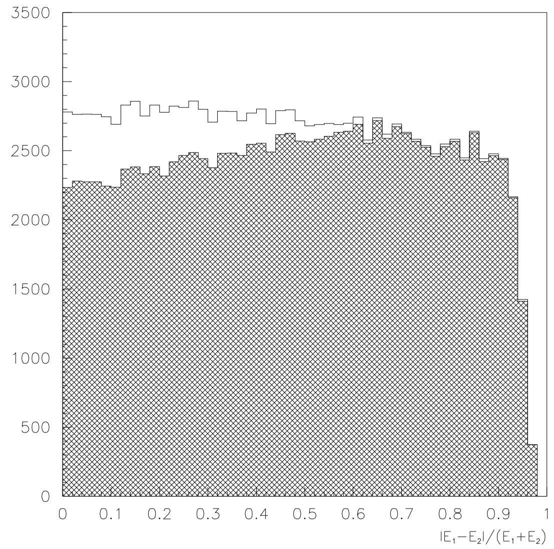

Figure 2.15: Asymmetry for π^0s with (unshaded) and without splitting. Missing events at asymmetry near 1 had low energy photons that either missed the CCAL or were below threshold.

2.15.

Timing and Resolution

The high luminosities E835 ran at required the use of timing information in order to separate meaningful signals from noise or from signals that were not associated with an event. For example, The information in an event could be contaminated by signals from different events sharing the same FERA gate. This could happen if a previous event, which need not have caused a trigger, contained a cluster in the CCAL with a long tail. The tail would then be recorded as a cluster by the FERA in the next event if the tail was still above threshold. The use of TDCs allowed the reduction of the FERA gate from 200 ns to 100 ns and also the separation of "in-time" clusters from other spurious out-of-time clusters.

The time of a cluster was defined as the time associated with the highest energy block in the cluster. Pulses with different amplitudes cross the TDC threshold at different times, with respect to the start of the signal, and a pulse-height dependent (slew) correction was applied to improve the timing resolution [40]. If a cluster had no timing information, then the cluster was called "undetermined". Undetermined clusters were common, were usually of low energy, and occurred when the amplitude of the pulse was below the timing threshold. If a cluster had a TDC hit that was outside of the timing window (± 10 ns), it was called "out-of-time".

For the 2000 run, the CCAL energy and position resolution was calculated by using $\psi' \to e^+e^-$ data (by finding the deviation of the events from two body kinematics) and it was found to be consistent with previous measurements from $J/\psi \to e^+e^-$ data [41, 31]. The resolutions were 6 mrad for θ, 11 mrad for ϕ and the measured energy resolution was:

$$\frac{\sigma_E}{E} = \frac{6.0\%}{\sqrt{E(GeV)}} + 1.4\%. \tag{2.17}$$

Complete discussions of the CCAL calibration, cluster parameter errors, and vertex determination are found in Chapter 3 of Reference [31].

2.4.5 Forward Calorimeter

The Forward Calorimeter (FCAL) was the secondary calorimeter in E835 and was primarily used as a veto. The FCAL was a planar array of 144 lead-glass blocks that covered polar angle between 2 and 12 degrees. Table 2.4 summarizes the three sizes of blocks used in the FCAL [42]. Reshaped signals[9] from FCAL's PMTs were sent to ADCs and TDCs.

Energy deposits in the FCAL were also subjected to a clusterization algorithm. The block which contained the largest deposit of energy was called the seed. If the seed block contained more than 25 MeV then the cluster energy was defined as the sum of the energy in the seed plus the energy in all of the seed's neighboring blocks. The cluster energy was subjected to a threshold of 50 MeV. Energy loss due to the cracks in the FCAL was not appreciable since they did not project back to the interaction vertex. The FCAL energy resolution was:

$$\frac{\sigma_E}{E} = \frac{6\%}{\sqrt{E}} + 4\% \tag{2.18}$$

[9]The shaper boards in FCAL were the same as those in CCAL.

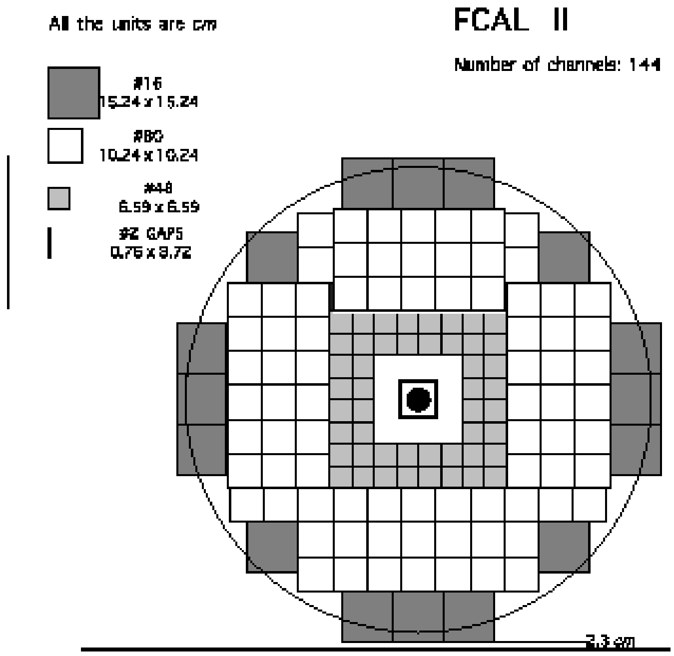

Figure 2.16: Layout of the Forward Calorimeter. The circle on the figure represents where the CCAL overlapped the FCAL.

	Cross. Sect. (cm^2)	Length (cm)	X_0	Glass Type	PMT Type
48 "small"	6.3×6.3	58.6	21	SF2	RCA 6342A (2.5 in.)
80 "medium"	10×10	38.0	14	Schott SF2	RCA 6342A (2.5 in.)
16 "large"	15×15	36.1	13	SF2	RCA 4335 (5in.)

Table 2.4: Summary of the FCAL block characteristics.

A zeroth order cluster position was determined by calculating the cluster's center of gravity based on the center position of the neighbors. A correction to the position determination was applied on the basis of a uniform minimum bias event distribution [43]. Figure 2.17 shows a clear improvement in the hit distribution uniformity for events with the correct position.

Timing information was obtained for each FCAL cluster. TDC hits were analyzed for the two highest ADC count blocks. The hit closest to the event time was accepted as the cluster time. A slew correction was implemented to improve the timing resolution of the FCAL and allowed the timing window to be reduced from ± 20 ns to ± 10 ns, see Figure 2.18.

Data taken at the χ_{c1} (3510 MeV) was chosen for the FCAL calibration. Events with 5 photons in the CCAL and 1 photon in the FCAL were selected. Each event was subjected to a 5 constraint kinematic fit to the hypothesis of $\pi^0\pi^0 + \pi^0$, $\pi^0\eta + \pi^0$, or $\eta\eta + \pi^0$, where two CCAL clusters were required to form an invariant mass near either the π^0 or η mass. Clear π^0 and η mass peaks can be seen in Figure 2.19 in the $\sim$ 100 and $\sim$ 550 MeV energy regions respectively.

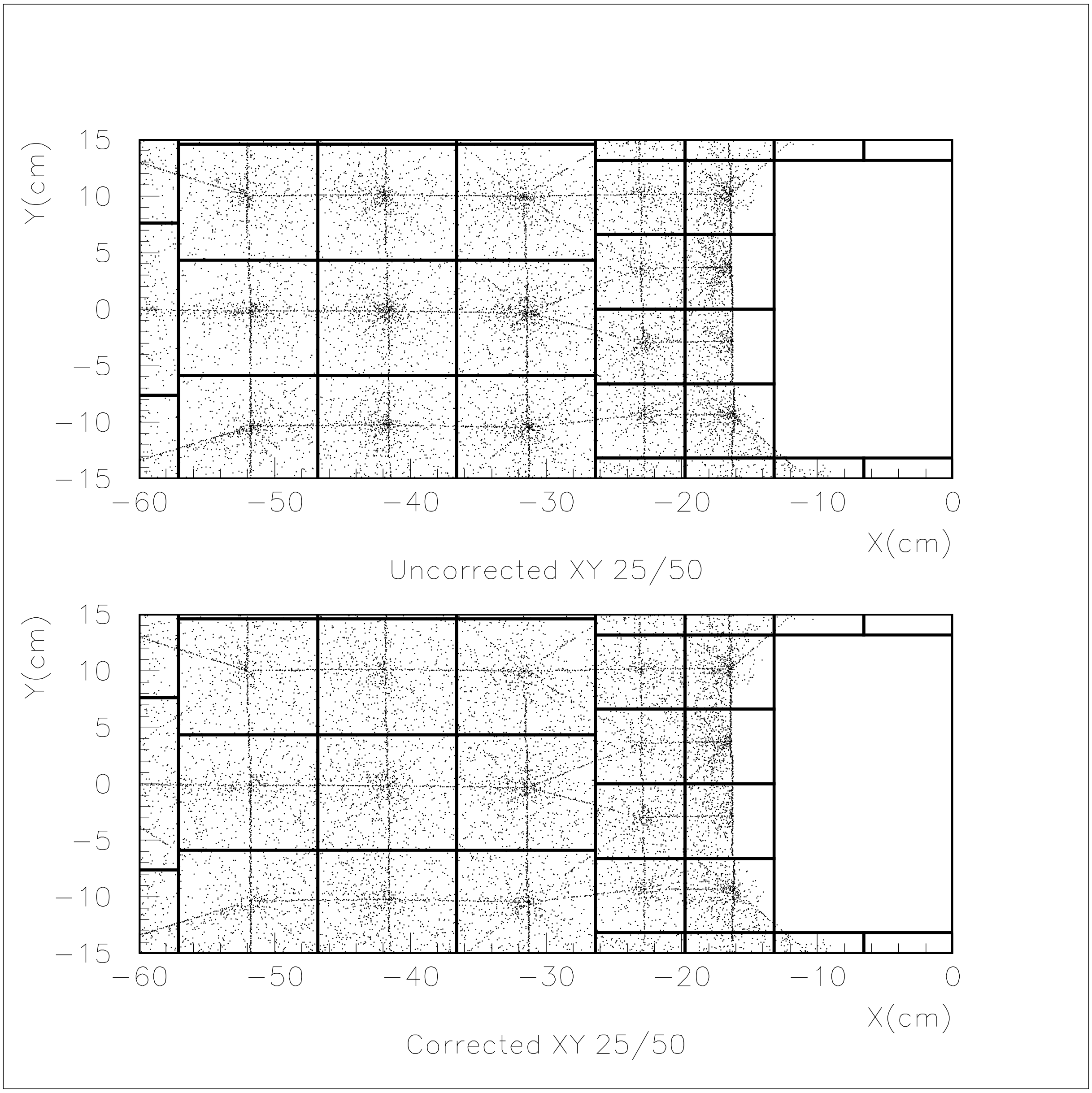

Figure 2.17: Partial hit distributions for minimum bias events in the FCAL. Top: Without position correction. Bottom: With position correction. A clear improvement is seen.

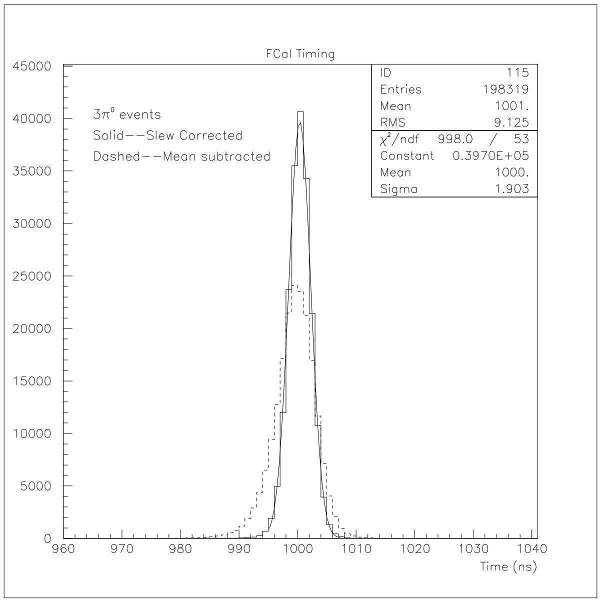

Figure 2.18: The cluster times for the 6γ FCAL calibration data. The dashed curve corresponds to raw times and the solid curve represents slew corrected times.

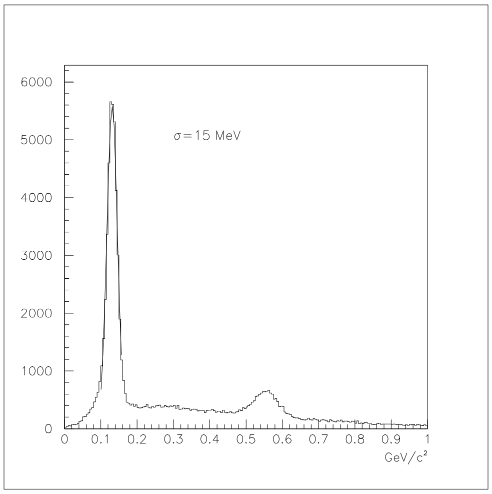

Figure 2.19: Two photon invariant mass distributions for FCAL calibration data where one photon is in the FCAL. The π^0 peak is fitted with a Gaussian.

Chapter 3

Data Acquisition

The data acquisition system (DAQ) used in E835 received information from four independent data sources. Three of these sources, the luminosity data source, the scalar data source, and the beam parameter data source were used to monitor the performance of the experiment. The luminosity data source contained information about the status of the Luminosity Monitor as well as other data collected to determine the interaction rate. The scalar data source measured activity rates of the triggers and the subdetectors in order to monitor the performance of the detector. The beam parameter data source was was received from the FNAL Beams Division through the Accelerator Control NETwork (ACNET) [44]. The beam parameter data source was used to monitor the status of the beam. Information collected by the beam parameter data source included the beam position, momentum, and it's spread, the beam emittance, and other similar information. The fourth data source, the event data source was responsible for collecting, packaging, and recording all of the interesting data produced by E835.

The event data source was based on DART (Data Acquisition for Real Time systems) [45] and is the focus of this chapter. The event data source can be divided into three major systems, data readout, hardware trigger, and software trigger. The data readout system collected, transferred, packaged and recorded the data from the detector that was selected by the hardware trigger. The hardware trigger studied each event from the detector and selected the events which had physically interesting topologies. The software trigger partially reconstructed the events selected by the hardware trigger in order to further purify and filter the data into three possible data types, neutral, charged, or $\phi\phi$.

3.1 Data Readout

The data readout system was responsible for collecting, transferring, packaging, and recording all data selected by the hardware trigger. An outline of the data readout system can be seen in Figure 3.1. There were three computers contained within the data readout system. Two SGI[1] Indigos were used for run control and system monitoring. A SGI Challenge-L, containing 12 R4400 150 MHz processors, was used for online data analysis. The Challenge-L was also used for streaming and writing the data selected by the software trigger to tape or disk.

Prior to readout, the signals from the individual detector elements were split. Five percent of the original signal was sent to the hardware trigger logic in order to determine if the event was of interest. The remaining 95% of the signal was passed through delay cables to the readout electronics. Both amplitude and timing signal were collected by E835. Situated in 19 CAMAC crates, 16-bit LeCroy 4300 and 4300b ADCs along with 16-bit LeCroy 3377 TDCs digitized the amplitude and timing signals from the individual detector channels and sent them through their ECL ports to Damn Yankee Converters (DYCs) [46]. The DYC, developed as part of the DART project, is a data buffer, which can simultaneously read and write, and used to convert the 16-bit output of the ADCs and TDCs into 32-bit words. When a DYC was receiving data, it sent a busy signal to the trigger logic which prevented the trigger from accepting events. The fraction of the time that the trigger was inhibited, the dead-time, was less than 5% for E835. For debugging and programming purposes, the ADCs and the TDCs were also connected through the CAMAC backplane via two SCSI Jorway interfaces.

Once the hardware trigger selected an event, the DYCs transferred their data, by RS-485 (DART) cables, in 2 independent streams to two DC2/DM115 modules housed in a VME crate. Each DC2 is connected, via the VME backplane, to a 8 MB and two 32 MB Dual Port Memory modules (DPM). The 32 MB DPMs are used to store information for N events while the 8 MB DPM is used as a "mailbox" for communication between the DC2s and the "gateway", a process

[1]Silicon Graphics Inc.

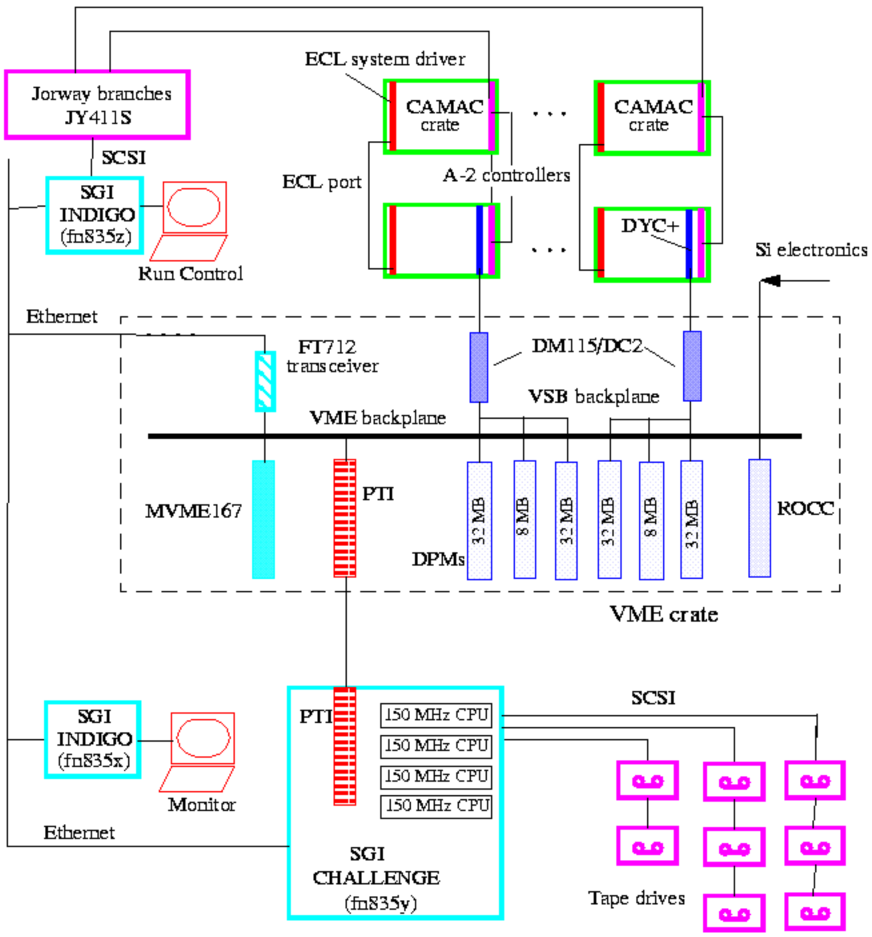

Figure 3.1: Schematic of the data readout system.

which ran on the Challenge-L that read the data from the DPMs. The DC2 used a "ping-pong" algorithm to fill the DPMs, *ie.* while one of the DPMs was being read by the gateway, the other DPM was being filled by the DC2.

Also contained within the VME crate was a Motorola MVME167 processor which was used by the gateway to combine information for each event from the corresponding DPMs and the hardware trigger in order to assemble all event information in the correct manner. Once the events were constructed, they were sent to the software trigger for online analysis and filtering. Finally, events which were selected and filtered by the software trigger were written, by the Challenge-L, to Exabyte 8500 8 mm tapes. Also, subsets of this data were simultaneously written to disk.

3.2 E835 Hardware Trigger

The E835 hardware trigger selected from the ~1 million interactions per second, those events which were most likely to include charmonium. Since the majority of $p\bar{p}$ interactions do not form charmonium, the process of selecting these events, reduced the interaction rate of ~1 MHz to the trigger rate of 2 kHz. The hardware trigger consisted of two branches, the charged trigger and the neutral trigger. The charged trigger used information from the Inner Detector and the Čerenkov Counter to identify events with charged particles in the final state. The neutral trigger used information from the CCAL to identify events with a large amount of the event energy in the CCAL and events with large energy deposits in azimuthally opposite portions of the detector (two-body events).

3.2.1 The Charged Trigger

There were two branches in the charged trigger [47] used to identify events that contained e^+e^- pairs, $p\bar{p}$ pairs, or $4K^\pm$ mesons (from the decay $\phi\phi \to 4K^\pm$). Information collected by the charged trigger from the 4 Hodoscopes (H1, H2, H2$'$, and FCH), the Čerenkov Counter, and the Scintillating Fiber Detector were combined into 12 different logic signals which were the input for 2 Memory Lookup Units (MLU). The Charged MLU (CMLU) was designed to look for electron and hadron pairs. The CMLU had 7 input signals. These signals, listed in table 3.1, were as follows:

- $1e$ (1 electron) $\leftrightarrow$ the AND of a 1h track and the OR of the upstream and downstream Čerenkov cells along the line of the track.
- $2e$ (2 electrons) $\leftrightarrow$ 2 "1e"s.
- $2ch$ (2 charged hadrons) $\leftrightarrow$ 2 ANDs between separate H1 elements and 6 H2 elements along the line of the track (the 4 elements within the solid angle covered by the H1 element as well as the 2 adjacent H2 elements).
- Inputs 4, 5 were for events that had hits in 2 or <6 elements in H2.
- $COPL$ (coplanarity) $\leftrightarrow$ the AND between a H2 element and the OR of 3 coplanar H2 elements.
- Input 7 was for events that had hits in any element of the Forward Charged Hodoscope.

The CMLU used these 7 inputs to form 7 physics signals. The outputs of the CMLU were:

- e^+e^- (1) $\leftrightarrow$ $2e \otimes (H2 < 6) \oplus 1e \otimes 2h \otimes (H2 = 2) \otimes COPL$
- e^+e^- (2) $\leftrightarrow$ $2e \otimes (H2 = 2) \otimes COPL \otimes \overline{FCH}$
- $\phi\phi(1)$ $\leftrightarrow$ $2h \otimes COPL \otimes \overline{FCH}$
- $p\bar{p}$ $\leftrightarrow$ $2h \otimes (H2 = 2) \otimes COPL \otimes \overline{FCH}$
- $unnamed$ $\leftrightarrow \overline{1e} \otimes 2h \otimes (H2 = 2) \otimes COPL$
- $p\bar{p}$ 90 $\leftrightarrow (PPbar90bundle) \otimes \overline{H2} \otimes (SF = 1)$, where $PPbar90bundle$ refers to the scintillating fiber bundle that corresponded to 90° in the center of momentum frame for $\bar{p}p \to \bar{p}p$ events.
- $p\bar{p}$ 55 $\leftrightarrow (PPbar55bundle) \otimes \overline{H2} \otimes (SF = 2)$, where $PPbar55bundle$ refers to the scintillating fiber bundle that corresponded to 55° in the center of momentum frame for $\bar{p}p \to \bar{p}p$ events.

The ΦMLU also used information from the inner detector, but it was strictly designed to identify the kinematics of 2 ϕ mesons decaying into $4K^{\pm}$ mesons. The ΦMLU had 5 inputs[2], listed in table 3.1, when combined formed 1 output signal:

- $\phi\phi(2) \leftrightarrow H2_{\phi\phi} \otimes (H2 = 3,4) \otimes (SF = 3,4) \otimes (H2 \oplus SF = 7,8) \otimes VETO_{\phi\phi} \otimes KIN_{\phi\phi}$

Input Channel	Description	Output Channel	Description
Charged MLU			
1	$1e$	1	$e^+e^-(1)$
2	$2e$	2	$e^+e^-(2)$
3	$2ch$	3	$\phi\phi(1)$
4	$NH2 = 2$	4	$p\bar{p}$
5	$NH2 < 6$	5	*unnamed*
6	$COPL$	6	$p\bar{p}$ 90
7	FCH_OR	7	$p\bar{p}$ 55
ΦMLU			
1	$VETO_{\phi\phi}$	1	$\phi\phi(2)$
2	$NH2_{\phi\phi}$		
3	$NH2 = 3,4$		
4	$KIN_{\phi\phi}$		
5	$NSF = 3,4$		

Table 3.1: Inputs and Outputs of the Charged and Φ MLUs.

Once these eight signals were constructed, the CMLU and ΦMLU sent their output signals to the Master MLU which combined them to form the final e^+e^-, $p\bar{p}$, and $\phi\phi$ hardware trigger signals, see Section 3.2.3.

3.2.2 The Neutral Trigger

The Neutral Trigger (Figure 3.2) used the 1280 signals from the CCAL to identify events which had back-to-back or multi-photon final states [48, 49]. The neutral

[2]The specific construction of the inputs for the ΦMLU are discussed in detail in Reference [47].

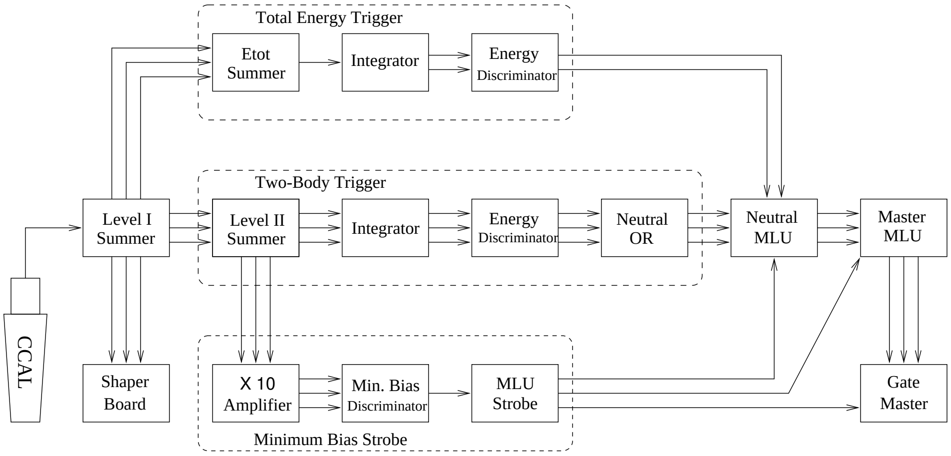

Figure 3.2: Schematic of the Neutral Trigger.

trigger contained two independent trigger types, PBG[3] and ETOT. The PBG branch was designed to identify two-body ($\gamma\gamma$ and e^+e^-) events. The ETOT branch summed the energy in the CCAL and identified events with multiple photon final states ($\pi^0\pi^0$, $\eta\eta$, *etc...*). The ETOT branch was not limited by the number of final state particles and required events to have a large fraction of the event energy in the CCAL. In order to allow the Gatemaster to synchronize all of the triggering processes, a minimum bias strobe was also included in the neutral trigger.

The PBG branch of the trigger combined the CCAL signals with a 2 stage analog summing unit (summer) which combined the analog signals from the CCAL into 5 *super-rings* and 8 *super-wedges* or 40 *super-blocks*. The reduction in the number of input channels allowed the neutral trigger to select events more quickly than when all 1280 CCAL signals were used independently. Each super-wedge (see table 3.2) contained the information from 9 wedges and each super-ring contained information from 5 rings[4] (table 3.3). In the super-ring (super-wedge) direction each super-block overlapped it's neighboring super-block by 1 ring (wedge), as characterized in Figure 3.3. The overlaps reduced an inefficiency caused by events

[3]PBG stands for Pb-glass.

[4]Super-ring 1 only contained information from rings 1-4.

where particles hit the super-block borders. In this class of events, a large percentage of the energy deposited would spread across more than 1 super-block. A ring-sum, with no overlap, was also performed by the summers to produce signals for the ETOT branch.

Super-Wedge	Included Wedge Numbers
1	1-9
2	9-17
3	17-25
4	25-33
5	33-41
6	41-49
7	49-57
8	57-1

Table 3.2: Individual wedges included in each super-wedge.

Super-Ring	Included Ring Numbers
1	1-4
2	4-8
3	8-12
4	12-16
5	16-20

Table 3.3: Individual rings included in each super-ring.

The output of the summer were the analog signals of the super-blocks and the ring-sums were formed as input to the integrator modules that converted the super-blocks and ring-sums to signals with amplitudes proportional to the total energy. These amplitudes are independent of the pulse shapes that come from the PMTs. The use of the Integrator modules was necessary because of the different PMTs used in the CCAL. If the uncorrected signal amplitudes were used an inefficiency in the neutral trigger would have been introduced, due to the inability to apply proper and universal discriminator thresholds.

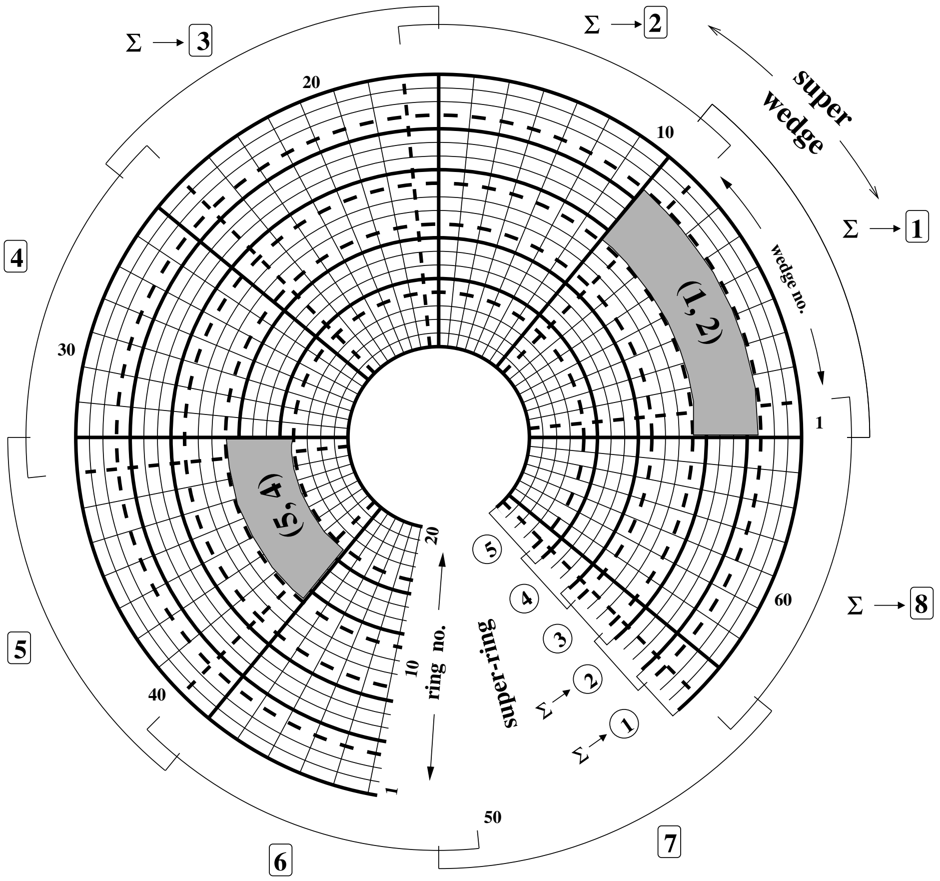

Figure 3.3: Super-block positions in the CCAL as defined by the neutral trigger summers. Each block is segmented in super-block units of θ and ϕ. Super-blocks $\{1, 2\}$ and $\{5, 4\}$ are shaded.

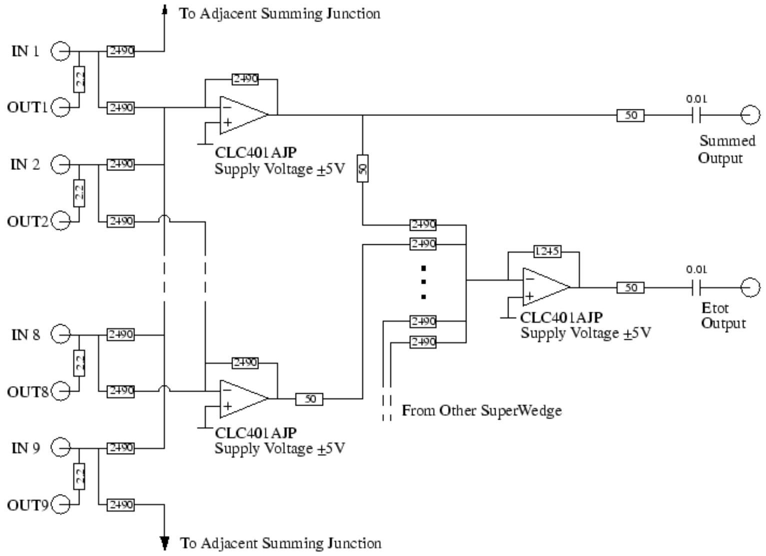

Figure 3.4: Circuit diagram of the Neutral Trigger's Level I Summer. All resistances are in ohms and all capacitances are in pico-Farads.

After the super-block signals were sent through the Integrator modules and energy discriminated, the 40 super-block signals were sent into the Neutral_OR Module (NORM) to form 8 CCAL super-wedge signals. If one super-block in the super-wedge was above threshold, then the neutral_OR bit for that super-wedge was set.

Finally, the neutral_OR and the ETOT signals were passed on to the Neutral MLU which used the input signals to develop four level 1 hardware triggers; ETOT-HI, ETOT-LO, PBG1, and PBG3. These trigger signals were then sent to the Master MLU.

Level I Summer

The Level I Summer was used to sum the signals from the CCAL into ring-sums and super-wedges. The CCAL's signals arrived to the 128 channel summers via RG-174 cables. Signals from exactly 2 wedges were connected to each summer module. The circuit diagram for the Level I Summer is illustrated in Figure 3.4.

The output of the CCAL's PMTs were the input of the Level I Summer. The CCAL signals were split. Ninety-five percent of the input signal was sent into delay cables and to the shaper boards (detailed in Section 2.4.4). The remaining 5% of the signal was used by the Summer. The signal from each block was summed with the signals from all of the other blocks in the same ring to form the 20 ring-sums.

The other operation of the Level I Summer was forming 8 super-wedges with the information from the CCAL wedges. Each super-wedge contained information from 9 wedges and overlapped it's adjacent super-wedges by 1 wedge. If the wedge being summed was to be shared by two super-wedges, then half of the signal was sent to each super-wedge. In order to insure stability, if the wedge was not shared then half of the signal was sent to the super-wedge while the other half was discarded. The total output of the Level I Summer was 8 super-wedges and the 20 ring-sums. The 160 ring/super-wedge signals were sent to the Level II Summer and the 20 ring-sums were sent to the ETOT Summer.

Level II Summer

The Level II Summer consisted of 8 units, each of which were connected to the signals from one super-wedge. Ninety-five percent of the signal that entered the Level II Summer were sent to a inverting feedthrough where the signals were reinverted and amplified by a factor of 1.5. The signals were then sent to discriminators with a 17 mV threshold. This "minimum bias" threshold was used to determine the event time.

The partial signal (5%) used by the Level II Summer was summed in a similar manner as the signals entering the Level I Summer. Super-rings were formed by summing 5 rings, except SR1 which had 4 rings, with an overlap of 1 ring. As in the Level I Summer, the signals were split before they were summed, with the overlapped rings sending half of their signal to each super-ring and the non overlapped rings discarding half of their signal. The average particle energy in each ring was different for two-body events. In order to set a single super-ring energy threshold, the ring signals were weighted with resistors.

The signals from the shared rings had different weights depending on which super-ring was under consideration. The values of the resistors are listed in table 3.4. Due to the homogeneity of the CCAL only 1 set of resistors was required. Figure 3.5 shows a study of the CCAL energy deposits versus ring number for $J/\psi \to e^+e^-$ Monte Carlo events. The presence of the resistors in the trigger logic allowed a single energy threshold for each super-ring. After the super-rings were formed, the weighted and summed signals were inverted and amplified to produce 40 super-block sums. These sums were arranged in 5 super-rings of 8 super-wedges and contained all of the energy deposited in the CCAL.

The super-block sums were fanned out 3 times. The first fan-out went to the Integrator Module, which is described below. The second fan-out, used to monitor the neutral trigger and the energy thresholds, was directed to an ADC. The third fan-out was delayed by 100 ns and then sent to an ADC to monitor event overlap.

Integrator Module

Each super-ring in the Neutral Trigger contained different types of PMTs that had different pulse shapes. Rather than set multiple discriminator thresholds to reflect this, a universal threshold was used by introducing an integrator circuit into the NT logic. The Integrator Module integrated the charge in the pulse, which is proportional to the amount of energy deposited in a CCAL block, to produce an independent pulse-shape.

To perform the integration, a bipolar signal was created by clipping the current from the input signal with a shorted 16 ns cable[5]. The bipolar signal was then integrated with a time constant of 500 ns. Despite this large integration time constant, the clipping cable brought the output from the integrator back to it's baseline in $\sim$ 100 ns. The charge to voltage conversion of the integrator was constant up to $\sim$ 500 pC at about 2 mV/pC (see Figure 3.6). After the integration, the super-block signals were sent to the Energy Discriminators.

Energy Discriminators

After passing through the Integrator Modules, the 40 super-block signals were sent to one of four 16 channel LeCroy 4413 CAMAC discriminator modules. The signals from the 8 super-wedges in a super-ring were connected to the same discriminator. The other 8 channels in the discriminator were unused. The energy thresholds depended upon which super-ring was being analyzed as well as the

[5]The current was clipped before the integration in order to reduce pile-up in the integration capacitor.

Ring Number	Resistor Value (ohm)	Relative Weight
1	2260	1.10
2	2490	1.00
3	2740	0.91
4	3090,2050	0.81,1.21
5	2260	1.10
6	2490	1.00
7	2740	0.91
8	3010,2100	0.83,1.19
9	2320	1.07
10	2490	1.00
11	2610	0.95
12	2740,2260	0.91,1.10
13	2370	1.05
14	2490	1.00
15	2610	0.95
16	2670,2370	0.93,1.05
17	2430	1.02
18	2490	1.00
19	2550	0.98
20	2610	0.95

Table 3.4: The ring number, resistance, and relative weight of the resistors in the Level II Summer. The relative weight is calculated by finding the ratio of the given resistor to the resistor in the central channel of the super-ring. The overlapping rings had 2 resistors.

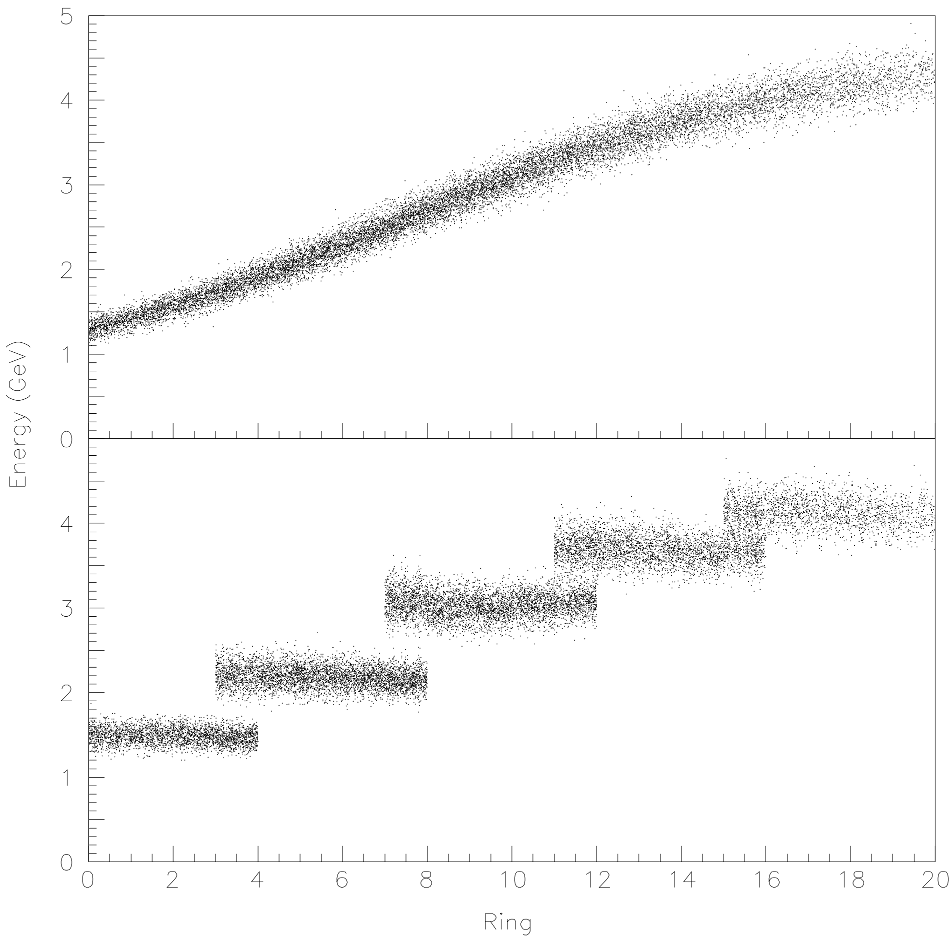

Figure 3.5: Particle Energy vs. ring number for $J/\psi \to e^+e^-$ MC events. The upper (lower) plot is without (with) the weighting resistors.

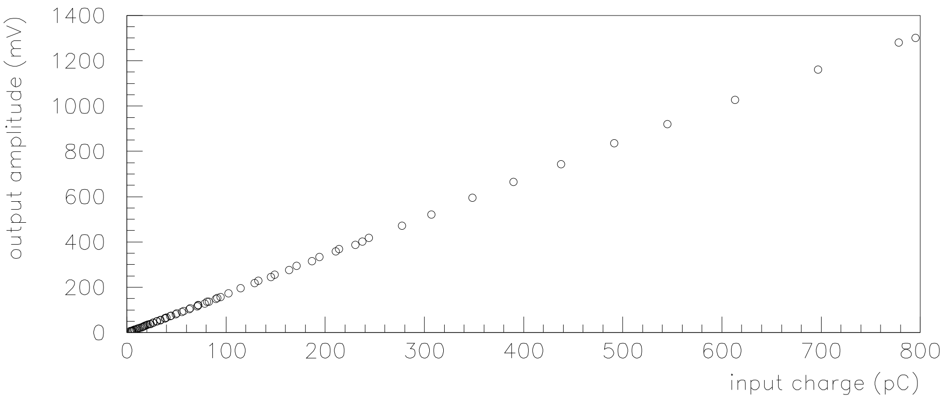

Figure 3.6: Charge to voltage conversion for the Integrator Module.

center of mass energy.

Energy thresholds were determined by generating Monte Carlo events in 5 MeV steps, in the center-of-mass energy range, 2.9 to 4.2 GeV. In each charmonium resonance region, a different decay mode was studied based on the partial widths of the resonance in question. The lowest threshold (SR1) was determined by finding the mean value of the energy deposit expected within SR1 for the $two-body-like$ events and then subtracting 3σ. The actual energy threshold was set to 60% of this energy threshold. The 40% reduction was necessary in order to take into account the energy loss in the CCAL due to the inactive material (cracks). Every super-ring had a different energy threshold for each resonance, table 3.5.

Neutral OR Module

The 40 output signals from the energy discriminators were sent to the 5 OR modules that made up the Neutral OR Module. Each OR module contained signals for 1 super-wedge. The output of the Neutral OR Module represented the energy deposited, above threshold, in each azimuthal octant of the calorimeter. The output of the Neutral OR Module was sent to the Neutral MLU.

Channel	Energy threshold (GeV) (60% of min. energy)					Energy discriminator threshold (mV)				
	SR1	SR2	SR3	SR4	SR5	SR1	SR2	SR3	SR4	SR5
$\eta_c \to \gamma\gamma$	0.70	1.05	1.46	1.79	—	52	81	119	146	—
$\psi \to e^+e^-$	0.72	1.08	1.54	1.91	—	53	84	125	155	—
$\chi_{c0} \to \gamma\psi$	0.61	0.95	1.41	1.81	2.09	45	73	115	147	217
$\chi_{c1} \to \gamma\psi$	0.57	0.89	1.34	1.74	2.03	42	69	109	142	212
${}^1P_1 \to \pi^0\psi$	0.56	0.88	1.33	1.73	2.02	41	69	108	141	210
$\chi_{c2} \to \gamma\psi$	0.54	0.87	1.31	1.70	1.99	40	67	106	138	207
$\eta_c' \to \gamma\psi$	0.53	0.84	1.28	1.68	1.97	39	65	104	136	205
$\psi' \to X\psi$	0.55	0.88	1.35	1.80	2.17	41	68	110	146	225

Table 3.5: Neutral Trigger discriminator and energy thresholds set for each super-ring for different charmonium resonances based on the two-body kinematics. Where SR stands for super-ring and for the $\chi_{c0,1,2}$, ${}^1P_1$ reactions, the J/ψ decays to e^+e^-.

Total Energy Summer

The Total Energy Summer (TES) took the 20 ring-sums from the Level I Summer and used them to form a signal that represented the total energy deposited in the CCAL. The TES was constructed in the same manner as the Level I Summer. In a similar fashion to the Level II Summer, the signals were sent through an Integrator Module to remove the pulse-height dependence from the different sized PMTs. The output signal from the Integrator Module was then fanned out twice and sent to discriminators with thresholds set at 70% and 80% of the center of mass energy. The discriminator output was then sent to the Neutral MLU.

Neutral MLU

The Neutral MLU (NMLU) received the signals from the Neutral OR Module and the Total Energy Summer via ECL. The NMLU's inputs and outputs are listed in table 3.6. The signals received from the TES were passed through the NMLU and became the ETOT-HI (80%) and the ETOT-LO (70%) level 1 hardware triggers. The 8 octant signals from the NORM were subjected to pattern recognition in order to generate the PBG1 and PBG3 triggers. The PBG1 signal strictly tagged

Input Channel	Description	Output Channel	Description
1	CCAL octant 1	1	PBG1
2	CCAL octant 2	2	PBG3
3	CCAL octant 3	3	ETOT-HI
4	CCAL octant 4	4	ETOT-LO
5	CCAL octant 5	5	empty
6	CCAL octant 6	6	empty
7	CCAL octant 7	7	empty
8	CCAL octant 8	8	empty
9	ETOT-HI		
10	ETOT-LO		
11-16	empty		

Table 3.6: The inputs and outputs of the Neutral Memory Lookup Unit.

two-body events and required that two opposing octants contain energy deposits above threshold. The PBG3 signal was used to tag $J/\psi \to e^+e^-$ decays where the J/ψ recoiled off of a photon. Due to the Doppler-broadening in the $\gamma J/\psi$ events, PBG3 requirements were not as stringent as PBG1. The PBG3 signal required a large energy deposit in a super-wedge and either it's opposing super-wedge or a super-wedge adjacent to the opposing super-wedge.

3.2.3 Master MLU

The Master MLU (MMLU) was triggered by the minimum bias strobe from the Neutral Trigger. Once triggered, the MMLU combined the signals from the CMLU, ΦMLU, and NMLU to build the level-2 hardware triggers. The MMLU also sent a trigger to the Gatemaster, which was used to send gates to the readout electronics, for each event that was interesting enough be collected. The inputs and outputs of the MMLU are listed in table 3.7. The level-2 charged triggers were formed by the MMLU combining signals from the CMLU and ΦMLU. They were:

- $e^+e^- \leftrightarrow e^+e^-(1) \otimes PBG1 \oplus e^+e^-(2)$

Input Channel	Description	Output Channel	Description
1	PBG1	1	e^+e^-
2	PBG3	2	not used
3	ETOT-HI	3	$\phi\phi$
4	ETOT-LO	4	Neutral PBG1
5	H1 $\times$ H2'_OR	5	Neutral ETOT
6	FCAL_OR	6	not used
7	H2$>$ 2	7	ETOT-NOVETO
8	FCH_OR	8	ETOT-LO
9	e^+e^- (1)		
10	e^+e^- (2)		
11	$\phi\phi(1)$		
12	not used		
13	not used		
14	$\phi\phi(2)$		
15	not used		
16	not used		

Table 3.7: The inputs and outputs of the Master MLU.

- $\phi\phi \leftrightarrow \phi\phi(1) \otimes \phi\phi(2)$

The $p\bar{p}$ triggers formed by the CMLU were passed through the MMLU as output (table 3.7). For the neutral triggers, the MMLU combined the ETOT and PBG1 signals with the neutral veto signal defined as:

- $NV \leftrightarrow H1 \otimes H2' \oplus FCH$

The neutral triggers were:

- *Neutral PBG1*$\leftrightarrow PBG1 \otimes \overline{NV}$
- *Neutral ETOT*$\leftrightarrow$*ETOT-HI*$\otimes\overline{NV}$
- *ETOT-NOVETO*$\leftrightarrow$*ETOT-HI*$\otimes\overline{H2 \geq 2}$
- *ETOT-LO*$\leftrightarrow$*ETOT-LO*$\otimes\overline{NV}$

3.2.4 Gatemaster

The Gatemaster was used to generate a gate signal in order for the DAQ to read data collected from the detector. The minimum bias strobe activated the Gatemaster when a gate was to be sent to the readout electronics. The Gatemaster then read the data and passed it to PRUDE for analysis. The Gatemaster's 14 inputs are listed in table 3.8. Eight of the inputs came from the MMLU while the other 6 inputs were from special triggers used to monitor detector performance and check trigger efficiencies. These special triggers were:

- Laser Monitor$\rightarrow$ Described in Section 2.4.4, used to monitor the gain stability in the CCAL.
- Silicon Strobe$\rightarrow$ Not used.
- Minimum Bias$\rightarrow$ Used to check the trigger efficiency.
- Random Gate$\rightarrow$ Random gates were generated with a 10Hz pulser. The RGs were used to study rate dependent pile-up in the detector.
- FCAL Cosmic Ray$\rightarrow$ Not used.

Input Channel	Description	Input Channel	Description
1	e^+e^-	9	Laser Monitor
2	$\bar{p}p90^\circ$	10	Silicon Strobe
3	$\phi\phi$	11	empty
4	Neutral PBG1	12	Minimum Bias
5	Neutral ETOT	13	Random Gate
6	$\bar{p}p55^\circ$	14	FCAL Cosmic Ray
7	ETOT-NOVETO	15	High Rate Minimum Bias
8	ETOT-LO	16	empty

Table 3.8: The inputs of the Gatemaster.

- High-rate Min. Bias$\rightarrow$ Not used

After the gate was sent to the readout electronics, the Gatemaster entered INHIBIT mode for 10 μs to allow the CAMAC modules to reset. During the duration of this 10 μs all strobes were ignored. To allow PRUDE to autopass a certain percentage of events, the Gatemaster kept a trigger count for each input. The autopassed events were used to check trigger efficiencies.

3.3 PRUDE Software Trigger

The Program Rejecting Unwanted Data Events or PRUDE was developed to reduce the $\sim$2 kHz trigger rate to $\sim$500 Hz, the maximum tape writing speed for E835. This rate reduction was accomplished by studying software triggers that were generated on events surviving the hardware trigger procedure. By performing an online analysis, PRUDE generated software triggers.

PRUDE performed a simplified version of the CCAL clusterization algorithm, discussed in Section 2.4.4, to calculate cluster energies, masses, and positions. A cluster was defined in PRUDE as having a minimum of 75 MeV in the 3$\times$3 grid with a seed that had energy greater than 37 MeV. The position and energy of a cluster was calculated using Equations 2.8 and 2.9. Crack corrections to the energy and position were made and the cluster mass was calculated, though no splitting was performed. With these calculations, PRUDE formed the invariant mass of cluster pairs and defined acceptance windows of 100-170 MeV for π^0s and 450-650 MeV for ηs. PRUDE also defined exclusive π^0s and ηs. Exclusive formation was tagged when the constituent clusters did not form any other acceptable π^0 or η invariant mass with other clusters in the event.

The invariant masses along with the information from the hardware trigger was then used to decide on which software trigger (PRUDE ID) should be assigned to the event. If multiple software triggers were satisfied for an event, the PRUDE ID with highest priority (lowest number) was assigned.

Once the PRUDE ID was assigned to an event, it was channeled into one of 3 data streams, GK, GP, or GN. The GK data stream contained charged events, the GP data stream contained $\phi\phi$ and $\bar{p}p$ events, and the GN stream contained neutral events. Defined within these three streams, there were two subsets of data, "gold" and GNA. The gold events (explained below) were written directly to disk for quick access. The other subset, GNA, was used for CCAL calibration. A final selection of events, the autopasses, were assigned to PRUDE's output streams without receiving software triggers. The PRUDE software triggers, including the autopasses, are listed in table 3.9. Ordered by priority, the software triggers generated by PRUDE were:

- goldee$\leftrightarrow$ Gatemaster input 1 (GM1) (e^+e^-) where at least one invariant mass pair >2.2 GeV.
- elec$\leftrightarrow$ GM1 events where all invariant mass pairs were less than 2.2 GeV.
- $\phi\phi$ $\leftrightarrow$ GM3 ($\phi\phi$) events were selected based on the kinematics, opening angles, and occupancy of the Hodoscopes and Scintillating Fiber Detector.
- goldgg$\leftrightarrow$ GM4 (Neutral PBG1) or GM5 (Neutral ETOT) where at least one invariant mass pair was >2.7 GeV.
- etainvm$\leftrightarrow$ GM4 or GM5 where there were less than 6 CCAL clusters, at least one exclusive η was present, at least one invariant mass pair >2.0 GeV.
- piinvm$\leftrightarrow$ GM4 or GM5 where there were less than 6 CCAL clusters, at least one exclusive π^0 was present, at least one invariant mass pair was >2.0 GeV.

- cmainvm$\leftrightarrow$ GM4 or GM5 where there were less than 5 CCAL clusters, the largest energy cluster could have been split (*ie.* $M_{cl} \geq 100$ MeV), and at least one invariant mass pair was >2.0 GeV.
- cmbinvm$\leftrightarrow$ GM4 or GM5 where there were less than 5 CCAL clusters, the second largest energy cluster could have been split, and at least one invariant mass pair was >2.0 GeV.
- invmass$\leftrightarrow$ GM4 or GM5 where at least one invariant mass pair was >2.0 GeV.
- etaetot$\leftrightarrow$ GM4 or GM5 where there were less than 6 CCAL clusters, at least one exclusive η was present, all invariant mass pairs were <2.0 GeV, and 90% of the total energy was in the CCAL.
- pietot$\leftrightarrow$ GM4 or GM5 where there were less than 6 CCAL clusters, at least one exclusive π^0 was present, all invariant mass pairs were <2.0 GeV, and 90% of the total energy was in the CCAL.
- cmaetot$\leftrightarrow$ GM4 or GM5 where there were less than 5 CCAL clusters, the largest energy cluster could have been split, all invariant mass pairs were <2.0 GeV, and 90% of the total energy was in the CCAL.
- cmbetot$\leftrightarrow$ GM4 or GM5 events where there were less than 5 CCAL clusters, the second largest energy cluster could have been split, all invariant mass pairs were <2.0 GeV, and 90% of the total energy was in the CCAL.
- etotten$\leftrightarrow$ GM4 or GM5 events with greater than 9 clusters, all invariant masses were less than 2.0 GeV, and 90% of the total energy was in the CCAL.
- etotsoft$\leftrightarrow$ GM4 or GM5 events where there were less than 10 CCAL clusters, all invariant mass pairs were <2.0 GeV, and 90% of the total energy was in the CCAL.

Priority	PRUDE ID	Trigger Name	Written to
1	90	GM9: Laser Monitor	GK
2	120	GM12: Minimum Bias	GK
3	130	GM13: Random Gate	GK
4	70	GM7: ETOT-NOVETO	GK
5	80	GM8: ETOT-LO	GK
6	10	GM1: e^+e^-	GK
7	40	GM4: Neutral PBG1	GK
8	30	GM3: $\phi\phi$	GP
9	20	GM2: $\bar{p}p$ 90°	GP
10	60	GM6: $\bar{p}p$ 55°	GP
11	50	GM5: Neutral ETOT	GK
12	13	goldee	GK Gold
13	11	elec	GK
14	31	$\phi\phi$	GP
15	48	goldgg	GK GNA Gold
16	42	etainvm	GK GNA
17	43	piinvm	GK GNA
18	44	cmainvm	GK GNA
19	45	cmbinvm	GK GNA
20	41	invmass	GK
21	52	etaetot	GN GNA
22	53	pietot	GN GNA
23	54	cmaetot	GN GNA
24	55	cmbetot	GN GNA
25	59	etotten	GN GNA
26	51	etotsoft	GN

Table 3.9: PRUDE IDs, priorities, names, and destinations.

Chapter 4

Data Analysis

A large statistical sample from the interaction, $p\bar{p} \rightarrow \pi^0\pi^0 \ \rightarrow 4\gamma$, collected by E835, was used to search for charmonium in the triplet P-wave region (3340-3558 MeV). The kinematic properties of data, collected from the neutral data stream (GN), were studied in order to select events that closely resembled a two-body $\pi^0\pi^0$ decay.

$$\begin{array}{lll} & & \ulcorner\!\longrightarrow \gamma\gamma \\ \overline{p}p & \longrightarrow & \pi_1^0\pi_2^0 \\ & & \quad \llcorner\!\longrightarrow \gamma\gamma \end{array}$$

Once the $\pi^0\pi^0$ candidates were selected, the remaining background events were removed. Finally, the detection efficiency was calculated by using the CCAL Shower Monte Carlo and the differential cross sections for all energy points were determined.

4.1 Event Selection

Three procedures were used to select $\pi^0\pi^0$ candidate events. Data analysis began with the selection of events from the 4 cluster CCAL NDSTs. Next, correct cluster pair combinations were selected by choosing the combinations that most

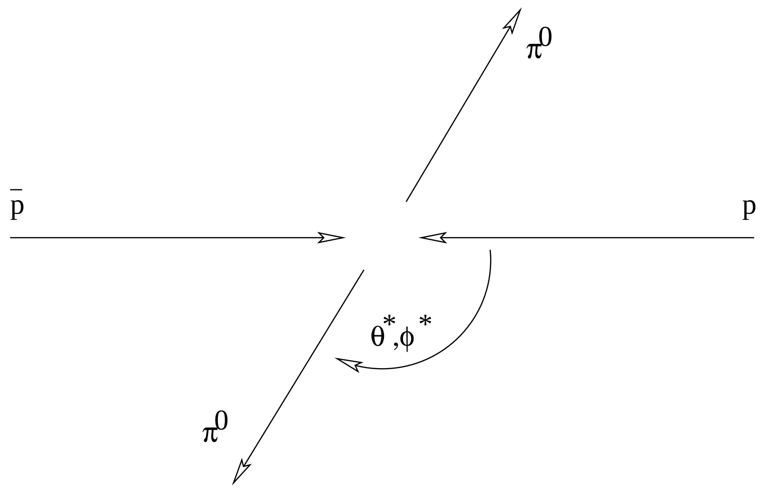

Figure 4.1: Diagram of the $\bar{p}p \to \pi^0\pi^0$ interaction. Where θ^* and ϕ^* are the $\pi^0\pi^0$ production angles.

closely conformed to a general two-body decay hypothesis, *ie.* the cluster pair combinations that most closely resembled any two particles decaying into 4 photons. Finally, analysis cuts were performed in order to select events that closely conformed to the kinematics of a di-neutral pion final state that decayed into 4 photons.

4.1.1 Neutral DST's

Neutral events from the GN data stream (Gatemaster 4 or 5) were used to study the $\bar{p}p \to \pi^0\pi^0$ interaction. A manageable subset of the GN events was created by subjecting each event to a selection process to determine whether or not the event conserved energy and momentum. The neutral events were also filtered and written, in summarized form, to tapes depending upon the number of in-time or undetermined clusters contained in either the CCAL or the CCAL+FCAL. These tapes, the Neutral Data Summary Tapes (NDSTs) and their production is described in Appendix B. To search for $\pi^0\pi^0$ events, the 4 cluster CCAL NDSTs were used[1].

Nearly 98.8% of the time, π^0s decay into two photons ($\pi^0 \rightarrow \gamma\gamma$). Therefore, sampling the 4 cluster events allowed at most 97.6% of the $\pi^0\pi^0$ events to be studied. There were four classes of these 4 photon final state $\pi^0\pi^0$ events not studied. The four samples were:

- Events lost due to the lack of complete angular coverage of the CCAL.
- Events where one or more of the photons struck the detector, but failed to deposit the required energy in the CCAL.
- Events with one or more spurious energy deposit in the calorimeter, over threshold, that were labeled in-time or undetermined.
- Events where a charged track turned the Neutral Veto on.

The inability to study all of the 4 photon events was taken into consideration and corrected for by the use of the CCAL Shower Monte Carlo (see Analysis Efficiency in Section 4.3.1).

4.1.2 Topological Selection

Since the final state particles were identical, the identification of the exact event topology was non-trivial. The selected decay criteria of the π^0 required the pairing of clusters to form π^0 candidates. In order to determine event characteristics, the position of one of the candidate π^0s was used to predict the position of the other candidate π^0. The difference between the measured and the expected positions were used to determine how well the event satisfied a two-body hypothesis. The position differences in the polar and azimuthal directions were called "akinematics" and "acoplanarity", respectively. The akinematics, $\Delta\theta$, and acoplanarity, $\Delta\phi$, were given by:

$$\Delta\theta = \theta_{2,meas} - \theta_{2,pred}(\theta_1) \tag{4.1}$$

$$\Delta\phi = \mid \phi_1 - \phi_2 \mid - \pi \tag{4.2}$$

---

[1] The CCAL+FCAL events were not used because the FCAL was not included in the Neutral Trigger.

Where $\theta_{2,meas}$ is the measured polar angle of the forward[2] π^0; $\theta_{2,pred}(\theta_1)$ is the predicted polar angle of the forward π^0 as a function of θ_1; ϕ_1 is the measured azimuthal angle of the backward π^0, and ϕ_2 is the measured azimuthal angle of the forward π^0.

For two-body events the akinematics and acoplanarity distributions were peaked at zero and had widths determined by the CCAL's angular resolution. The cluster pair combinations that had the best agreement with the two-body kinematic hypothesis was chosen by minimizing $\sqrt{(2\Delta\theta)^2 + (\Delta\phi)^2}$.

4.1.3 Analysis Cuts

Additional selection criteria were applied to the data to remove events from sources other than $\pi^0\pi^0$ decays. In total there were four criteria applied. A fiducial volume cut to remove events with large uncertainties in the cluster position, cuts on the akinematics and acoplanarity forced the candidates to fit the two-body hypothesis, and an invariant mass cut applied on the two selected cluster pairs removed events that did not contain exactly 2 π^0s.

Fiducial Volume

Events where one or more clusters located in either rings 1 or 20 were discarded. When a particle struck one of the CCAL elements in rings 1 or 20, the resulting shower was not fully contained. This partial shower containment caused unreliable measurements of the particle's position and energy, necessitating the event's removal from consideration.

Akinematics and Acoplanarity

For each event, the agreement with the two-body hypothesis was examined. If the event differed significantly from the hypothesis it was rejected. The determination of the appropriate values for the selection criteria was done by plotting the akinematics and acoplanarity distributions for each beam energy setting. These

[2] The forward π^0 was defined as the candidate π^0 furthest from ring 1.

were fit to a Gaussian distribution and events which fell within 2 standard deviations of both akinematics and acoplanarity were accepted[3]. The akinematics and acoplanarity distributions with the range of accepted values for $\pi^0\pi^0$ data taken at 3415 MeV in the center of mass are shown in Figures 4.2a and 4.2b.

Invariant Mass

After the kinematic selections cut was made to determine whether or not the cluster pairs in the event resembled π^0s. A cluster pair was identified as a π^0 if the two clusters formed a single cluster that was split by the CCAL clusterization algorithm[4] or if the cluster pair's invariant mass, $M_{\gamma\gamma}$, satisfied:

$$\mid M_{\gamma\gamma} - M_{\pi^0} \mid \leq 35\ MeV/c^2 \tag{4.3}$$

Where M_{π^0}=135 MeV/c^2 is the mass of a π^0. The cluster's invariant mass distribution and the range of accepted values for the cluster pairs in 4 photon events taken at a center of mass energy of 3415 MeV is seen in Figure 4.2c.

4.2 Background Subtraction

After the event selection, there was a small class of events ($\sim 3-5\%$) which closely resembled $\pi^0\pi^0$ events but were products of other interactions. The majority of these events were from $\bar{p}p \to \pi^0\omega$ and $\bar{p}p \to \pi^0\pi^0\pi^0$ interactions [50]. The presence of this background can be seen in Figure 4.3 as a decreasing background for increasing akinematics. The peak corresponds with akinematics values for real $\pi^0\pi^0$ events.

The di-neutral pion kinematics was mimicked when either the photon produced in a ω radiative transition, from a $\pi^0\omega$ interaction, or when one of the π^0s, from a $3\pi^0$ interaction, escaped detection. Usually, the undetected particle from these two processes would not be very energetic, since otherwise, it would have failed the kinematic conditions. Also, photons and π^0s from these interactions would

[3]The standard deviation for akinematics (acoplanarity) was 6 mrad (15 mrad).

[4]Split clusters and the CCAL clusterization algorithm have been explained in detail in Section 2.4.4.

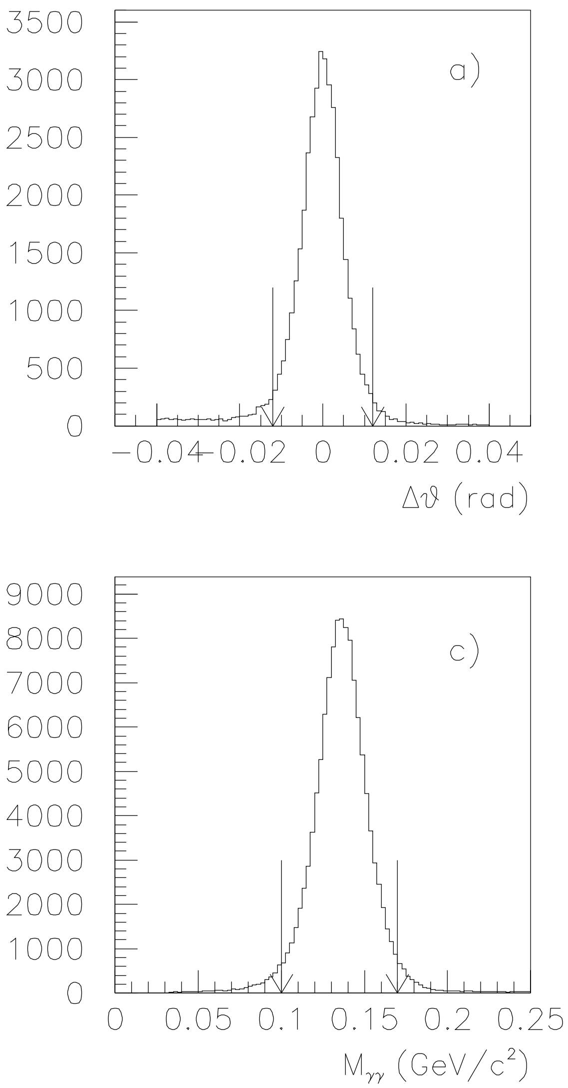

Figure 4.2: Akinematics, acoplanarity, and cluster pair invariant mass distributions for $\pi^0\pi^0$ candidate events. The arrows show the cuts made in the analysis. For each distribution, the other two analysis cuts are applied, *ie.* the selection criteria in Figures b and c are applied in Figure a. Note: Distribution c) has 2 entries per event. Candidate events were contained within all three cut windows.

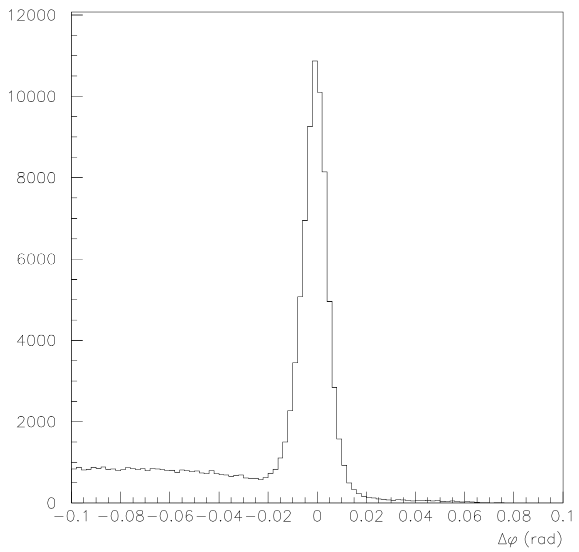

Figure 4.3: Uncut akinematics distribution for $\pi^0\pi^0$ candidate events. The background decreases as the akinematics increases.

have little effect on the four detected particle's positions when they had little transverse momentum, *ie.* traveled parallel to the beam pipe.

The asymmetric nature of the background events occurs because the polar coverage of the CCAL is not uniform. The higher background with negative akinematics values is associated with background events where a particle passed through the upstream end of the CCAL and was not detected. The missing energy from this undetected particle made the measured value of the forward π^0's polar angle appear boosted, in the antiproton direction ($\hat{z}$), with respect to the expected two-body behavior. Consequently, the akinematics was negative.

To remove the background events under the akinematics peak the data was first separated into forty $|\cos\theta^*|$ bins. The akinematics of each angular bin was then fit to a Gaussian distribution ($\pi^0\pi^0$ signal) superimposed on a 2^{nd} order polynomial, which corresponds to the background. The signal and background functions were integrated within the akinematics cut window, $2\sigma_{akin} \sim 12$ mrad, to determine the magnitude of the background, see Figure 4.4. The number of

$\pi^0\pi^0$ events was determined from:

$$N_{i,\pi^0\pi^0} = N_{i,tot} \times \frac{I_{i,G}}{I_{i,G} + I_{i,P2}} \tag{4.4}$$

Where $N_{i,tot}$ is the total number of events, $I_{i,G}$ is the integral of the Gaussian (signal), and $I_{i,P2}$ is the integral of the Polynomial (background) in the i^{th} $|\cos\theta^*|$ bin. The number of $\pi^0\pi^0$ candidates and the background fraction for each energy point in E835 are listed in Appendix A.

4.3 Differential Cross Section Measurement

The number of $\pi^0\pi^0$ events detected in a particular $|\cos\theta^*|$ bin is related to the differential cross section by:

$$\frac{\partial\sigma(\bar{p}p \to \pi^0\pi^0)}{\partial \mid \cos\theta^* \mid} = \frac{\Delta N_{\pi^0\pi^0}}{\Delta \mid \cos\theta^* \mid \times \epsilon \times \mathcal{L}_{int} \times Br(\pi^0 \to \gamma\gamma)^2} \tag{4.5}$$

Where $\Delta N_{\pi^0\pi^0}$ is the number of $\pi^0\pi^0$ events in a $|\cos\theta^*|$ bin with size $\Delta |\cos\theta^*|$, $\mathcal{L}_{int}$ is the total integrated luminosity, ϵ is the product of the geometrical acceptance and the $\pi^0\pi^0$ analysis efficiency, and $Br(\pi^0 \to \gamma\gamma)$ is the probability that a π^0 will decay into 2 photons.

4.3.1 Efficiencies

Various inefficiencies caused real $\pi^0\pi^0$ events to go undetected. Final state photon conversions into e^+e^- pairs and the Dalitz decay of π^0 ($\pi^0 \to e^+e^-$) would set the Neutral Veto on. Overlapping event contamination would also set the Neutral Veto on or mask the event's true final state particle multiplicity. Inefficiencies were also caused by the NDST production mechanism, the Neutral Trigger logic, and the geometrical acceptance of the CCAL. The total detection efficiency for a $\pi^0\pi^0$ event was:

$$\begin{aligned} \epsilon = \alpha \times \epsilon_{\pi^0\pi^0} \times \epsilon_{NT} \times \epsilon_{NDST} \times (1 - \epsilon_{NV}P_{conv})^4 \\ \times (1 - \epsilon_{NV}P_{Dalitz})^2 \times (1 - P_{cont}) \end{aligned} \tag{4.6}$$

Where α is the geometrical acceptance, ϵ_{NT} is the combined efficiency for the Neutral Trigger, ϵ_{NDST} is the NDST efficiency, $\epsilon_{\pi^0\pi^0}$ is the $\pi^0\pi^0$ analysis efficiency,

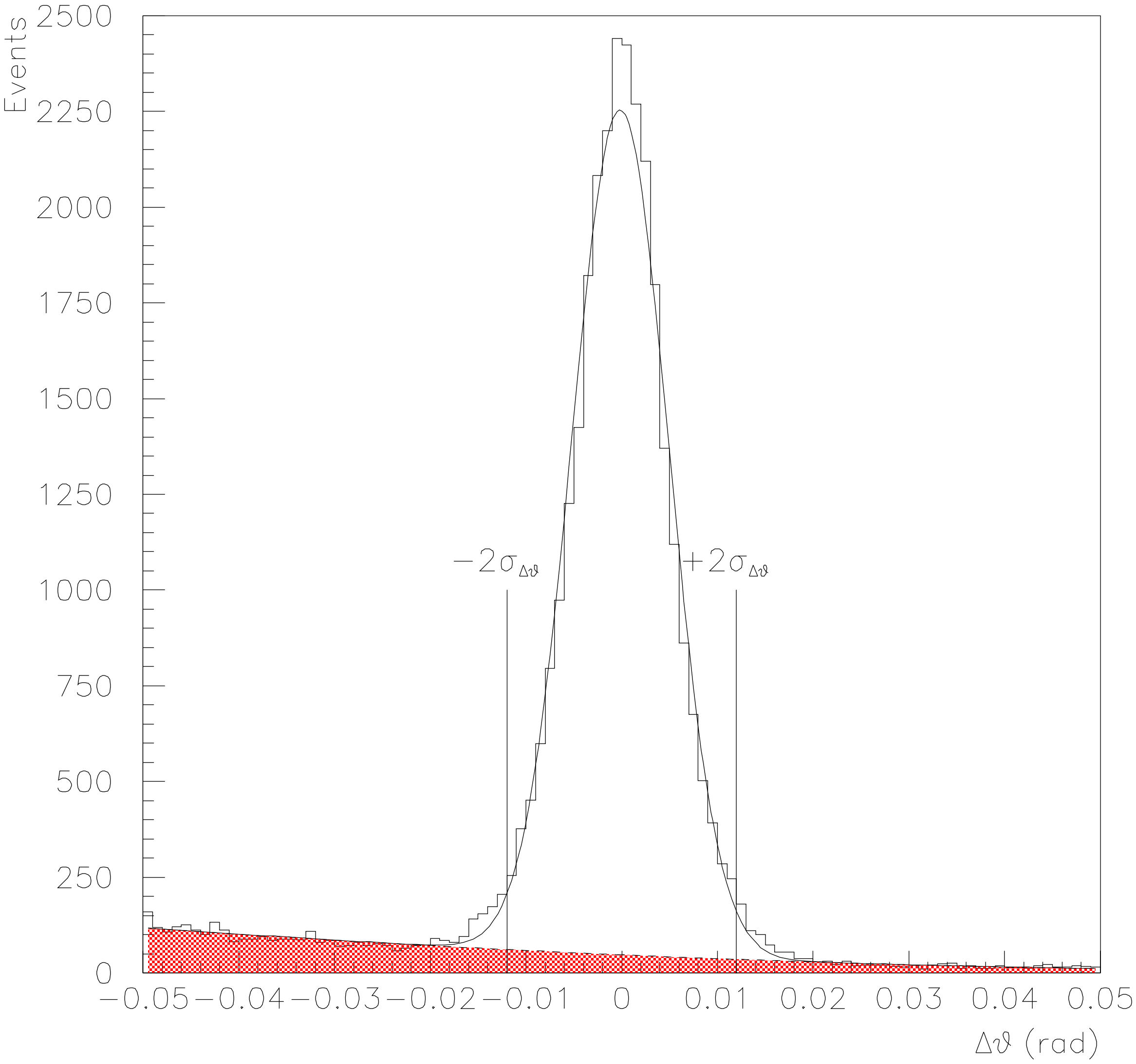

Figure 4.4: A schematic of the background subtraction method for 1 bin in $|\cos\theta^*|$. Events within the $\pm 2\sigma_{\Delta\theta}$ window are selected and the signal and background are determined by integrating the unshaded and the shaded regions respectively.

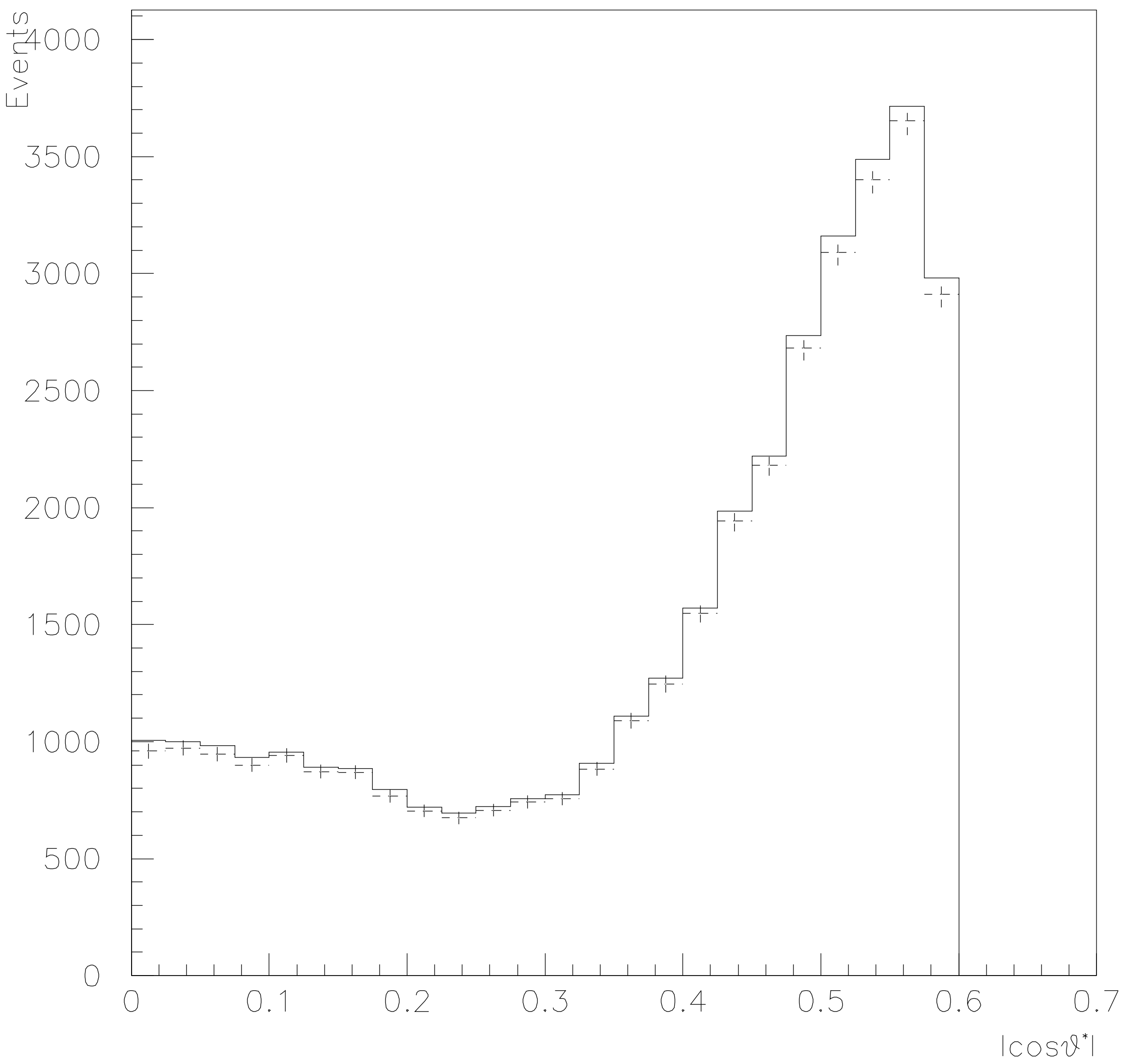

Figure 4.5: Angular distribution of the $\pi^0\pi^0$ candidate events taken at the center of mass energy, 3415 MeV. The solid histogram represents the data before background subtraction. The dashed histogram corresponds to the data after the background subtraction. The error bars on the corrected data are only statistical.

ϵ_{NV} is the Neutral Veto efficiency, P_{conv} is the photon conversion probability, P_{Dalitz} is the π^0 Dalitz decay probability, and P_{cont} is the event contamination probability.

Photon Conversions

To determine inefficiencies due to photon conversions four cluster events from the ETOT-NOVETO (see section 3.3) hardware trigger were used. From this trigger sample, 13,734 events passed the $2\pi^0$ analysis cuts (stated above) providing 54,936 photons to study.

The probability of a photon setting the Neutral Veto through conversion was then determined by using the hodoscope signals to identify charged tracks; a charged track being defined as an in-time signal greater than 0.5 mips in H1 plus an in-time signal greater than 1.0 mips in either H2 or H2′ [31]. The probability of finding a track from a $\pi^0\pi^0$ event was then:

$$P_{track} = \epsilon_{track} \times [P_{conv} + \frac{1}{2}P_{Dalitz}] \tag{4.7}$$

Where the probability that a π^0 undergoes a Dalitz decay is $P_{Dalitz} = (1.198 \pm 0.032) \times 10^{-2}$ [28] and $\epsilon_{track} = 0.794 \pm 0.013_{stat} \pm 0.02_{sys}$ is the detection efficiency for charged tracks [51]. The value of P_{track} contains both the probability associated with conversions and with Dalitz decays because the E835 detector wasn't able to distinguish between the two.

In the data there were 902 clusters with an associated charged track. Giving the probability of a photon converting into an e^+e^- pair and consequently turning on the Neutral Veto to be:

$$\epsilon_{NV} \times P_{conv} = (1.16 \pm 0.04_{stat} \pm 0.02_{sys})\%$$

Where $P_{track} = \frac{902}{54936}$ and, because the track detection efficiency is completely dominated by the Neutral Veto efficiency, $\epsilon_{NV} = \epsilon_{track}$.

Overlapping Event Contamination

If a second event occurred too close in time to a $\pi^0\pi^0$ event, information from the additional event was recorded along with the main event. The $\pi^0\pi^0$ event was rejected if the overlapping event had one or more in-time or undetermined energy deposits in the CCAL, or if the event contained a charged track. The degree of this contamination was studied by overlaying random gate data (see section 3.4) onto $\pi^0\pi^0$ events generated by the CCAL Shower Monte Carlo. Figure 4.6 shows the fraction of random gate events containing one or more in-time or undetermined cluster as a function of instantaneous luminosity.

Trigger Efficiency

The Neutral Trigger efficiency for the individual branches ETOT and PBG1 are each 100%. However, the total Neutral Trigger efficiency is calculated by combining the probability that a neutral event passes either branch of the Neutral Trigger with the probability that an event would be left unanalyzed and removed from the neutral data stream for performing trigger studies (autopassed):

$$\begin{aligned}\epsilon_{NT} = \epsilon_{auto}^2 [&\epsilon_{auto} \times \epsilon_{Neutral\ ETOT} \times (1 - \epsilon_{auto} \times \epsilon_{Neutral\ PBG1}) \\ &+\epsilon_{auto} \times \epsilon_{Neutral\ PBG1} \times (1 - \epsilon_{auto} \times \epsilon_{Neutral\ ETOT}) \\ &+\epsilon_{auto}^2 \times \epsilon_{Neutral\ ETOT} \times \epsilon_{Neutral\ PBG1}]\end{aligned}$$

This becomes:

$$\epsilon_{NT} = \epsilon_{auto}^3 [\epsilon_{Neutral\ PBG1} + \epsilon_{Neutral\ ETOT} \times (1 - \epsilon_{auto} \times \epsilon_{Neutral\ PBG1})] \tag{4.8}$$

Where, due to trigger priority (see Section 3.5), each ϵ_{auto} represents a 1% probability that the event was autopassed and $\epsilon_{Neutral\ ETOT}$ ($\epsilon_{Neutral\ PBG1}$) is the efficiency of the Neutral ETOT (PBG1) branch of the Neutral Trigger. The terms of equation 4.8 represent the probability of an event passing only the Gatemaster 4 (first), Gatemaster 5 (second), or both the Gatemaster 4 and 5 (third) trigger requirements. The third class of events, those that passed both NT branches, comprised 98.6% of the candidate $\pi^0\pi^0$ events. The total Neutral Trigger efficiency for the $\pi^0\pi^0$ analysis was $\sim 97\%$.

The Neutral ETOT and PBG1 branch efficiencies were calculated by studying 4 cluster events which passed the $\pi^0\pi^0$ selection [52]. Events satisfying the ETOT-LO hardware trigger (see Section 3.3) were used to generate Neutral ETOT(PBG1) software triggers. The Neutral ETOT(PBG1) hardware trigger efficiency was given by the ratio of events with both a Neutral ETOT(PBG1)

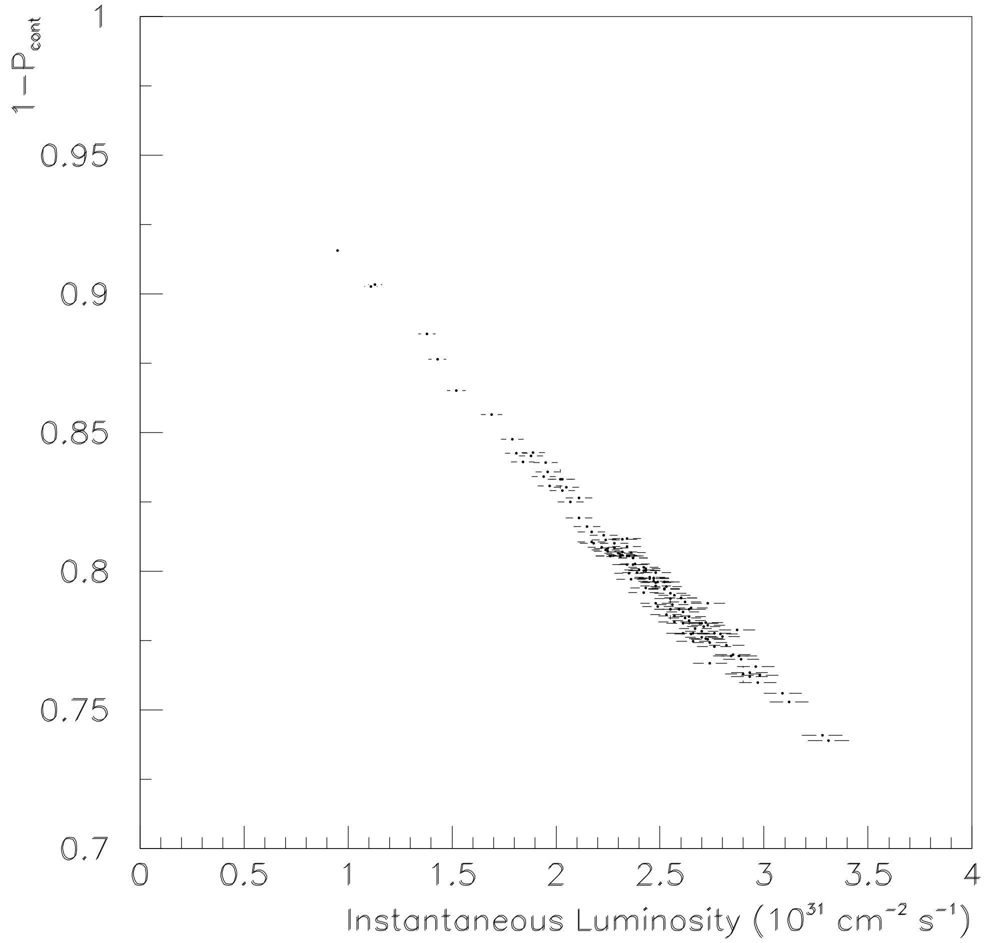

Figure 4.6: The efficiency of the random gate data in the χ_{c0} region for events with one or more i.o.u. CCAL clusters and the Neutral Veto on versus the instantaneous luminosity. The horizontal error bars represent the 2.5% uncertainty in the instantaneous luminosity measurement and the vertical error bars are statistical.

hardware and software trigger to those events with only a Neutral ETOT(PBG1) software trigger.

- Neutral ETOT software triggers were generated by comparing the total energy deposited in the CCAL with the available energy. If an event had 80% of the available energy a Neutral ETOT software trigger was generated.A 100% efficiency for the ETOT-LO trigger was measured similarly by using a relaxed trigger[5] to generate ETOT-LO software triggers.

- Neutral PBG1 software triggers were generated by studying the super-block energies in opposing super-wedges. If the energy for a super-block was larger than the threshold for it's super-ring and the opposing super-wedge had a similar super-block, a Neutral PBG1 software trigger was generated.

NDST Efficiency

The NDST efficiency, ϵ_{NDST}, accounted for data lost due to the conservation of energy and momentum cuts as well as the filtering in the NDST production. Real $\pi^0\pi^0$ events were removed by the NDST production mechanism if the event had a spurious in-time or undetermined cluster in the event, if the event's longitudinal momentum was not within 15% of the expected antiproton momentum, or the event's transverse momentum was greater than 350 MeV. The NDST efficiency was:

$$\epsilon_{NDST} = 2.08 - 5.6 \times 10^{-4}\sqrt{s} + 6.8 \times 10^{-8}(\sqrt{s})^2 \tag{4.9}$$

Where $\sqrt{s}$ is the $\bar{p}p$ center of mass energy, in MeV. A comprehensive study of the NDST efficiency is detailed in Appendix B.

Analysis Efficiency

The $\pi^0\pi^0$ analysis efficiency, $\epsilon_{\pi^0\pi^0}$, was calculated to correct for $\pi^0\pi^0$ events lost due to detector defects like dead channels, initial event reconstruction like low energy clusters below clusterization thresholds, and the analysis cuts. These efficiencies were estimated with the CCAL Shower Monte Carlo and the efficiency

[5] 60% of the event energy in the CCAL.

was found from the ratio of the number of $\pi^0\pi^0$ events detected to the number of generated $\pi^0\pi^0$ events.

For each center of mass energy point, the CCAL Shower Monte Carlo was used to generate randomly distributed $\bar{p}p \to \pi^0\pi^0 \to 4\gamma$ events that conserved energy and momentum. For each generated event, where all the final state particles were within the CCAL acceptance, their energy deposition was simulated. This was then used to assign values for the ADC and TDC counter for each block in the calorimeter. To insure an accurate simulation, the shower characteristics of the Monte Carlo were tuned to match, as well as possible, the calorimeter's response to real data [53]. In the $\pi^0\pi^0$ analysis, the response simulation was a sufficiently accurate that a detailed simulation of the particle's interactions, using for example a program like GEANT [54], was not required.

Once the ADC and TDC hitmaps were calculated, the simulated events were processed with the $\pi^0\pi^0$ analysis. As with the real data, a random gate event was superimposed on the generated event in order to determine the overlapping event contamination. An iterative process was then used to simultaneously determine the analysis efficiency ($\epsilon_{\pi^0\pi^0}$), the geometrical acceptance (α), and the overlapping event contamination ($1 - P_{cont}$).

The iterative process was necessary in order to remove event migration. Monte Carlo event migration was an artifact of the geometry of the CCAL and was caused by the uncertainty of the reconstructed cluster position and energy. These uncertainties caused events to be reconstructed in $\mid \cos\theta^* \mid$ bins different from the bins the events were generated in. The iterative process successfully removed the event migration by:

1. Using the generated angles, the reconstructed MC events were weighted with an angular distribution function determined from the previous iteration. The function was flat for the first iteration.

2. For each $\mid \cos\theta^* \mid$ bin, the ratio of the number of weighted MC events to survive the $\pi^0\pi^0$ analysis to the number of weighted MC generated events was calculated to determine the product of the analysis efficiency, the geometrical acceptance, and the overlapping event contamination probability; $\alpha \times \epsilon_{\pi^0\pi^0} \times (1 - P_{cont})$.

3. Each bin of the $\pi^0\pi^0$ data (not the MC events) was divided by the integrated luminosity ($\mathcal{L}_{int}$), the bin width ($\Delta \mid \cos\theta^* \mid = 0.025$), and the total detection efficiency (ϵ), including the result of step 2. This differential cross section was then fitted to a sixth degree polynomial in order to determine the angular distribution weighting function.

4. Steps 1-3 were repeated until convergence.

Convergence was defined to occur when all bins of the measured differential cross section changed by less than 1% of the value from the previous iteration. The result of this process is shown in Figure 4.7. The average overall efficiency for the $\pi^0\pi^0$ analysis varied from $\sim 40\%$ to $\sim 65\%$ for all the center of mass energies. The values of the total detection efficiency are listed in Appendix A. Differential cross sections computed from the number of $\pi^0\pi^0$ events observed and the overall efficiency for various center of mass energies are shown in Figure 4.8.

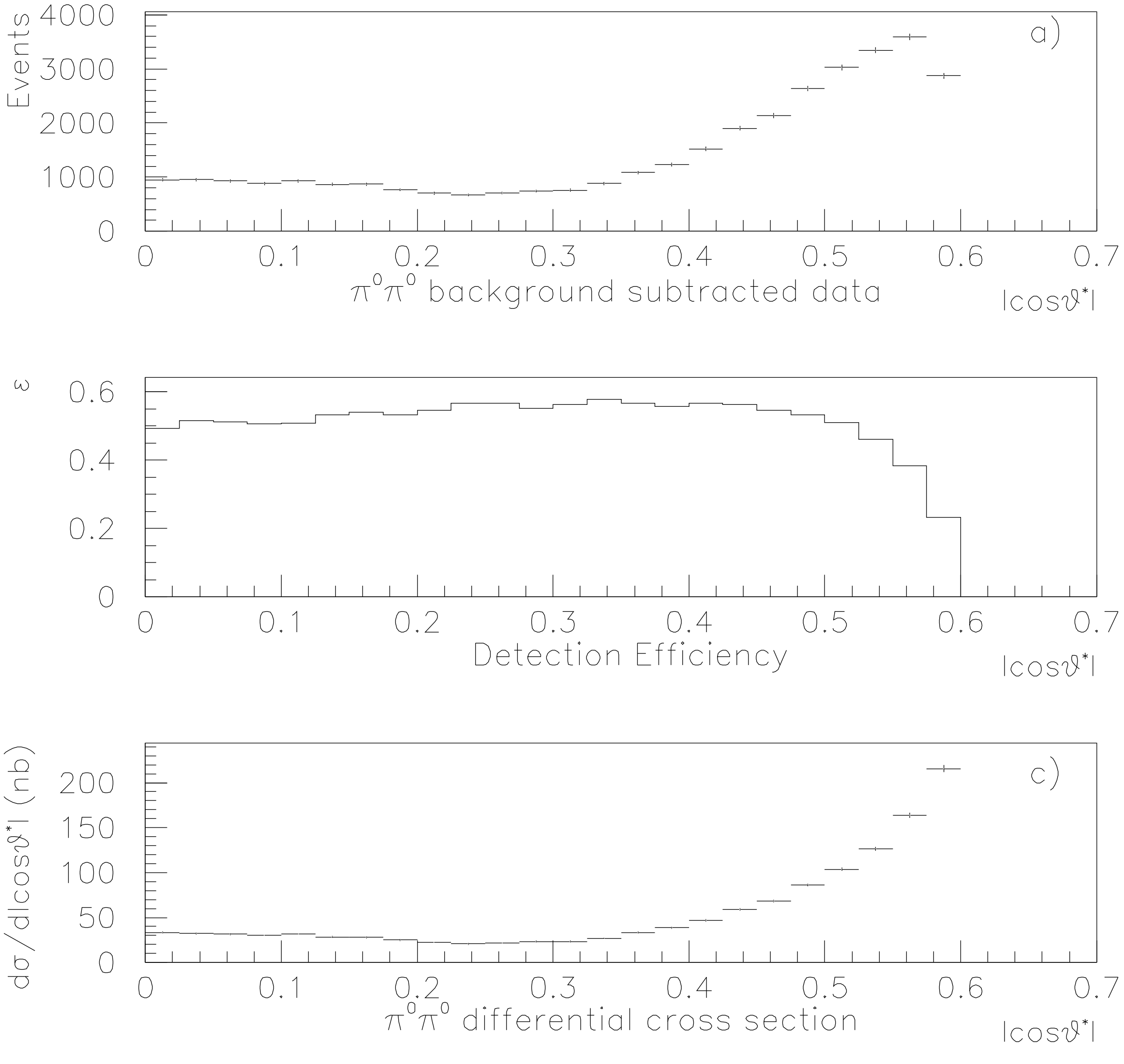

Figure 4.7: The angular distribution of a) $\pi^0\pi^0$ data events after background subtraction, b) the detection efficiency, and c) $\pi^0\pi^0$ differential cross section. The data was taken at $\sqrt{s}$ =3415 MeV.

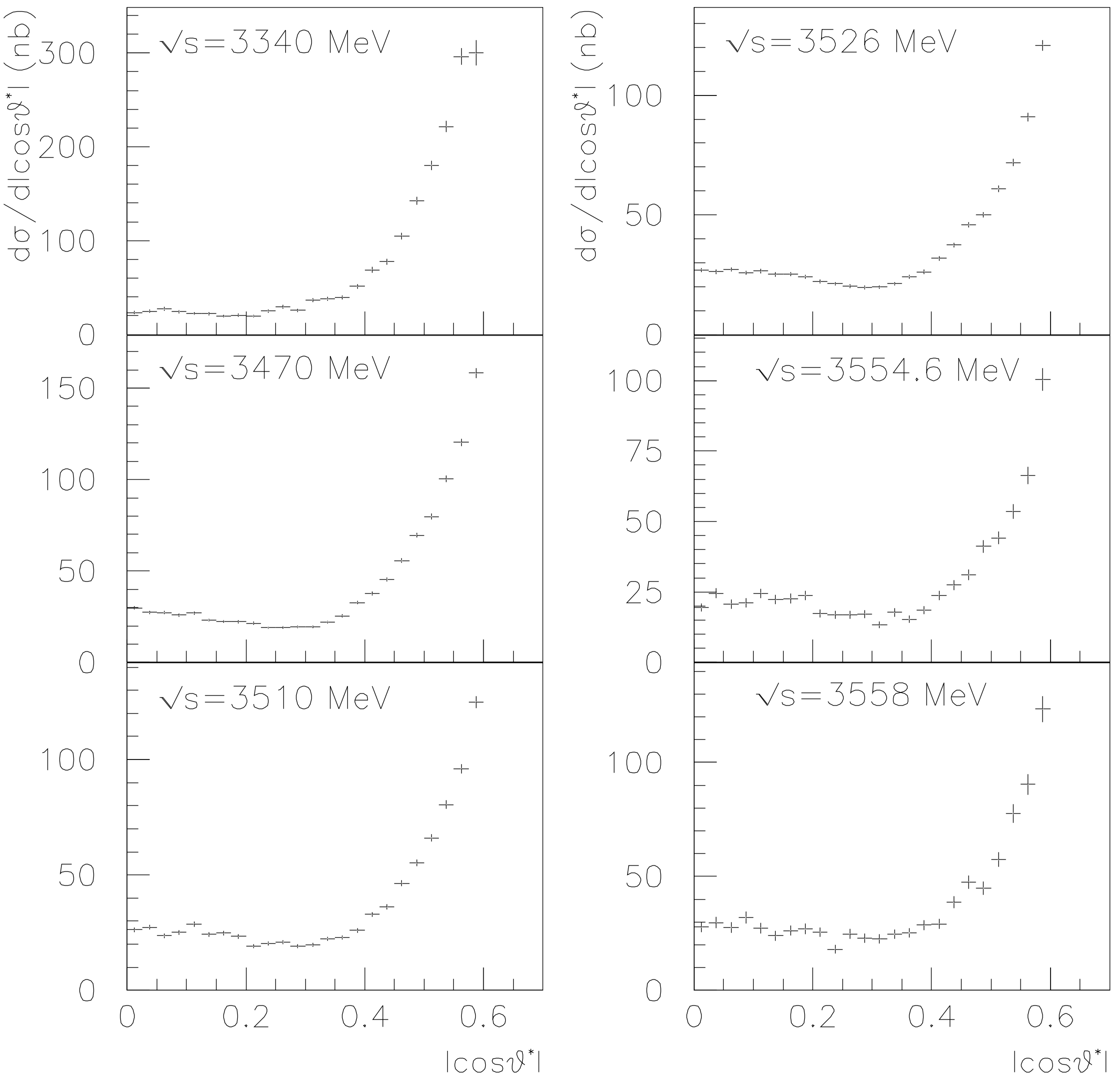

Figure 4.8: The $\pi^0\pi^0$ differential cross section for the range of $\sqrt{s}$ covering the triplet P-wave states of charmonium.

Chapter 5

Data Fitting

Figure 5.1 shows the $p\bar{p} \to \pi^0\pi^0$ energy spectrum for data taken by E835 in the triplet P-wave region of charmonium. The figure represents a total integrated luminosity of 96.6 pb^{-1}. Interesting aspects of Figure 5.1 include a steeply falling continuum which is flat in the central region and a clear enhancement near the χ_{c0} mass (~3415 MeV). An additional enhancement may also be present near the χ_{c2} (~3556 MeV) but there is insufficient continuum data near the χ_{c2} to support any contention. The breakdown of the integrated luminosity into specific resonance regions is listed in table 5.2.

This chapter describes the data fitting procedures developed in order to extract the χ_{c0} resonance contribution to the $\pi^0\pi^0$ cross section[1]. Additionally, the χ_{c0} resonance contribution is extracted and the product of the branching fractions, $Br(p\bar{p} \to \chi_{c0}) \times Br(\chi_{c0} \to \pi^0\pi^0)$ is determined. Finally, the systematic effects inherent in the data fitting and analysis are discussed.

5.1 $\pi^0\pi^0$ Differential Cross Section Calculation

In many interactions, the resonance signal is much larger than the continuum and interference between the non-resonant continuum and the resonance may

[1]The total integrated luminosity of the data taken in the χ_{c0} resonance region (3330-3480 MeV) was 32.8 pb^{-1}.

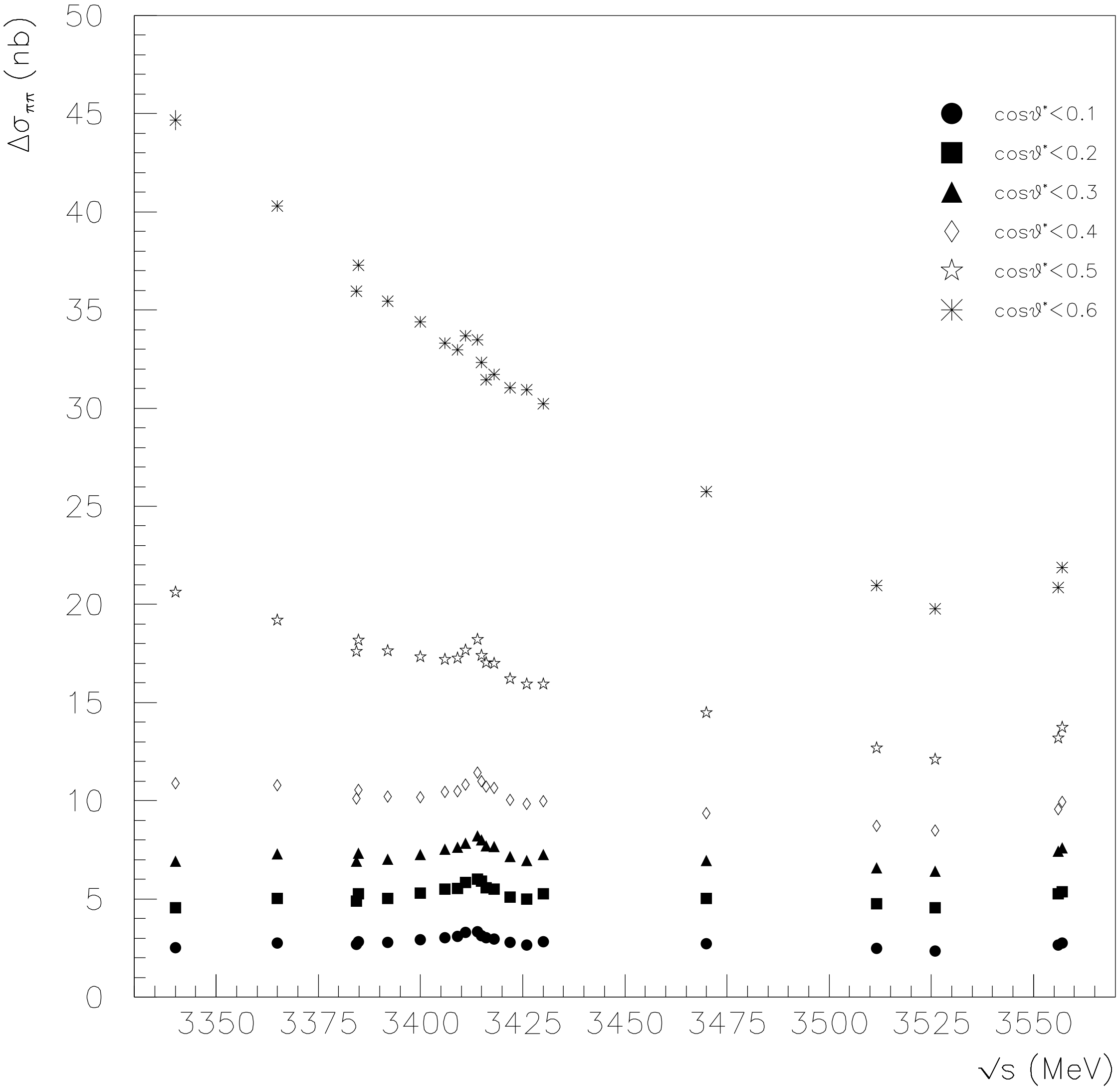

Figure 5.1: The $p\bar{p} \to \pi^0\pi^0$ energy spectrum in the P-wave region of charmonium, for increasing acceptance.

be neglected. However, in the case of $p\bar{p} \to \pi^0\pi^0$ in the χ_{c0} region, the non-resonant continuum is much larger than the expected resonance signal. Using measurements from the literature [28, 30] to estimate the total resonant cross section at the χ_{c0} , one expects ~ 0.3 nb. Reading from Figure 5.1, the total cross section is two orders of magnitude larger than the expected resonant cross section, for $\cos\theta^* < 0.6$. Additionally, it is clear that the enhancement seen at the χ_{c0} is much larger than 0.3 nb. This magnification of the resonance signal is an indication that the resonance is constructively interfering with the non-resonant continuum. Furthermore, when a simple incoherent background plus a Breit-Wigner resonance fit was performed to the $\pi^0\pi^0$ cross section, the extracted resonant amplitude was a factor of 20 larger than what was expected from previous measurements. These arguments provide evidence the continuum is not incoherent and is constructively interfering with the χ_{c0} .

In order to study constructive interference in the $p\bar{p} \to \pi^0\pi^0$ interaction, a theoretical determination of the $\pi^0\pi^0$ differential cross section was made. The calculation of the differential cross section required the study of the characteristics of the π^0, the $\pi^0\pi^0$ composite state, and the $\bar{p}p$ initial state.

The nature of the pseudo-scalar π^0 ($J^{PC} = 0^{-+}$) meson implies that the $\bar{p}p \to \pi^0\pi^0$ interaction can occur with many J^{PC}'s. Several steps are then required to determine the possible J^{PC}'s of the $\pi^0\pi^0$ state. In the first step the calculation of the eigenvalue of the C-Parity operation is made. Since C-Parity is multiplicative, the C-parity of the state is +1. The second step was the determination of the total angular momentum of the $\pi^0\pi^0$ state. This is the vector sum of the spin and orbital angular momenta, $J = L \oplus S$. The spin, S, of the $\pi^0\pi^0$ state is 0, therefore, the total angular momentum, J, is the same as the orbital angular momentum, L. To determine the orbital angular momentum, the bosonic nature of the $\pi^0\pi^0$ state was studied.

Since π^0s are bosons, their wave function is symmetric. A symmetric wave function implies that the total angular momentum must be even for a spin zero object. Thus, concluding from above, the orbital angular momentum of the $\pi^0\pi^0$ state must be even. Furthermore, from $P_{\pi^0\pi^0} = P_{\pi^0_1} P_{\pi^0_2} (-1)^L$, an even orbital angular momentum implies that the Parity of the $\pi^0\pi^0$ state is +1. Therefore the possible J^{PC}'s of the $\pi^0\pi^0$ state are $even^{++}$. Expanding the differential cross section into functions of the total angular momentum, *ie.* partial waves, the

$\mid \vec{L}_{\bar{p}p} \mid$	$\mid \vec{S}_{\bar{p}p} \mid$	$J^{PC}_{\pi^0\pi^0}$
1	1	0^{++}, 2^{++}
3	1	2^{++}, 4^{++}
5	1	4^{++}, 6^{++}
7	1	6^{++}, 8^{++}
9	1	8^{++}, 10^{++}

Table 5.1: Possible quantum numbers for the $\bar{p}p \rightarrow \pi^0\pi^0$ interaction for initial state orbital angular momentums up to L=9. Note: One initial angular momentum state will produce two final state angular momenta.

differential cross-section of the $\pi^0\pi^0$ state is:

$$\frac{\partial\sigma(\bar{p}p \rightarrow \pi^0\pi^0\ )}{\partial \mid \cos\theta^* \mid} = \left| \sum_{J=even} C_J Y_J^{m_J}(\theta^*, \phi^*) \right|^2 \tag{5.1}$$

Where C_J is complex, $\mid C_J \mid^2$ is the probability that the $\pi^0\pi^0$ state has angular momentum J with projection m_J, and where $Y_J^{m_J}(\theta^*, \phi^*)$ are the spherical harmonics and represent the angular dependence of the differential cross section.

Angular momentum conservation implies that the initial $\bar{p}p$ state must also have $J^{PC} = even^{++}$. Since protons are spin-1/2 this can only be accomplished if the orbital angular momentum of the initial state is odd and the spin of the initial state is 1 (see table 5.1). For a particle with spin angular momentum, $S_{p\bar{p}} = 1$, there are three projection of the spin on the particle's direction axis, m_s=1,0,-1. As the initial $\bar{p}p$ state decays, there is a probability that the spin orientation of the initial state, m_s, changes. If this change in the spin orientation occurs, in order to conserve the total angular momentum orientation, m_J, the orbital angular momentum orientation, m_L, must also change. Thus implying m_J is non-zero, which introduces a sum of "spin-flip" amplitudes into the differential cross section [55]. The spin-flip and non-spin-flip amplitudes are orthogonal and do not interfere, therefore, the differential cross section for $\bar{p}p \rightarrow \pi^0\pi^0$ becomes:

$$\frac{\partial\sigma(\bar{p}p \rightarrow \pi^0\pi^0\ )}{\partial \mid \cos\theta^* \mid} = \left| \sum_{J=even} C_J P_J(\cos\theta^*) \right|^2 + \left| \sum_{J=even} C_J^1 P_J^1(\cos\theta^*) \right|^2 \tag{5.2}$$

Where the second term in the differential cross section represents the spin-flip interaction and $P_J^{m_J}(\cos\theta^*)$ are Legendre Polynomials (from $Y_L^m(\theta^*, \phi^*) = P_J^{m_J}(\cos\theta^*)$

Resonance Region	Energy Range	$\mathcal{L}_{int}$ (pb^{-1})
χ_{c0}	3340-3470 MeV	32.8
χ_{c1}	3509-3512 MeV	4.3
h_c	3523-3529 MeV	50.5
χ_{c2}	3555-3558 MeV	9.0

Table 5.2: Integrated luminosity breakdown of data taken by E835 in the triplet P-wave region of charmonium.

$\times e^{\imath m_J \phi^*})^2$. The non-spin-flip (spin-flip) interaction is also known as the helicity 0 (helicity 1) component of the differential cross section[3] from the initial state helicity $\lambda_i = 0$ ($\lambda_i = 1$). A more powerful and explicit calculation of the $\bar{p}p \to \pi^0\pi^0$ differential cross section using the helicity formalism is presented in Appendix C.

5.2 Resonance Contribution Determination

The resonance contribution was extracted by using the method of least squares. The minimizing function was:

$$\chi^2 = \sum_{i=1}^{N} \sum_{j=1}^{M} \left(\frac{\nu_{i,j} - \mu_{i,j}}{\sigma_{\nu_{i,j}}} \right)^2 \tag{5.3}$$

Where $\nu_{i,j}$ is the measured differential cross section, $\sigma_{\nu_{i,j}}$ is the experimental error, and $\mu_{i,j}$ is the predicted differential cross section for center-of-mass energy point i and $\cos\theta^*$ bin j. The predicted differential cross section was determined from equation 5.2. In order to determine $\mu_{i,j}$ and ultimately extract the resonance amplitude, a parameterization of equation 5.2 was made.

[2] The spin-flip term's ϕ^* dependence is suppressed because after squaring the amplitude the ϕ^* dependence cancels exactly.

[3] Helicity is the projection of a particle's spin onto the direction of propagation, $\lambda = \frac{\vec{S}\cdot\vec{p}}{|\vec{p}|}$.

5.2.1 Method I

In general, when a differential cross section is studied with a partial wave expansion, the farther away from $\cos\theta^*$=0 one looks, the more partial waves are needed to describe the angular dependence of the cross section. Fit method I utilized the incomplete polar coverage of the CCAL in order to limit the number of partial waves used in the determination of $\mu_{i,j}$ (from Eq. 5.3). That is to say, the partial wave expansions contained within equation 5.2 were cut off at a specific angular momentum state.

This angular momentum cutoff was determined by studying the 17 measured differential cross sections independently. Each cross section was fitted to equation 5.2 (excluding the first summation) for various angular momentum cutoffs. The constant coefficients, C_J, were determined through the minimization of equation 5.3 for each center-of-mass energy point. The χ^2s for each angular momentum cutoff were compared with one another by using the F-test[4].

For every center-of-mass energy point, the result of the F-test showed decreasing significance for each additional partial wave. After the inclusion of the J=4 partial wave, the F-test suggested that the number of partial waves in the expansion was sufficient to describe the angular dependence inherent in the measured differential cross sections. Thus, the G-wave, J=4, was selected as the maximum angular momentum in the partial wave expansion for Fit Method-I.

Once the angular momentum cutoff for the predicted differential cross section was determined, the energy and angular dependence of the entire χ_{c0} data sample was studied. The simultaneous determination of the energy and angular dependence of the χ_{c0} data sample was made by parameterizing the coefficients, C_J, of equation 5.2 with real energy dependent amplitudes, A_J, and phases, δ_J:

$$C_J = A_J e^{\imath\delta_J} - \frac{A_{res}}{x+\imath}\delta_{J,0} \tag{5.4}$$

Where the first term represents the helicity 0 continuum with total angular momentum J and the second term is the relativistic form of a Briet-Wigner resonance amplitude. The center-of-mass energy parameterization of A_J and δ_J were given

[4]The F-test provides a statistical method for determining whether or not the contribution due to the addition of a free parameter is significant enough to warrant inclusion of that parameter into a fit. A detailed description of the F-test can be found in Reference [56].

as:

$$A_{J,0} + A_{J,1}x \qquad \text{and} \qquad \delta_J = \delta_{J,0} + \delta_{J,1}x \tag{5.5}$$

Due to the spinless χ_{c0} , the resonant amplitude, A_{res} is only present when $J = 0$, as denoted by $\delta_{J,0}$. Also, A_{res} is real, $x = \frac{2(E_{CM}-M_{res})}{\Gamma_{res}}$, and the χ_{c0} mass and width were taken from a previous E835 measurement [57]. Furthermore, similar to the helicity 0 continuum, the helicity 1 continuum's coefficients were parameterized by:

$$C_J^1 = A_J^1 e^{\imath\delta_J^1} \tag{5.6}$$

Equation 5.3 was minimized for the entire χ_{c0} data set which contained 17 center-of-mass energy points with 24 $\cos\theta^*$bins for each. Thus 408 total bins were fitted simultaneously. Fit method I contained a total of 19 free parameters; 1 parameter for the resonance and 4 parameters for each partial wave[5]. The total number of degrees of freedom was $24 \times 17 - 19 = 389$.

Results

The angular and energy dependence of the data sample was sufficiently determined by Fit Method-I. Figure 5.2 shows the individual helicity contributions extracted using Fit Method-I for $\sqrt{s}$ = 3415 MeV. Additionally, Figure 5.3a shows how the fraction of the differential cross section arising from the helicity 1 continuum is zero at $\cos\theta^*$=0, increasing to a maximum near 100% at $\cos\theta^*$=0.4. Also relevant is the helicity 1 continuum's contribution to the total cross section as a function of $\cos\theta^*$. Figure 5.3b shows that as the cross section is integrated, the helicity 1 continuum's contribution becomes more significant.

Although this procedure was sufficient to describe the energy and angular dependence of the data and the general structure of the continuum, it was not sensitive enough to the resonance. This insensitivity was due to the large statistics and small errors associated with the forward peaked helicity 1 continuum. The helicity 1 contribution dominated the value of the χ^2 during the minimization procedure, preventing a determination of a unique result for the resonant amplitude, A_{res}. Additionally, the large number of free parameters associated with Fit Method-I

---

[5]The helicity 1, J=2 partial wave's phase was fixed to 0, reducing the total number of free parameters to 19.

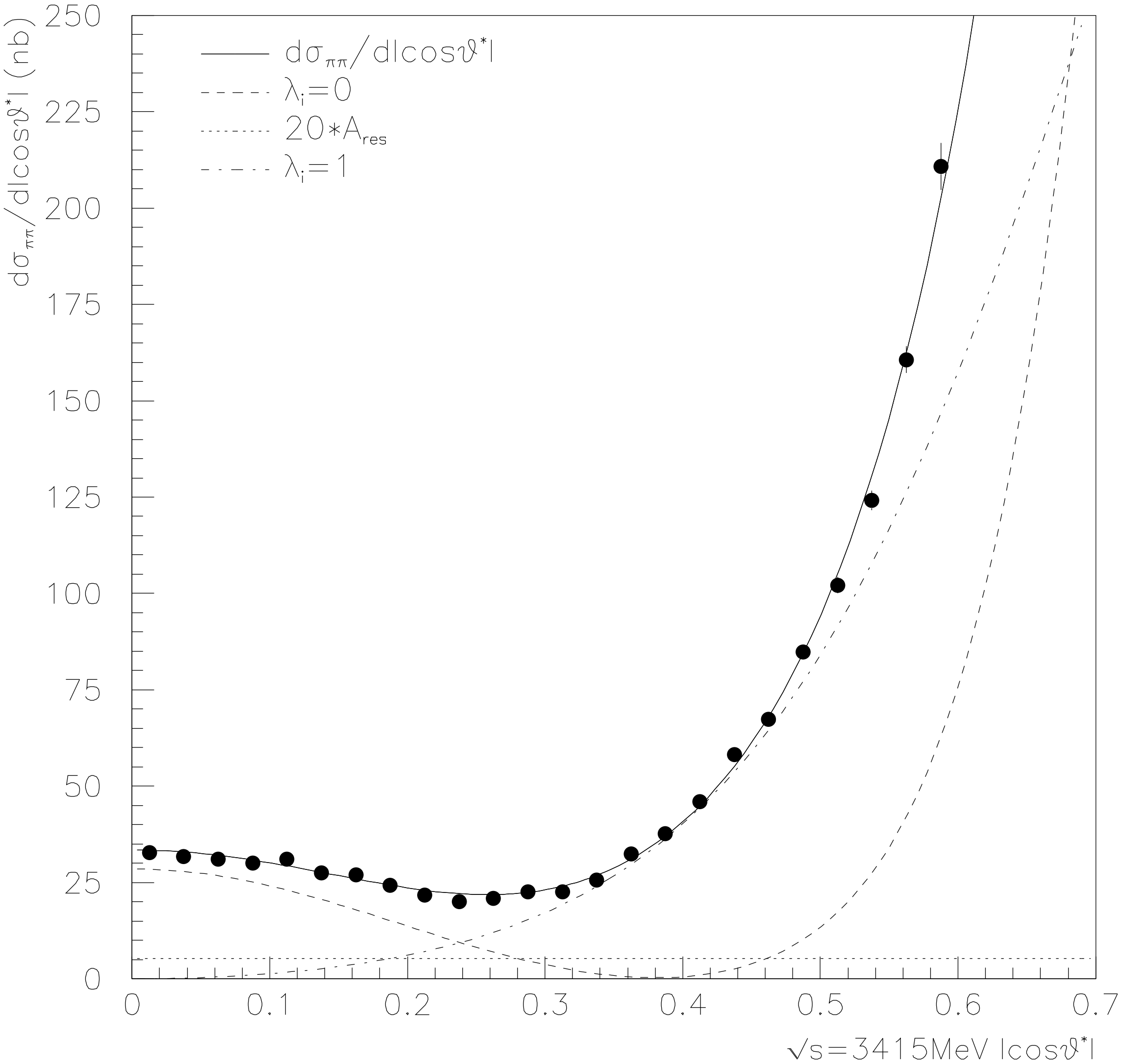

Figure 5.2: The $\pi^0\pi^0$ differential cross section and results using Fit Method-I for data taken at 3415 MeV (solid). The large dots represent the measured differential cross section with statistical error bars. The helicity 0 contribution (dashed) dominates in the central region. The helicity 1 contribution (dot-dashed) dominates in the forward region. The resonance contribution is also shown multiplied by a factor of 20 (dotted).

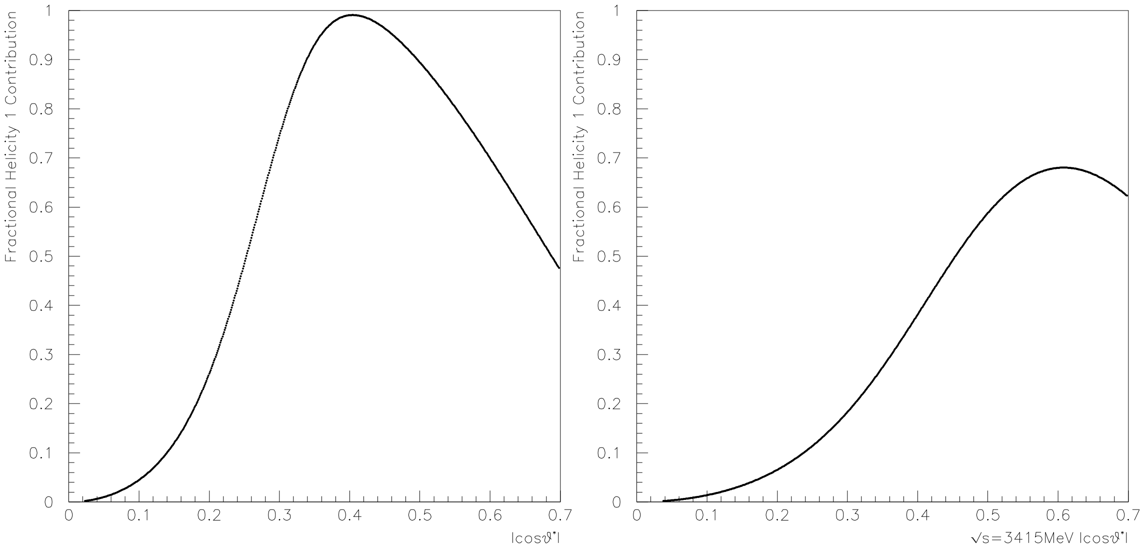

Figure 5.3: Left: The fractional contribution of the helicity 1 component to the differential cross section as a function of $\cos\theta^*$. Right: The fractional contribution of the helicity 1 component to the integrated cross section as a function of $\cos\theta^*$.

made the estimation of any possible systematic effects due to the removal of the higher angular momentum states impossible. Ultimately, for the above reasons, Fit Method-I was abandoned as a method of extracting the resonant contribution.

5.2.2 Method II

Although Fit Method-I was not sensitive enough to determine the resonant amplitude, it did give incite into how the resonant amplitude may be extracted. The principle problem with Fit Method-I was the dominance of the helicity 1 continuum over the determination of the resonant amplitude. The general helicity structure extracted using Fit Method-I shows that the helicity 1 contribution to the differential cross section can be minimized by studying the differential cross section near $\cos\theta^*=0$. Additionally, the number of free parameters associated with Fit Method-I (19) was too large for any studies of important systematic effects due to the truncation of angular momentum states in the fit.

The reduction of the number of parameters associated with the determination of the predicted differential cross section was achieved by exploiting the fact that every partial wave in equation 5.2 is an energy and angular dependent complex vector. The coherent sum of many complex vectors is also a complex vector. Thus, the parameterization of equation 5.2 for Fit Method-II is expressed as:

$$\frac{\partial\sigma(\bar{p}p \rightarrow \pi^0\pi^0\ )}{\partial \mid \cos\theta^* \mid} = \left| C_{\lambda_i=0} - \frac{A_{res}}{x+\imath} \right|^2 + |C_{\lambda_i=1}|^2 \tag{5.7}$$

Where $C_{\lambda_i=0}$ and $C_{\lambda_i=1}$ represent the complex vectors for the helicity 0 and helicity 1 continuum respectively. This can be rewritten as:

$$\frac{\partial\sigma(\bar{p}p \rightarrow \pi^0\pi^0\ )}{\partial \mid \cos\theta^* \mid} = \left| Ae^{\imath\delta} - \frac{A_{res}}{x+\imath} \right|^2 + |B(E_{CM}, \cos\theta^*)|^2 \tag{5.8}$$

Where A, δ, and $B(E_{CM}, \cos\theta^*)$ are real. The energy and angular dependence of the helicity 0 continuum was parameterized by expanding A in terms of the center-of-mass energy, E_{CM}, and $\cos\theta^*$, $A = A_0 + A_1x + A_2\cos^2\theta^*$. The $\cos\theta^*$ expansion performed the same function as limiting the number of angular momentum states in Fit Method-I when truncated and was studied with the F-test in the same manner as in Fit Method-I.

The ability of Fit Method-I to determine the general helicity structure of the differential cross section was taken advantage of to estimate $B(E_{CM}, \cos\theta^*)$. The large statistical sample in the forward region of the differential cross sections along with the structure of the associated Legendre polynomials provided a very precise estimate of the helicity 1 continuum over the entire acceptance region. Due to this precision determination of the helicity 1 continuum from Fit Method-I, the value of the helicity 1 contribution in Fit Method-II, $B(E_{CM}, \cos\theta^*)$, was fixed to the result of the helicity 1 continuum from Fit Method-I[6].

As has been discussed above, the result of Fit Method-I shows that the helicity 1 continuum is negligible near $\cos\theta^*$=0. However, the amount of statistics in this region is also small. Optimization of the signal to noise ratio was achieved by studying the behavior of the resonant amplitude as a function of increasing acceptance. Equation 5.3 was minimized for the differential cross section of every

[6]Fixing $B(E_{CM}, \cos\theta^*)$ to the result of the helicity 1 continuum extracted from Fit Method-I as well as the re-parameterization of 5.2 succeeded in reducing the number of free parameters from 19 in Fit Method-I to 5.

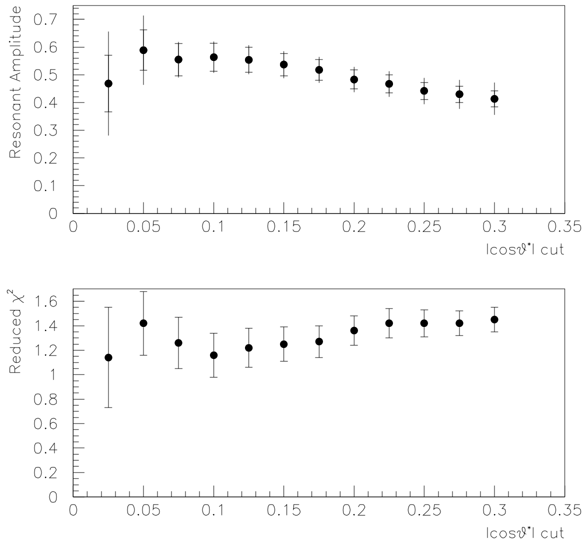

Figure 5.4: The value of the resonant amplitude (upper) and the reduced χ^2 (lower) for different $\cos\theta^*$ cuts.

center-of-mass energy point for various $\cos\theta^*$ cuts. The parameterization from equation 5.8, was used to show that the extracted resonant amplitude stayed relatively constant up to a $\cos\theta^*$ cut of 0.125 (Figure 5.4a). But, as the acceptance limit increases past $\cos\theta^*$=0.125, the value of the resonant amplitude extracted from Fit Method-II decreases. This decrease is not physical, due to the spinless nature of the χ_{c0} , and is caused by the the rapidly increasing helicity 1 continuum. In order to limit the contribution of this forward peaked incoherent continuum an acceptance cut was applied at $\cos\theta^*$=0.125.

Results

The re-parameterization of equation 5.2, the estimation of $B(E_{CM}, \cos\theta^*)$ from Fit Method-I, and the acceptance cut at $\cos\theta^*$=0.125 combined to reduce the number of free parameters from 19 in Fit Method-I to 5 and allowed fit Method II to gain the necessary sensitivity to the resonance signal. The parameter values extracted from the minimization of equation 5.3, for all center-of-mass energy points, using Fit Method-II are summarized in table 5.3; the units of the As and Bs are $\sqrt{nb}$ and the units for the δs are radians. The energy and angular behavior

Parameter:	Value:
Helicity 0	
A_{res}	0.55 ± 0.04
A_0	5.39 ± 0.03
A'	0.01 ± 0.003
A''	-41.57 ± 3.04
δ	10.20 ± 0.08
Helicity 1	
B_2	-9.77 ± 0.47
B_2'	0.13 ± 0.02
B_4	-2.79 ± 0.44
B_4'	0.04 ± 0.02
δ_4	-0.31 ± 0.13
χ^2/NDF	$97.46/80$

Table 5.3: Results of fit method 2. Where from equation 5.8: $A = A_0 + A'x + A'' \cos^2\theta^*$ and $B = (B_2 + B_2'x)P_2^1(\cos\theta^*) + (B_4 + B_4'x)e^{\imath\delta_4}P_4^1(\cos\theta^*)$.

extracted with the use of Fit Method-II are shown in Figures 5.5, 5.6, and 5.7.

The extracted resonant amplitude associated with the χ_{c0} was $A_{res} = 0.55 \pm 0.04$. The relationship between this amplitude and the product of the incoming and outgoing branching fractions is:

$$Br(\bar{p}p \to \chi_{c0}) \times Br(\chi_{c0} \to \pi^0\pi^0) = \frac{k^2}{\pi} |A_{res}|^2 \tag{5.9}$$

For $k = (M^2_{\chi_{c0}} - 4M_p^2)/4h^2$, where M_p is the mass of the proton. Thus:

$$Br(\bar{p}p \to \chi_{c0}) \times Br(\chi_{c0} \to \pi^0\pi^0) = (5.09 \pm 0.81_{stat}) \times 10^{-7} \tag{5.10}$$

5.3 Systematic Error

Table 5.4 lists the sources of systematic error in the $\pi^0\pi^0$ analysis. These eleven sources of systematic error are defined to have been introduced during two specific processes, data analysis and data fitting. Processes arising from data analysis were defined to have been introduced during the collection of data (eg. luminosity) or during data reduction (eg. seed, cluster thresholds). Systematic errors

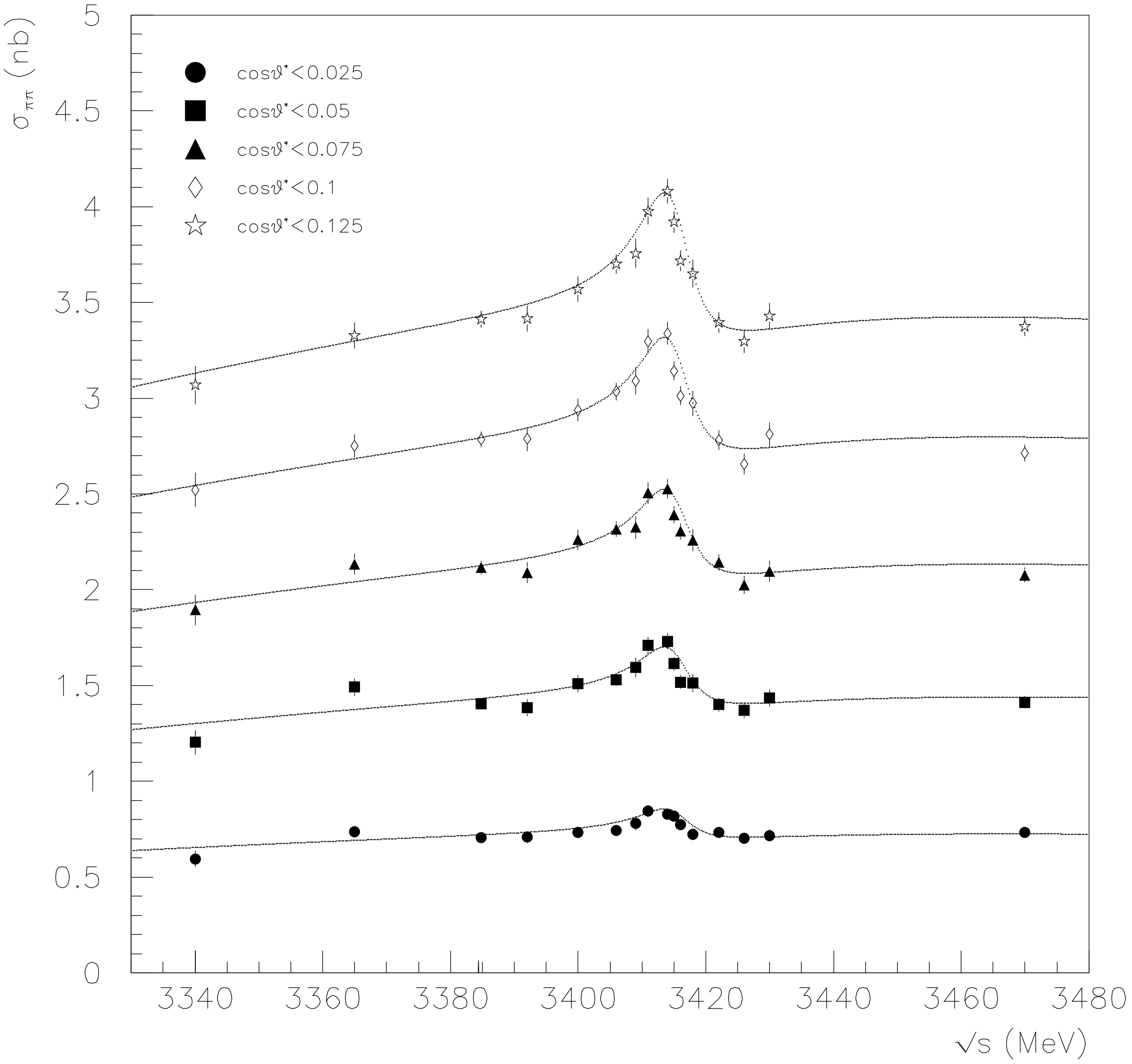

Figure 5.5: The integrated cross sections versus energy for the data using Fit Method-II for different upper limits of $\cos\theta^*$.

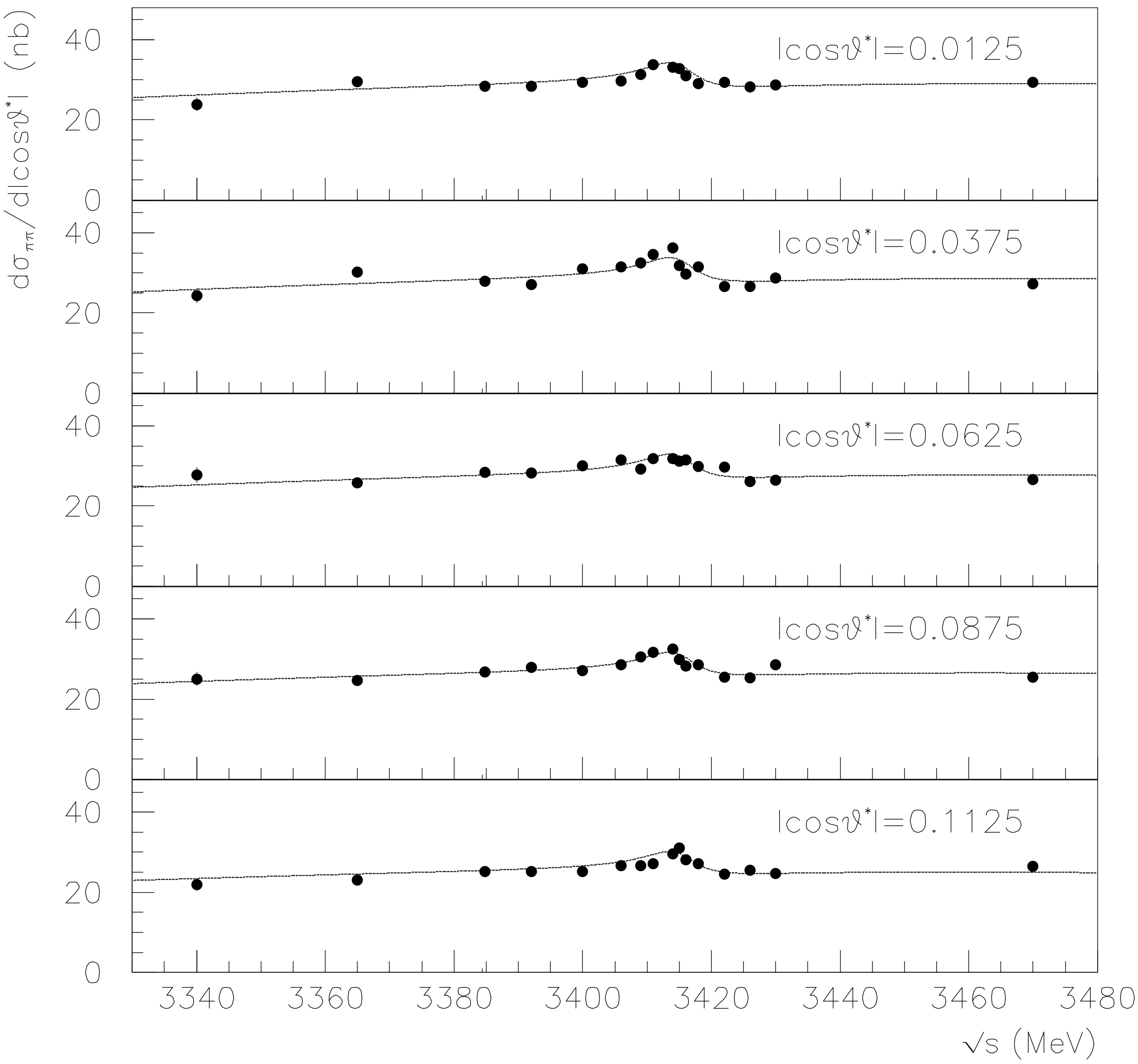

Figure 5.6: The differential cross sections versus energy for the data using Fit Method-II for different $\cos\theta^*$ bins.

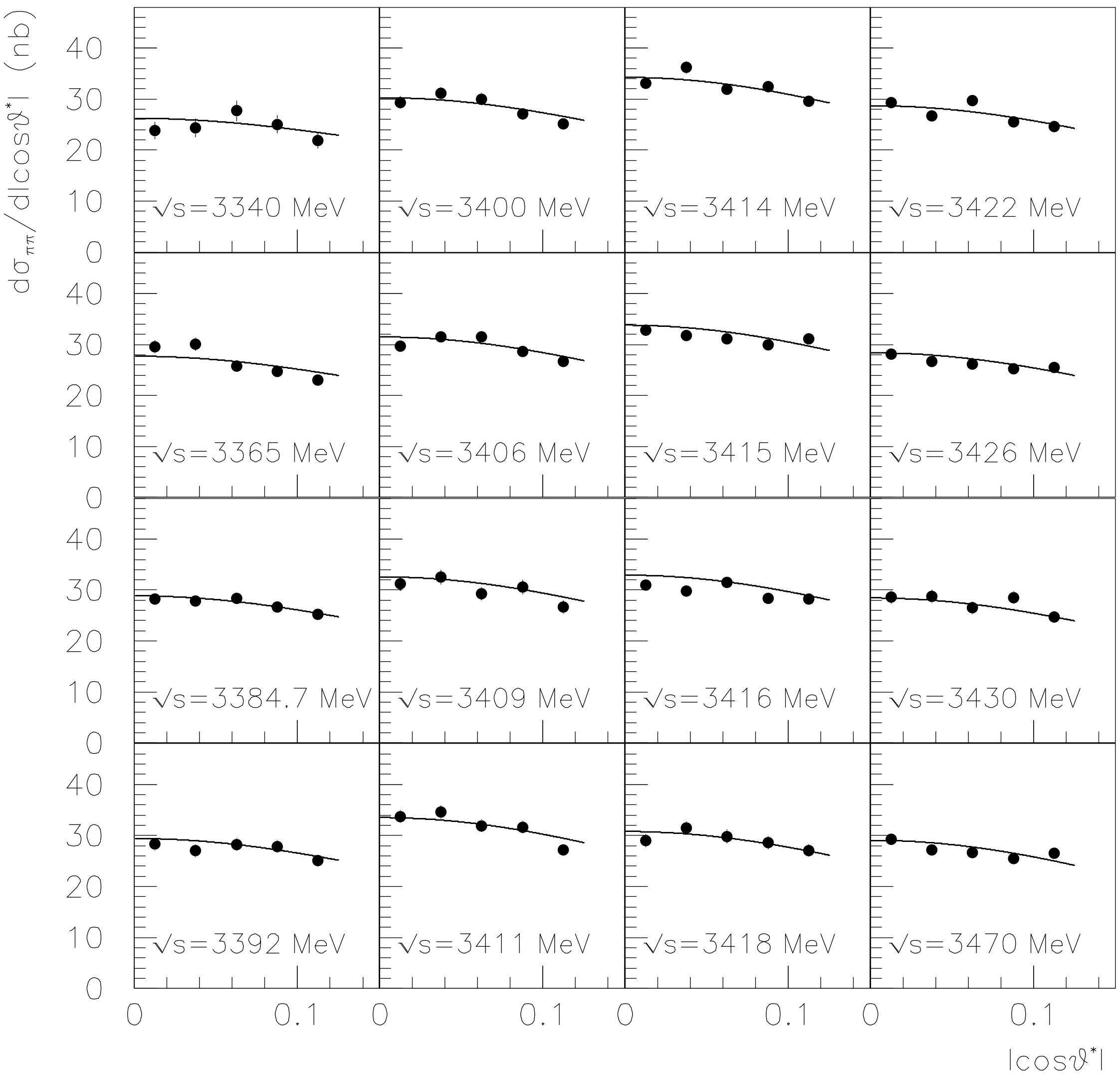

Figure 5.7: The differential cross sections versus $\cos\theta^*$ for the data using Fit Method-II, for every energy point in the χ_{c0} region.

were introduced during the data fitting procedure due to the truncation of ordered parameter expansions, *ie.* x, $\cos\theta^*$, the uncertainties in the measurements of the χ_{c0} mass and width, and the uncertainty in the estimation of the helicity 1 contribution.

The largest source of systematic error introduced during the data analysis process was due to the determination of the integrated luminosity [58]. Due to uncertainty in the measurement of the position of the interaction vertex as it relates to the luminosity monitor's viewing window and the finite measurement precision of the size of the viewing window along with the error associated with the measurement of the elastic $p\bar{p}$ scattering cross section, the integrated luminosity measurement has a systematic uncertainty of 2.5%. The remaining sources of systematic error introduced during data analysis were all due to specific selection criteria being placed on the data. These "threshold" systematics were determined by varying each analysis cut by $\pm 10\%$. The differential cross section was then recalculated and the ratio between the "adjusted" differential cross section and the "original" differential cross section was determined. The values of these two ratios, for each threshold, were averaged and taken as the systematic error associated with the threshold in question.

The sources of systematic error introduced during the data fitting process were determined using several different procedures. To determine the sensitivity of the fit to the finite angular and center-of-mass energy expansions, the next order in each expansion was included in the fit. The largest systematic error in the fitting procedure resulted from including $\mathcal{O}(\mathrm{E}^3_{\mathrm{CM}})$, 2.8%. The systematic error due to uncertainty in the measurements of the χ_{c0} mass and width[7] were considered by varying the mass and width independently by $\pm 1\sigma$, subsequently re-fitting the data, extracting the value of the resonance contribution, and comparing that result to the original result.

The final source of systematic error introduced during the data fitting process was introduced due to the uncertainty in the estimate of the helicity 1 contribution. Along with the central value of the helicity 1 component, Fit Method-I produced statistical uncertainties for each parameter. In order to calculate the

[7]The mass and width were taken as $M_{\chi_{c0}} = 3415.4 \pm 0.4\ MeV$ and $\Gamma_{\chi_{c0}} = 9.8 \pm 1.0\ MeV$ [57].

Systematic Source:	Value(%):
Data Analysis:	
Luminosity	2.5
Thresholds:	
Seed	1.0
Cluster	1.0
Split-π^0	1.0
NDST	0.6
Analysis	1.0
Fitting Procedure:	
$\mathcal{O}(\mathrm{E}^3_{\mathrm{CM}})$	2.8
$\mathcal{O}(\cos^6\theta^*)$	0.4
χ_{c0} Mass	1.0
χ_{c0} Width	0.6
$\lambda_i = 1$ Comp.	0.8

Table 5.4: Systematic error sources in the $\pi^0\pi^0$ analysis.

systematic uncertainty due to the error in the estimate of the helicity 1 contribution, the helicity 1 contribution was varied by $\pm 1\sigma$, the data were re-fitted, the resonance contribution was re-determined, and the value was compared to the original result. The helicity 1 contribution and it's one standard deviation contours can be seen in Figure 5.8.

The total systematic error was calculated by adding the individual systematics listed in table 5.4 in quadrature. The product of the incoming and outgoing branching fractions becomes:

$$Br(p\bar{p} \to \chi_{c0}\ ) \times Br(\chi_{c0}\ \to \pi^0\pi^0\ ) = (5.09 \pm 0.81_{stat} \pm 0.25_{sys}) \times 10^{-7} \quad (5.11)$$

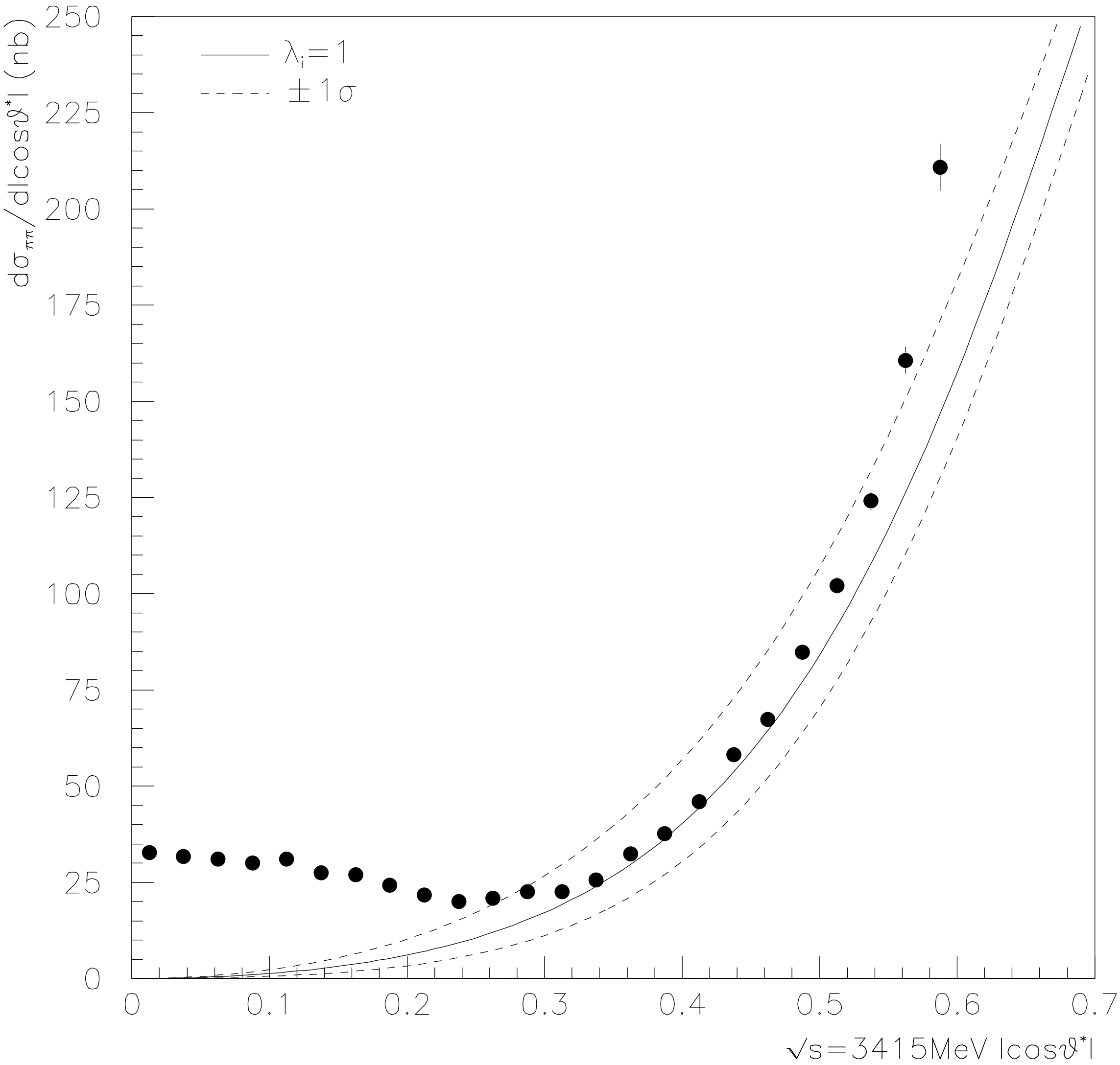

Figure 5.8: The estimate of the helicity 1 continuum extracted from Fit Method-I (solid) as a function of $\cos\theta^*$ with 1 σ errors (dashed).

Chapter 6

Summary

The $\bar{p}p \rightarrow \pi^0\pi^0$ cross section has been studied in the triplet P-wave region of charmonium. Constructive interference, between the χ_{c0} resonance and the non-resonant continuum, is responsible for the large enhancement in the $\pi^0\pi^0$ cross section near 3415 MeV. The general helicity structure of the $\pi^0\pi^0$ cross section was determined during the development of the method for extracting the χ_{c0} resonance contribution. Utilizing a parameterization of the $p\bar{p} \rightarrow \pi^0\pi^0$ differential cross section, a measurement of $Br(\bar{p}p \rightarrow \chi_{c0}) \times Br(\chi_{c0} \rightarrow \pi^0\pi^0)$ was made. Although direct measurements or theoretical predictions of this product have not previously been made, the individual branching fractions have been studied. This chapter assesses the result of this analysis in light of previous experimental and theoretical results.

6.1 Comparison With Experimental Results

Recently, C. Patrignani [59] developed a technique to remove correlations inherent in the Particle Data Group's (PDG) determination of the ψ' and χ_{cJ} branching fractions. These correlations typically arose from the use of "derived" individual branching fractions rather than the measured quantities, which tend to be composed of more than one individual branching fraction. The removal of these correlations was achieved by performing a maximum likelihood fit on all relevant measurements that included ψ' and/or χ_{cJ} branching fractions. This method has proved very reliable and it's results are listed in the PDG's 2002 Review of Particle

	W/O E835(2000)	W/ E835(2000)
$\Gamma_{\chi_{c0}}$	$15.1 \pm 2.0\ MeV$	$10.6 \pm 0.9\ MeV$
$Br(\chi_{c0} \to \gamma J/\psi)$	$(1.05 \pm 0.14)\%$	$(1.11 \pm 0.08)\%$
$Br(\chi_{c0} \to \gamma\gamma)$	$(1.96 \pm 0.36) \times 10^{-4}$	$(2.55 \pm 0.35) \times 10^{-4}$
$Br(\chi_{c0} \to p\bar{p})$	$(2.36 \pm 0.41) \times 10^{-4}$	$(2.43 \pm 0.17) \times 10^{-4}$
χ^2/NDF	$84.26/54$	$88.94/57$

Table 6.1: Results of the global fit of Reference [59] excluding and including recent E835 results.

Physics [28].

Recent measurements, made at the χ_{c0}, by E835 [57, 60] have been used to update the results of the global fit. The results of the updated global fit can be seen in table 6.1.

Although correlations in the comparison of individual branching fractions derived from composite measurements are important to take into account, it is still useful to compare derived branching fractions with previous measurements. If isospin is an exact symmetry of the strong interaction, the probability that a particle will decay to a $\pi^0\pi^0$ pair is exactly one half of the probability that the same particle will decay into $\pi^+\pi^-$. This implies that the product of the incoming and outgoing branching fractions can be constructed from results of the updated global fit and the $\chi_{c0} \to \pi^+\pi^-$ branching fraction listed in Reference [28]:

$$\begin{aligned} Br(p\bar{p} \to \chi_{c0}) \times Br(\chi_{c0} \to \pi^0\pi^0) &= \frac{1}{2} Br(p\bar{p} \to \chi_{c0}) \times Br(\chi_{c0} \to \pi^+\pi^-) \\ &= (6.1 \pm 0.4) \times 10^{-7} \end{aligned} \tag{6.1}$$

Although this composite estimate is 20% larger than the new result (Eq. 5.11) they are in agreement with one another, within errors. Additionally, the ratio of $Br(p\bar{p} \to \chi_{c0}) \times Br(\chi_{c0} \to \pi^+\pi^-)$, to the new measurement, $Br(p\bar{p} \to \chi_{c0}) \times Br(\chi_{c0} \to \pi^0\pi^0) = (5.09 \pm 0.81_{stat} \pm 0.25_{sys}) \times 10^{-3}$ gives a measure of the agreement between the experimental results and the prediction based on isospin symmetry:

$$\frac{Br(\chi_{c0} \to \pi^+\pi^-)}{Br(\chi_{c0} \to \pi^0\pi^0)} = 2.39 \pm 0.38_{stat} \pm 0.12_{sys} \pm 0.16_{PDG} \tag{6.2}$$

Parameter	Measurement ($\times 10^{-3}$)	Technique
$Br(\chi_{c0} \to \pi^0\pi^0)$	$2.09 \pm 0.35_{stat+sys}$	From Eq. 6.4
$Br(\chi_{c0} \to \pi^0\pi^0)$	$3.1 \pm 0.4 \pm 0.5$	From Ref. [29]
$Br(\chi_{c0} \to \pi^0\pi^0)$	$2.65 \pm 0.30 \pm 0.58$	From Ref. [30]
$\frac{1}{2}Br(\chi_{c0} \to \pi^+\pi^-)$	2.5 ± 0.35	From Ref. [28]

Table 6.2: Comparison of branching ratio, $\chi_{c0} \to \pi^0\pi^0$ to previous experimental results.

This ratio shows that there is a nice consistency between the previous $\pi^+\pi^-$ measurement, the new $\pi^0\pi^0$ measurement, and what would be expected from isospin. An estimate of the $p\bar{p}$ branching ratio can also be made by using the properties of isospin. Dividing equation 5.11 by $Br(\chi_{c0} \to \pi^0\pi^0) = \frac{1}{2}Br(\chi_{c0} \to \pi^+\pi^-) = (2.5 \pm 0.35) \times 10^{-3}$ implies:

$$Br(\chi_{c0} \to p\bar{p}) = (2.04 \pm 0.32_{stat} \pm 0.10_{sys} \pm 0.28_{PDG}) \times 10^{-4} \tag{6.3}$$

This value is systematically lower (19%), but still compares favorably the value determined with the updated global fit (table 6.1).

In order to obtain $Br(\chi_{c0} \to \pi^0\pi^0)$, The result, equation 5.11, was included into the updated global fit. The result of which was:

$$Br(\chi_{c0} \to \pi^0\pi^0) = (2.09 \pm 0.35_{stat+sys}) \times 10^{-3} \tag{6.4}$$

This result is smaller than but still in reasonable agreement with the results of earlier measurements [29, 30], see table 6.2.

6.2 Comparison With Theoretical Predictions

The various approximations to exact QCD have had differing degrees of success when attempting to calculate the rates of exclusive P-wave quarkonium decays. Because there are no effects of dynamic gluons incorporated within the framework of the potential model discussed in Chapter 1 it fails when attempts are made at predicting the exclusive P-wave charmonium branching fractions. Also, difficulties arise in perturbative QCD (pQCD), which is effective at calculating short distance processes due to the exploitation of the asymptotic freedom associated with QCD. This happens because infrared divergences are revealed in exclusive quarkonium decay calculations at $\mathcal{O}(\alpha_s^3)$. Additional complications arise in calculating the χ_{c0} decay into $p\bar{p}$. The spin zero χ_{c0} is forbidden to decay into $p\bar{p}$ due to a violation of the helicity conservation rule (HCR), which states that heavy meson decay proceeding through hard gluons can only decay into particle-antiparticle pair if the decay products have opposite helicities. However, through the use of QCD sum rules, Anselmino *et. al.* were able to calculate the partial width of the HCR-violating $\chi_{c0} \rightarrow p\bar{p}$ decay using several different schemes. In order to make these calculations they replaced the current mass of the quarks with a constituent mass. The results of these calculations can be seen in table 6.3. For comparison with the predictions listed in table 6.3, an experimental determination of the partial width, $\Gamma(\chi_{c0} \rightarrow p\bar{p})$, was made by scaling the result $Br(\chi_{c0} \rightarrow p\bar{p}) = (2.04 \pm 0.32_{stat} \pm 0.10_{sys} \pm 0.28_{PDG}) \times 10^{-4}$ to the total width of the χ_{c0} , from table 6.1:

$$\Gamma(\chi_{c0} \rightarrow p\bar{p}) = (216.2 \pm 35.5_{stat+sys} \pm 29.7_{PDG} \pm 18.4_{width})\ eV \tag{6.5}$$

In 1982, Chernyak and Zhitnitsky predicted the branching fractions of charmonium states decaying into $\pi^+\pi^-$ [62]. Using the properties of isospin and scaling to the total χ_{c0} width (from table 6.1), the prediction for the $\pi^0\pi^0$ partial width is:

$$\Gamma(\chi_{c0} \rightarrow \pi^0\pi^0) = (58.3 \pm 5.0_{width})\ keV \tag{6.6}$$

Calculations based upon a non-relativistic QCD (NRQCD) approximation have also been made to predict P-wave quarkonium decay rates. NRQCD was developed by Bodwin, Braaten, and Lepage [63] and is an effective field theory which reformulates QCD into separate non-relativistic and relativistic parts. This separation is achieved by introducing an ultraviolet cutoff into the QCD Lagrangian. This cutoff effectively removes the contributions from any relativistic virtual states from the quarkonium wave-function. Since these intermediate states cannot propagate over large distances, they are assumed to be local and are re-introduced into the Lagrangian by adding additional local interactions.

NRQCD has the advantage that additional local interactions can be added to the Lagrangian in order to reproduce the accuracy of QCD results. Furthermore, features of the heavy quarkonium state can be studied, *eg.* higher order

Paramter	Experimental Measurement (eV)	
$\Gamma(\chi_{c0} \rightarrow p\bar{p})$	$216.2 \pm 35.5_{stat+sys} \pm 29.7_{PDG} \pm 18.4_{width}$	
Parameter	Theoretical Prediction (eV)	Technique
$\Gamma(\chi_{c0} \rightarrow p\bar{p})$	0.46 ± 0.23	Scheme as
	45 ± 22	Scheme CZ
	26 ± 13	Scheme COZ
	10 ± 5	Scheme KS
	23 ± 11	Scheme GS

Table 6.3: Comparison of the experimental measurement with various theoretical predictions of the partial width, $\Gamma(\chi_{c0} \rightarrow p\bar{p})$ from Reference [61].

Fock states, without having to disentangle the relativistic part. To study these properties, the quarkonium state is expanded in orders of v, the heavy quark velocity with respect to the quarkonium state's center-of-mass. One such expansion is utilized to study the exclusive decays of P-wave charmonium:

$$|\chi_{cJ}\rangle = \mathcal{O}(1)\left|c\bar{c}_1(^3P_J)\right\rangle + \mathcal{O}(v)\left|c\bar{c}_8(^3S_1)g\right\rangle + \mathcal{O}(v^2) \tag{6.7}$$

where the first term is in a color singlet state, specified by $c\bar{c}_1$ and the second term is in a color octet state, $c\bar{c}_8$ and represents a virtual state where either the charm or anticharm quark has radiated a gluon and the $c\bar{c}$ pair exist in a $^3S_1$ state.

Decay widths of P-wave charmonium have been calculated by both excluding and including the color octet state [64]. When only the singlet state is considered, the calculation yielded:

$$\Gamma(\chi_{c0} \rightarrow \pi^0\pi^0) = \frac{1}{2}\Gamma(\chi_{c0} \rightarrow \pi^+\pi^-) = 4.11\ keV \tag{6.8}$$

When the color octet state was included in the expansion, the prediction was larger:

$$\Gamma(\chi_{c0} \rightarrow \pi^0\pi^0) = 23.5\ keV \tag{6.9}$$

The above predictions and can be seen in table 6.4. The experimental determination of $\Gamma(\chi_{c0} \rightarrow \pi^0\pi^0)$ is made by scaling the result, equation 6.4, to the total width given in table 6.1. The measurement is:

$$\Gamma(\chi_{c0} \rightarrow \pi^0\pi^0) = (22.2 \pm 3.7_{stat+sys} \pm 1.9_{width})\ keV \tag{6.10}$$

Parameter	Prediction (keV)	Technique
$\Gamma(\chi_{c0} \rightarrow \pi^0\pi^0)$	$53.9 \pm 5.5_{width}$	Sum Rules [62]
	4.11	Color Singlet [64]
	23.5	Color Octet [64]

Table 6.4: Theoretical predictions of the partial width, $\Gamma(\chi_{c0} \rightarrow \pi^0\pi^0)$ from QCD sum rules and NRQCD.

6.3 Conclusion

A measurement of $Br(p\bar{p} \rightarrow \chi_{c0}) \times Br(\chi_{c0} \rightarrow \pi^0\pi^0)$ has been made. This new measurement is in agreement with and was measured with a higher precision than the product calculated from the individual branching fractions, $Br(\chi_{c0} \rightarrow p\bar{p})$ and $Br(\chi_{c0} \rightarrow \pi^+\pi^-)$, listed in Reference [28]. In addition, the individual branching fractions, extracted using independent experimental results, are in agreement with previous measurements.

Comparisons of the individual partial decay widths, $\Gamma(\chi_{c0} \rightarrow p\bar{p})$ and $\Gamma(\chi_{c0} \rightarrow \pi^0\pi^0)$, with theoretical predictions have varying results. The $p\bar{p}$ partial width is at least an order of magnitude larger and completely incompatible with any of the predictions using QCD sum rules. The $\pi^0\pi^0$ partial width also disagrees with the prediction calculated with QCD sum rules. Furthermore, the NRQCD prediction disagrees if only the color singlet component of the χ_{c0} wave function is included. However, when the color octet is included in the calculation, the result is in excellent agreement with the new measurement. This agreement is consistent with previous efforts which demonstrated the need for including the color octet contribution in the NRQCD formalism for evaluating the decay of P-wave charmonium [63, 64, 65]. However, there are no predictions of $\Gamma(\chi_{c0} \rightarrow p\bar{p})$ using NRQCD. This is unfortunate because the predicted decay rates of the χ_{c1} and χ_{c2} into $p\bar{p}$ [65] are in agreement with experimental results when the color octet contribution is included. If a more thorough understanding of helicity conservation and QCD is to be achieved, the incompatibility of the experimental results with the theoretical predictions of $p\bar{p}$ decay of the χ_{c0} needs to be resolved. One hope for this resolution is by using the NRQCD formalism with the inclusion of the color octet contribution to make new predictions of exclusive charmonium decay rates.

Appendix A

$\pi^0\pi^0$ Data Summary

The following tables summarize the data taken by E835, in the χ_{c0} region of charmonium. The measured differential cross section, as well as all other relevant information, is given for each energy point used in the analysis detailed in chapter 4.

$E_{CM} = 3340\ MeV,\ \mathcal{L}_{int} = 0.629\ pb^{-1}$				
$\cos\theta^*$	N_{tot}	Bkg. Frac.	ϵ	$\frac{\partial\sigma}{\partial\lvert\cos\theta^*\rvert}$ (nb)
0.0125	188.	0.0518	0.4755	23.823 ± 1.738
0.0375	181.	0.0411	0.4534	24.326 ± 1.808
0.0625	199.	0.0030	0.4556	27.676 ± 1.962
0.0875	203.	0.0247	0.5024	25.043 ± 1.758
0.1125	189.	0.0616	0.5155	21.863 ± 1.590
0.1375	165.	0.0213	0.4845	21.180 ± 1.649
0.1625	147.	0.0198	0.4951	18.491 ± 1.525
0.1875	175.	0.0446	0.5415	19.624 ± 1.484
0.2125	169.	0.0661	0.5416	18.519 ± 1.424
0.2375	193.	0.0329	0.5045	23.514 ± 1.692
0.2625	231.	0.0170	0.5145	28.049 ± 1.846
0.2875	220.	0.0288	0.5572	24.369 ± 1.644
0.3125	302.	0.0216	0.5385	34.872 ± 2.006
0.3375	298.	0.0189	0.5177	35.894 ± 2.080
0.3625	338.	0.0143	0.5436	38.951 ± 2.118
0.3875	460.	0.0468	0.5594	49.807 ± 2.322
0.4125	564.	0.0306	0.5123	67.821 ± 2.856
0.4375	648.	0.0276	0.5169	77.467 ± 3.043
0.4625	888.	0.0227	0.5340	103.281 ± 3.466
0.4875	1092.	0.0283	0.4812	140.148 ± 4.241
0.5125	1263.	0.0301	0.4461	174.535 ± 4.911
0.5375	1412.	0.0277	0.4075	214.116 ± 5.699
0.5625	1213.	0.0237	0.2644	284.604 ± 8.172
0.5875	489.	0.0346	0.1039	288.648 ± 13.054

$E_{CM} = 3365\ MeV,\ \mathcal{L}_{int} = 1.424\ pb^{-1}$				
$\cos\theta^*$	N_{tot}	Bkg. Frac.	ϵ	$\frac{\partial\sigma}{\partial\lvert\cos\theta^*\rvert}$ (nb)
0.0125	535.	0.0201	0.4990	29.521 ± 1.276
0.0375	527.	0.0163	0.4835	30.126 ± 1.312
0.0625	475.	0.0516	0.4914	25.758 ± 1.182
0.0875	475.	0.0386	0.5202	24.666 ± 1.132
0.1125	449.	0.0355	0.5275	23.065 ± 1.089
0.1375	458.	0.0327	0.5095	24.431 ± 1.142
0.1625	425.	0.0248	0.5229	22.270 ± 1.080
0.1875	450.	0.0490	0.5575	21.567 ± 1.016
0.2125	476.	0.0314	0.5557	23.310 ± 1.068
0.2375	435.	0.0306	0.5312	22.304 ± 1.070
0.2625	428.	0.0264	0.5508	21.257 ± 1.028
0.2875	503.	0.0327	0.5756	23.752 ± 1.059
0.3125	524.	0.0295	0.5650	25.288 ± 1.105
0.3375	632.	0.0420	0.5391	31.553 ± 1.255
0.3625	759.	0.0202	0.5690	36.720 ± 1.333
0.3875	959.	0.0207	0.5750	45.892 ± 1.482
0.4125	1157.	0.0172	0.5428	58.857 ± 1.730
0.4375	1390.	0.0127	0.5461	70.605 ± 1.894
0.4625	1792.	0.0102	0.5570	89.472 ± 2.114
0.4875	2173.	0.0186	0.5123	116.967 ± 2.509
0.5125	2591.	0.0200	0.4783	149.157 ± 2.930
0.5375	2876.	0.0191	0.4381	180.908 ± 3.373
0.5625	2826.	0.0136	0.3136	249.725 ± 4.698
0.5875	1472.	0.0251	0.1522	264.928 ± 6.904

$E_{CM} = 3384.4\ MeV$, $\mathcal{L}_{int} = 1.631\ pb^{-1}$				
$\cos\theta^*$	N_{tot}	Bkg. Frac.	ϵ	$\frac{\partial\sigma}{\partial\lvert\cos\theta^*\rvert}$ (nb)
0.0125	513.	0.0458	0.4910	26.200 ± 1.157
0.0375	515.	0.0530	0.4816	26.618 ± 1.173
0.0625	549.	0.0333	0.4849	28.765 ± 1.228
0.0875	522.	0.0248	0.5040	26.547 ± 1.162
0.1125	451.	0.0305	0.5140	22.356 ± 1.053
0.1375	480.	0.0552	0.5114	23.306 ± 1.064
0.1625	440.	0.0625	0.5197	20.859 ± 0.994
0.1875	437.	0.0454	0.5378	20.385 ± 0.975
0.2125	433.	0.0478	0.5405	20.048 ± 0.963
0.2375	420.	0.0404	0.5373	19.713 ± 0.962
0.2625	443.	0.0448	0.5463	20.359 ± 0.967
0.2875	461.	0.0199	0.5562	21.350 ± 0.994
0.3125	509.	0.0310	0.5540	23.400 ± 1.037
0.3375	642.	0.0268	0.5385	30.493 ± 1.204
0.3625	735.	0.0316	0.5629	33.234 ± 1.226
0.3875	886.	0.0208	0.5560	41.010 ± 1.378
0.4125	1038.	0.0195	0.5407	49.470 ± 1.536
0.4375	1263.	0.0082	0.5427	60.658 ± 1.707
0.4625	1695.	0.0157	0.5397	81.249 ± 1.973
0.4875	2142.	0.0208	0.5078	108.540 ± 2.345
0.5125	2437.	0.0196	0.4811	130.523 ± 2.644
0.5375	2690.	0.0177	0.4432	156.682 ± 3.021
0.5625	2728.	0.0211	0.3352	209.374 ± 4.009
0.5875	1682.	0.0172	0.1833	236.960 ± 5.778

$E_{CM} = 3384.8\ MeV$, $\mathcal{L}_{int} = 3.371\ pb^{-1}$				
$\cos\theta^*$	N_{tot}	Bkg. Frac.	ϵ	$\frac{\partial\sigma}{\partial\lvert\cos\theta^*\rvert}$ (nb)
0.0125	1265.	0.0303	0.4978	29.240 ± 0.822
0.0375	1210.	0.0258	0.4914	28.466 ± 0.818
0.0625	1221.	0.0293	0.4974	28.274 ± 0.809
0.0875	1196.	0.0341	0.5112	26.817 ± 0.775
0.1125	1201.	0.0340	0.5201	26.468 ± 0.764
0.1375	1159.	0.0198	0.5181	26.018 ± 0.764
0.1625	1044.	0.0206	0.5289	22.941 ± 0.710
0.1875	1073.	0.0267	0.5460	22.696 ± 0.693
0.2125	965.	0.0329	0.5562	19.910 ± 0.641
0.2375	946.	0.0360	0.5467	19.794 ± 0.644
0.2625	991.	0.0125	0.5584	20.797 ± 0.661
0.2875	1062.	0.0214	0.5690	21.671 ± 0.665
0.3125	1230.	0.0234	0.5687	25.066 ± 0.715
0.3375	1352.	0.0230	0.5542	28.286 ± 0.769
0.3625	1657.	0.0172	0.5701	33.893 ± 0.832
0.3875	2053.	0.0164	0.5682	42.170 ± 0.931
0.4125	2428.	0.0128	0.5500	51.714 ± 1.050
0.4375	3054.	0.0173	0.5512	64.610 ± 1.169
0.4625	3875.	0.0240	0.5503	81.545 ± 1.310
0.4875	4756.	0.0178	0.5207	106.457 ± 1.544
0.5125	5566.	0.0218	0.4911	131.564 ± 1.764
0.5375	6293.	0.0203	0.4488	162.994 ± 2.055
0.5625	6277.	0.0193	0.3449	211.781 ± 2.673
0.5875	4123.	0.0187	0.1857	258.450 ± 4.025

$E_{CM} = 3392\ MeV,\ \mathcal{L}_{int} = 1.431\ pb^{-1}$				
$\cos\theta^*$	N_{tot}	Bkg. Frac.	ϵ	$\frac{\partial\sigma}{\partial\lvert\cos\theta^*\rvert}$ (nb)
0.0125	503.	0.0163	0.4885	28.313 ± 1.262
0.0375	489.	0.0492	0.4813	27.004 ± 1.221
0.0625	518.	0.0434	0.4897	28.282 ± 1.242
0.0875	517.	0.0290	0.5033	27.882 ± 1.226
0.1125	473.	0.0267	0.5121	25.128 ± 1.156
0.1375	417.	0.0494	0.5145	21.538 ± 1.055
0.1625	463.	0.0411	0.5251	23.634 ± 1.098
0.1875	380.	0.0282	0.5323	19.392 ± 0.994
0.2125	404.	0.0366	0.5449	19.965 ± 0.993
0.2375	373.	0.0158	0.5415	18.950 ± 0.981
0.2625	408.	0.0154	0.5472	20.522 ± 1.016
0.2875	413.	0.0314	0.5508	20.301 ± 0.999
0.3125	534.	0.0312	0.5556	26.027 ± 1.126
0.3375	559.	0.0176	0.5443	28.204 ± 1.193
0.3625	665.	0.0269	0.5538	32.662 ± 1.266
0.3875	814.	0.0148	0.5563	40.300 ± 1.412
0.4125	1054.	0.0236	0.5430	52.978 ± 1.632
0.4375	1237.	0.0130	0.5427	62.878 ± 1.788
0.4625	1526.	0.0173	0.5376	77.968 ± 1.996
0.4875	1941.	0.0184	0.5135	103.714 ± 2.354
0.5125	2148.	0.0162	0.4833	122.219 ± 2.637
0.5375	2602.	0.0184	0.4475	159.546 ± 3.128
0.5625	2491.	0.0218	0.3456	197.062 ± 3.948
0.5875	1720.	0.0370	0.1979	233.934 ± 5.641

$E_{CM} = 3400\ MeV,\ \mathcal{L}_{int} = 1.483\ pb^{-1}$				
$\cos\theta^*$	N_{tot}	Bkg. Frac.	ϵ	$\frac{\partial\sigma}{\partial\lvert\cos\theta^*\rvert}$ (nb)
0.0125	584.	0.0519	0.5091	29.340 ± 1.214
0.0375	619.	0.0435	0.5138	31.083 ± 1.250
0.0625	597.	0.0258	0.5226	30.019 ± 1.228
0.0875	551.	0.0432	0.5245	27.117 ± 1.155
0.1125	526.	0.0514	0.5343	25.195 ± 1.099
0.1375	494.	0.0441	0.5400	23.592 ± 1.062
0.1625	498.	0.0375	0.5550	23.299 ± 1.044
0.1875	462.	0.0321	0.5549	21.738 ± 1.011
0.2125	426.	0.0496	0.5690	19.194 ± 0.930
0.2375	464.	0.0333	0.5726	21.129 ± 0.981
0.2625	409.	0.0351	0.5797	18.363 ± 0.908
0.2875	447.	0.0269	0.5761	20.368 ± 0.963
0.3125	482.	0.0299	0.5867	21.498 ± 0.979
0.3375	559.	0.0315	0.5819	25.096 ± 1.062
0.3625	726.	0.0213	0.5850	32.768 ± 1.216
0.3875	839.	0.0315	0.5827	37.620 ± 1.298
0.4125	1112.	0.0130	0.5768	51.328 ± 1.539
0.4375	1291.	0.0202	0.5773	59.108 ± 1.645
0.4625	1633.	0.0212	0.5653	76.266 ± 1.887
0.4875	2035.	0.0164	0.5425	99.520 ± 2.206
0.5125	2357.	0.0220	0.5175	120.166 ± 2.475
0.5375	2643.	0.0213	0.4665	149.580 ± 2.910
0.5625	2620.	0.0223	0.3760	183.790 ± 3.590
0.5875	1902.	0.0204	0.2194	229.034 ± 5.251

$E_{CM} = 3406\ MeV,\ \mathcal{L}_{int} = 2.680\ pb^{-1}$				
$\cos\theta^*$	N_{tot}	Bkg. Frac.	ϵ	$\frac{\partial\sigma}{\partial\lvert\cos\theta^*\rvert}$ (nb)
0.0125	1036.	0.0406	0.4992	29.718 ± 0.923
0.0375	1108.	0.0339	0.5080	31.454 ± 0.945
0.0625	1111.	0.0237	0.5130	31.560 ± 0.947
0.0875	1013.	0.0300	0.5119	28.648 ± 0.900
0.1125	948.	0.0189	0.5207	26.662 ± 0.866
0.1375	947.	0.0346	0.5358	25.468 ± 0.828
0.1625	890.	0.0262	0.5416	23.882 ± 0.800
0.1875	840.	0.0244	0.5454	22.429 ± 0.774
0.2125	803.	0.0319	0.5554	20.891 ± 0.737
0.2375	769.	0.0360	0.5656	19.564 ± 0.706
0.2625	833.	0.0169	0.5669	21.560 ± 0.747
0.2875	759.	0.0179	0.5640	19.727 ± 0.716
0.3125	930.	0.0223	0.5721	23.722 ± 0.778
0.3375	1020.	0.0202	0.5778	25.817 ± 0.808
0.3625	1178.	0.0233	0.5735	29.944 ± 0.872
0.3875	1414.	0.0181	0.5653	36.658 ± 0.975
0.4125	1851.	0.0130	0.5690	47.921 ± 1.114
0.4375	2292.	0.0191	0.5657	59.314 ± 1.239
0.4625	2700.	0.0198	0.5537	71.342 ± 1.373
0.4875	3350.	0.0164	0.5361	91.739 ± 1.585
0.5125	3916.	0.0179	0.5075	113.109 ± 1.808
0.5375	4433.	0.0191	0.4612	140.713 ± 2.114
0.5625	4460.	0.0208	0.3781	172.372 ± 2.581
0.5875	3361.	0.0222	0.2251	217.926 ± 3.759

$E_{CM} = 3409\ MeV,\ \mathcal{L}_{int} = 1.135\ pb^{-1}$				
$\cos\theta^*$	N_{tot}	Bkg. Frac.	ϵ	$\frac{\partial\sigma}{\partial\lvert\cos\theta^*\rvert}$ (nb)
0.0125	468.	0.0108	0.5227	31.231 ± 1.444
0.0375	521.	0.0346	0.5458	32.494 ± 1.424
0.0625	471.	0.0386	0.5450	29.292 ± 1.350
0.0875	484.	0.0339	0.5392	30.578 ± 1.390
0.1125	434.	0.0481	0.5465	26.655 ± 1.280
0.1375	409.	0.0155	0.5699	24.910 ± 1.232
0.1625	438.	0.0518	0.5717	25.612 ± 1.224
0.1875	339.	0.0295	0.5728	20.252 ± 1.100
0.2125	411.	0.0338	0.5821	24.053 ± 1.186
0.2375	359.	0.0416	0.6008	20.192 ± 1.066
0.2625	359.	0.0299	0.6052	20.290 ± 1.071
0.2875	341.	0.0346	0.5912	19.632 ± 1.063
0.3125	422.	0.0286	0.6025	23.988 ± 1.168
0.3375	453.	0.0419	0.6131	24.958 ± 1.172
0.3625	508.	0.0269	0.6033	28.889 ± 1.282
0.3875	630.	0.0233	0.5972	36.327 ± 1.448
0.4125	810.	0.0223	0.6065	46.041 ± 1.618
0.4375	1033.	0.0212	0.6023	59.194 ± 1.842
0.4625	1220.	0.0114	0.5790	73.447 ± 2.103
0.4875	1508.	0.0145	0.5650	92.734 ± 2.388
0.5125	1754.	0.0137	0.5379	113.390 ± 2.708
0.5375	1969.	0.0183	0.4897	139.161 ± 3.136
0.5625	2013.	0.0164	0.3981	175.330 ± 3.908
0.5875	1428.	0.0354	0.2423	200.468 ± 5.305

$E_{CM} = 3410\ MeV,\ \mathcal{L}_{int} = 1.597\ pb^{-1}$				
$\cos\theta^*$	N_{tot}	Bkg. Frac.	ϵ	$\frac{\partial\sigma}{\partial\lvert\cos\theta^*\rvert}$ (nb)
0.0125	674.	0.0277	0.4861	33.768 $\pm$ 1.300
0.0375	710.	0.0356	0.4961	34.573 $\pm$ 1.298
0.0625	659.	0.0261	0.5038	31.907 $\pm$ 1.243
0.0875	650.	0.0348	0.4969	31.623 $\pm$ 1.240
0.1125	574.	0.0419	0.5073	27.152 $\pm$ 1.133
0.1375	597.	0.0303	0.5237	27.688 $\pm$ 1.133
0.1625	537.	0.0259	0.5349	24.491 $\pm$ 1.057
0.1875	481.	0.0241	0.5274	22.293 $\pm$ 1.016
0.2125	454.	0.0206	0.5386	20.677 $\pm$ 0.970
0.2375	454.	0.0456	0.5596	19.392 $\pm$ 0.910
0.2625	476.	0.0492	0.5553	20.415 $\pm$ 0.936
0.2875	445.	0.0523	0.5458	19.352 $\pm$ 0.917
0.3125	552.	0.0214	0.5598	24.170 $\pm$ 1.029
0.3375	610.	0.0226	0.5661	26.381 $\pm$ 1.068
0.3625	687.	0.0348	0.5573	29.804 $\pm$ 1.137
0.3875	884.	0.0182	0.5528	39.323 $\pm$ 1.322
0.4125	1088.	0.0328	0.5548	47.513 $\pm$ 1.440
0.4375	1353.	0.0152	0.5559	60.043 $\pm$ 1.632
0.4625	1658.	0.0159	0.5307	77.006 $\pm$ 1.891
0.4875	1901.	0.0112	0.5255	89.590 $\pm$ 2.055
0.5125	2297.	0.0226	0.4979	112.929 $\pm$ 2.356
0.5375	2630.	0.0219	0.4511	142.833 $\pm$ 2.785
0.5625	2546.	0.0188	0.3726	167.921 $\pm$ 3.328
0.5875	1993.	0.0269	0.2238	217.078 $\pm$ 4.862

$E_{CM} = 3414\ MeV,\ \mathcal{L}_{int} = 1.944\ pb^{-1}$				
$\cos\theta^*$	N_{tot}	Bkg. Frac.	ϵ	$\frac{\partial\sigma}{\partial\lvert\cos\theta^*\rvert}$ (nb)
0.0125	791.	0.0534	0.4660	33.060 ± 1.175
0.0375	884.	0.0454	0.4801	36.170 ± 1.216
0.0625	781.	0.0298	0.4894	31.857 ± 1.140
0.0875	764.	0.0223	0.4731	32.485 ± 1.175
0.1125	709.	0.0158	0.4849	29.609 ± 1.112
0.1375	734.	0.0349	0.5045	28.892 ± 1.066
0.1625	647.	0.0410	0.5106	25.004 ± 0.983
0.1875	577.	0.0273	0.5082	22.723 ± 0.946
0.2125	589.	0.0295	0.5141	22.881 ± 0.943
0.2375	599.	0.0219	0.5367	22.461 ± 0.918
0.2625	561.	0.0351	0.5376	20.716 ± 0.874
0.2875	602.	0.0305	0.5250	22.876 ± 0.932
0.3125	693.	0.0329	0.5345	25.799 ± 0.980
0.3375	761.	0.0316	0.5445	27.848 ± 1.009
0.3625	923.	0.0200	0.5369	34.666 ± 1.141
0.3875	1051.	0.0140	0.5257	40.556 ± 1.251
0.4125	1281.	0.0260	0.5363	47.868 ± 1.338
0.4375	1541.	0.0157	0.5329	58.564 ± 1.492
0.4625	1894.	0.0204	0.5146	74.187 ± 1.704
0.4875	2270.	0.0242	0.5069	89.906 ± 1.887
0.5125	2576.	0.0179	0.4761	109.334 ± 2.154
0.5375	2747.	0.0238	0.4375	126.110 ± 2.406
0.5625	2976.	0.0267	0.3609	165.129 ± 3.027
0.5875	2334.	0.0312	0.2207	210.803 ± 4.363

$E_{CM} = 3415\ MeV,\ \mathcal{L}_{int} = 2.352\ pb^{-1}$				
$\cos\theta^*$	N_{tot}	Bkg. Frac.	ϵ	$\frac{\partial\sigma}{\partial\lvert\cos\theta^*\rvert}$ (nb)
0.0125	1005.	0.0453	0.4980	32.766 ± 1.034
0.0375	999.	0.0259	0.5203	31.810 ± 1.006
0.0625	984.	0.0389	0.5168	31.122 ± 0.992
0.0875	932.	0.0340	0.5107	29.978 ± 0.982
0.1125	955.	0.0141	0.5143	31.135 ± 1.008
0.1375	891.	0.0219	0.5375	27.573 ± 0.924
0.1625	885.	0.0182	0.5460	27.067 ± 0.910
0.1875	795.	0.0338	0.5387	24.249 ± 0.860
0.2125	720.	0.0226	0.5516	21.698 ± 0.809
0.2375	695.	0.0307	0.5735	19.978 ± 0.758
0.2625	724.	0.0244	0.5725	20.982 ± 0.780
0.2875	757.	0.0184	0.5573	22.676 ± 0.824
0.3125	774.	0.0216	0.5683	22.664 ± 0.815
0.3375	907.	0.0262	0.5843	25.708 ± 0.854
0.3625	1110.	0.0186	0.5722	32.378 ± 0.972
0.3875	1271.	0.0191	0.5624	37.700 ± 1.058
0.4125	1572.	0.0152	0.5723	46.003 ± 1.160
0.4375	1985.	0.0217	0.5681	58.136 ± 1.305
0.4625	2219.	0.0166	0.5513	67.322 ± 1.429
0.4875	2734.	0.0192	0.5382	84.739 ± 1.621
0.5125	3161.	0.0224	0.5146	102.122 ± 1.816
0.5375	3487.	0.0244	0.4661	124.126 ± 2.102
0.5625	3714.	0.0165	0.3867	160.634 ± 2.636
0.5875	2981.	0.0237	0.2348	210.826 ± 3.862

$E_{CM} = 3416\ MeV,\ \mathcal{L}_{int} = 2.467\ pb^{-1}$				
$\cos\theta^*$	N_{tot}	Bkg. Frac.	ϵ	$\frac{\partial\sigma}{\partial\lvert\cos\theta^*\rvert}$ (nb)
0.0125	940.	0.0025	0.4832	30.969 ± 1.010
0.0375	957.	0.0437	0.4988	29.749 ± 0.962
0.0625	1008.	0.0329	0.5018	31.498 ± 0.992
0.0875	889.	0.0375	0.4902	28.303 ± 0.949
0.1125	889.	0.0232	0.4998	28.174 ± 0.945
0.1375	857.	0.0237	0.5208	26.050 ± 0.890
0.1625	852.	0.0209	0.5277	25.633 ± 0.878
0.1875	751.	0.0373	0.5223	22.446 ± 0.819
0.2125	779.	0.0216	0.5320	23.228 ± 0.832
0.2375	742.	0.0256	0.5533	21.184 ± 0.778
0.2625	748.	0.0161	0.5537	21.552 ± 0.788
0.2875	668.	0.0167	0.5384	19.780 ± 0.765
0.3125	822.	0.0205	0.5502	23.724 ± 0.828
0.3375	955.	0.0240	0.5653	26.733 ± 0.865
0.3625	1090.	0.0173	0.5503	31.562 ± 0.956
0.3875	1292.	0.0165	0.5425	37.984 ± 1.057
0.4125	1598.	0.0151	0.5566	45.848 ± 1.147
0.4375	1851.	0.0158	0.5470	53.996 ± 1.255
0.4625	2297.	0.0195	0.5258	69.456 ± 1.449
0.4875	2743.	0.0201	0.5256	82.920 ± 1.583
0.5125	3149.	0.0172	0.4937	101.652 ± 1.811
0.5375	3423.	0.0172	0.4505	121.076 ± 2.069
0.5625	3611.	0.0177	0.3758	153.051 ± 2.547
0.5875	2928.	0.0237	0.2302	201.358 ± 3.721

$E_{CM} = 3418\ MeV,\ \mathcal{L}_{int} = 1.466\ pb^{-1}$				
$\cos\theta^*$	N_{tot}	Bkg. Frac.	ϵ	$\frac{\partial\sigma}{\partial\lvert\cos\theta^*\rvert}$ (nb)
0.0125	474.	0.0371	0.5182	28.976 ± 1.331
0.0375	542.	0.0510	0.5372	31.499 ± 1.353
0.0625	516.	0.0490	0.5408	29.852 ± 1.314
0.0875	475.	0.0238	0.5329	28.620 ± 1.313
0.1125	455.	0.0328	0.5344	27.090 ± 1.270
0.1375	462.	0.0425	0.5636	25.821 ± 1.201
0.1625	452.	0.0447	0.5688	24.971 ± 1.174
0.1875	409.	0.0435	0.5616	22.914 ± 1.133
0.2125	389.	0.0412	0.5763	21.290 ± 1.079
0.2375	409.	0.0189	0.5992	22.030 ± 1.089
0.2625	390.	0.0125	0.5989	21.154 ± 1.071
0.2875	415.	0.0197	0.5803	23.061 ± 1.132
0.3125	472.	0.0378	0.5898	25.328 ± 1.166
0.3375	508.	0.0462	0.6130	25.999 ± 1.154
0.3625	561.	0.0395	0.5938	29.852 ± 1.260
0.3875	680.	0.0267	0.5824	37.380 ± 1.434
0.4125	839.	0.0203	0.5980	45.215 ± 1.561
0.4375	958.	0.0148	0.5936	52.305 ± 1.690
0.4625	1263.	0.0202	0.5711	71.275 ± 2.006
0.4875	1504.	0.0236	0.5703	84.711 ± 2.184
0.5125	1750.	0.0242	0.5345	105.102 ± 2.512
0.5375	1844.	0.0228	0.4852	122.172 ± 2.845
0.5625	2057.	0.0267	0.4027	163.514 ± 3.605
0.5875	1586.	0.0333	0.2538	198.727 ± 4.990

$E_{CM} = 3422\ MeV,\ \mathcal{L}_{int} = 2.153\ pb^{-1}$				
$\cos\theta^*$	N_{tot}	Bkg. Frac.	ϵ	$\frac{\partial\sigma}{\partial\lvert\cos\theta^*\rvert}$ (nb)
0.0125	790.	0.0281	0.4863	29.339 ± 1.044
0.0375	776.	0.0482	0.5148	26.663 ± 0.957
0.0625	849.	0.0277	0.5165	29.699 ± 1.019
0.0875	715.	0.0335	0.5028	25.538 ± 0.955
0.1125	686.	0.0272	0.5049	24.562 ± 0.938
0.1375	722.	0.0260	0.5363	24.365 ± 0.907
0.1625	704.	0.0321	0.5419	23.364 ± 0.880
0.1875	599.	0.0178	0.5311	20.588 ± 0.841
0.2125	667.	0.0392	0.5409	22.016 ± 0.852
0.2375	624.	0.0306	0.5731	19.615 ± 0.785
0.2625	630.	0.0497	0.5635	19.743 ± 0.786
0.2875	640.	0.0286	0.5476	21.100 ± 0.834
0.3125	711.	0.0265	0.5639	22.809 ± 0.856
0.3375	847.	0.0273	0.5818	26.315 ± 0.904
0.3625	867.	0.0255	0.5634	27.870 ± 0.947
0.3875	1150.	0.0208	0.5533	37.819 ± 1.115
0.4125	1348.	0.0185	0.5707	43.076 ± 1.174
0.4375	1621.	0.0146	0.5613	52.884 ± 1.313
0.4625	1969.	0.0101	0.5398	67.100 ± 1.512
0.4875	2462.	0.0179	0.5352	83.947 ± 1.692
0.5125	2901.	0.0230	0.5130	102.668 ± 1.906
0.5375	3191.	0.0196	0.4609	126.127 ± 2.233
0.5625	3433.	0.0198	0.3897	160.462 ± 2.738
0.5875	2749.	0.0280	0.2443	203.224 ± 3.876

$E_{CM} = 3426\ MeV,\ \mathcal{L}_{int} = 1.800\ pb^{-1}$				
$\cos\theta^*$	N_{tot}	Bkg. Frac.	ϵ	$\frac{\partial\sigma}{\partial\lvert\cos\theta^*\rvert}$ (nb)
0.0125	627.	0.0416	0.4744	28.150 ± 1.124
0.0375	622.	0.0350	0.5003	26.657 ± 1.069
0.0625	616.	0.0354	0.5041	26.196 ± 1.056
0.0875	561.	0.0243	0.4813	25.272 ± 1.067
0.1125	577.	0.0265	0.4882	25.565 ± 1.064
0.1375	564.	0.0319	0.5190	23.377 ± 0.984
0.1625	583.	0.0372	0.5226	23.871 ± 0.989
0.1875	494.	0.0396	0.5098	20.680 ± 0.931
0.2125	468.	0.0534	0.5276	18.658 ± 0.862
0.2375	521.	0.0284	0.5583	20.149 ± 0.883
0.2625	482.	0.0410	0.5479	18.746 ± 0.854
0.2875	535.	0.0334	0.5316	21.618 ± 0.935
0.3125	592.	0.0272	0.5393	23.731 ± 0.975
0.3375	669.	0.0239	0.5692	25.494 ± 0.986
0.3625	733.	0.0263	0.5427	29.224 ± 1.079
0.3875	887.	0.0239	0.5328	36.110 ± 1.212
0.4125	1072.	0.0211	0.5542	42.078 ± 1.285
0.4375	1330.	0.0194	0.5444	53.237 ± 1.460
0.4625	1594.	0.0153	0.5231	66.683 ± 1.670
0.4875	1963.	0.0175	0.5196	82.483 ± 1.862
0.5125	2288.	0.0234	0.4966	99.984 ± 2.090
0.5375	2544.	0.0183	0.4509	123.088 ± 2.440
0.5625	2782.	0.0148	0.3815	159.638 ± 3.026
0.5875	2411.	0.0221	0.2422	216.286 ± 4.405

$E_{CM} = 3430\ MeV,\ \mathcal{L}_{int} = 1.438\ pb^{-1}$				
$\cos\theta^*$	N_{tot}	Bkg. Frac.	ϵ	$\frac{\partial\sigma}{\partial\lvert\cos\theta^*\rvert}$ (nb)
0.0125	491.	0.0362	0.4590	28.673 ± 1.294
0.0375	515.	0.0310	0.4830	28.734 ± 1.266
0.0625	483.	0.0402	0.4865	26.500 ± 1.206
0.0875	491.	0.0330	0.4625	28.553 ± 1.289
0.1125	442.	0.0535	0.4713	24.685 ± 1.174
0.1375	471.	0.0345	0.5012	25.235 ± 1.162
0.1625	446.	0.0237	0.5102	23.737 ± 1.124
0.1875	438.	0.0239	0.4919	24.174 ± 1.155
0.2125	381.	0.0343	0.5029	20.349 ± 1.042
0.2375	380.	0.0180	0.5343	19.425 ± 0.996
0.2625	367.	0.0191	0.5311	18.852 ± 0.984
0.2875	406.	0.0275	0.5095	21.554 ± 1.070
0.3125	401.	0.0408	0.5231	20.453 ± 1.022
0.3375	493.	0.0426	0.5469	24.002 ± 1.081
0.3625	570.	0.0291	0.5262	29.250 ± 1.225
0.3875	667.	0.0209	0.5203	34.912 ± 1.352
0.4125	828.	0.0236	0.5344	42.077 ± 1.462
0.4375	991.	0.0339	0.5242	50.795 ± 1.613
0.4625	1244.	0.0215	0.4994	67.785 ± 1.922
0.4875	1467.	0.0258	0.5058	78.581 ± 2.052
0.5125	1726.	0.0213	0.4786	98.174 ± 2.363
0.5375	1930.	0.0271	0.4345	120.180 ± 2.736
0.5625	2133.	0.0278	0.3750	153.801 ± 3.330
0.5875	1767.	0.0270	0.2405	198.772 ± 4.729

$E_{CM} = 3470\ MeV,\ \mathcal{L}_{int} = 2.513\ pb^{-1}$				
$\cos\theta^*$	N_{tot}	Bkg. Frac.	ϵ	$\frac{\partial\sigma}{\partial\lvert\cos\theta^*\rvert}$ (nb)
0.0125	945.	0.0228	0.5018	29.292 ± 0.953
0.0375	961.	0.0328	0.5442	27.185 ± 0.877
0.0625	937.	0.0348	0.5410	26.608 ± 0.869
0.0875	832.	0.0334	0.5033	25.434 ± 0.882
0.1125	870.	0.0249	0.5098	26.488 ± 0.898
0.1375	815.	0.0253	0.5601	22.574 ± 0.791
0.1625	805.	0.0357	0.5619	21.988 ± 0.775
0.1875	733.	0.0237	0.5278	21.581 ± 0.797
0.2125	727.	0.0248	0.5441	20.742 ± 0.770
0.2375	722.	0.0395	0.6002	18.390 ± 0.684
0.2625	712.	0.0357	0.5862	18.643 ± 0.699
0.2875	673.	0.0261	0.5514	18.920 ± 0.730
0.3125	708.	0.0322	0.5741	19.000 ± 0.714
0.3375	851.	0.0208	0.6174	21.482 ± 0.736
0.3625	914.	0.0233	0.5688	24.984 ± 0.826
0.3875	1130.	0.0137	0.5563	31.892 ± 0.949
0.4125	1409.	0.0139	0.5993	36.907 ± 0.983
0.4375	1660.	0.0142	0.5820	44.754 ± 1.098
0.4625	1888.	0.0186	0.5418	54.431 ± 1.253
0.4875	2455.	0.0150	0.5631	68.349 ± 1.379
0.5125	2743.	0.0244	0.5428	78.472 ± 1.498
0.5375	3061.	0.0203	0.4828	98.856 ± 1.787
0.5625	3400.	0.0242	0.4463	118.316 ± 2.029
0.5875	3178.	0.0306	0.3169	154.729 ± 2.745

Appendix B

Neutral DST Production and Efficiency

The process of neutral data analysis in E835 began with the creation of the NDSTs. These Neutral Data Summary Tapes allowed quicker access to data for many neutral analyses by using event topology to classify neutral events. Based upon the number of clusters contained within the events, the NDST production filtered raw data events into three possible streams (C,L,T) [66].

NDST sets C and L selected events with specific numbers of clusters contained within the CCAL. Set C was the general purpose neutral dataset and selected events with no less than 2 and no greater than 9 i.o.u.[1] clusters utilizing 25/50 MeV (seed/cluster) thresholds. Set L was optimized for low energy photon detection by using 5/20 MeV cluster thresholds and selecting events with between 2 and 4 i.o.u. clusters. Finally, set T used the same selection criteria as set C but set T included i.o.u. clusters detected in the FCAL.

Data reduction was achieved in the NDST production through two methods. First, the amount of information contained within each data event was reduced. For example, information pertaining to charged particle tracking was removed. The list of information retained for each event written to a NDST is listed in table B.1. Second, longitudinal (15%) and transverse (350 MeV) momentum cuts were applied on each neutral event passing the filtering process, insuring strict

[1] In-time Or Undetermined.

Information Contained in the NDSTs:
Gateway buffer, run, event, and processor #
Error flag, KPRID, # of trigger words
Event time (from processor clock)
of CCAL & FCAL clusters
of i.o.u. CCAL & FCAL clusters
of in-time CCAL & FCAL clusters
of CCAL & FCAL clusters with $E \geq 75MeV$
of CCAL & FCAL clusters with $E \geq 100MeV$
of CCAL clusters in rings 2-19
For each CCAL (FCAL) cluster:
Total energy
Position in ring & wedge (block) units
Cluster mass*
Split, shared, or isolated cluster flag
Timing flag and cluster time
Ratio of uncorrected to corrected energy*
Hitmap for the 3×3 grid*
$*$: CCAL only

Table B.1: Event information contained in the NDSTs.

adherence to conservation of momentum.

The momentum cuts placed upon the data cause analysis dependent efficiencies to arise. For the $\pi^0\pi^0$ analysis the ratio of the number of $\pi^0\pi^0$ events from a NDST to the number of $\pi^0\pi^0$ events from the corresponding raw data tape was taken as the NDST efficiency, for each energy point. The NDST efficiency is rate and energy dependent. The rate dependence is attributed to overlapping event contamination which is discussed in detail in section 4.3.1. The energy dependence is attributed to the hard cut on the transverse momentum; as the $\bar{p}$ momentum increases, the transverse momentum distribution broadens causing an increasing inefficiency [67]. No appreciable angular dependence in the efficiency was seen in the NDST production.

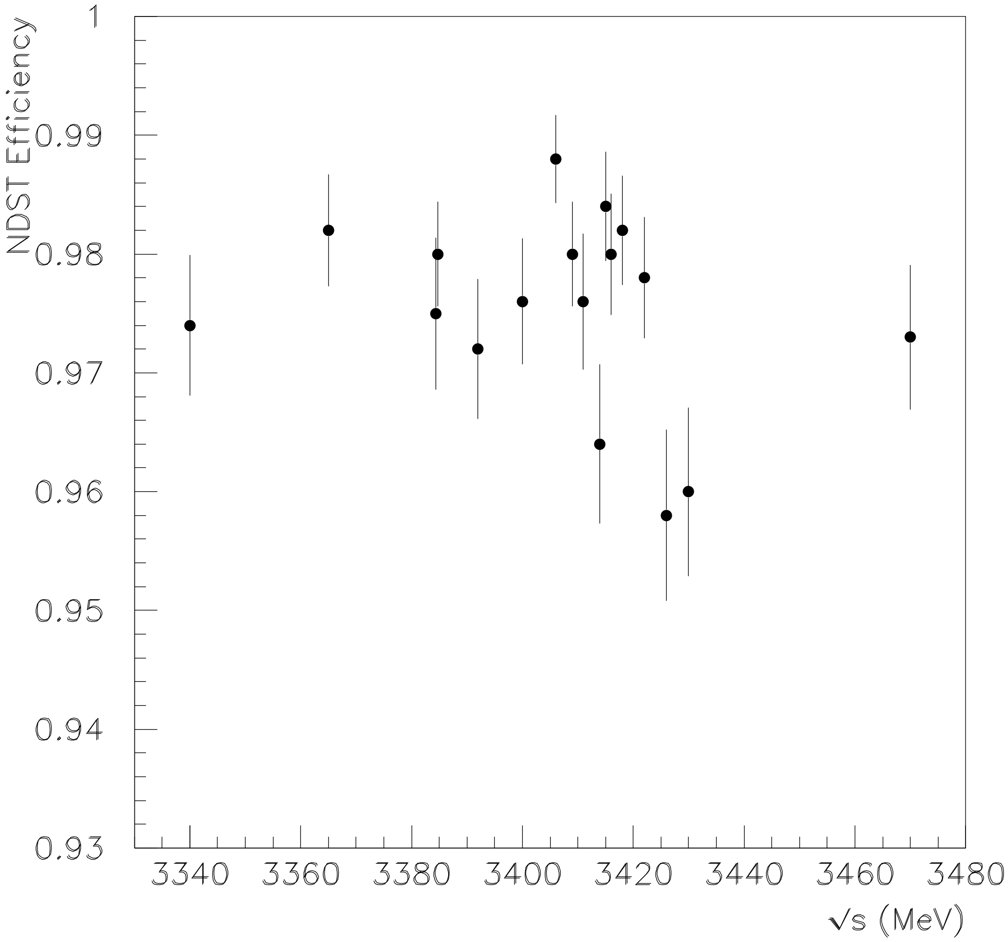

Figure B.1: NDST efficiency versus center of mass energy in the χ_{c0} region. There is no appreciable energy dependence in this small energy region.

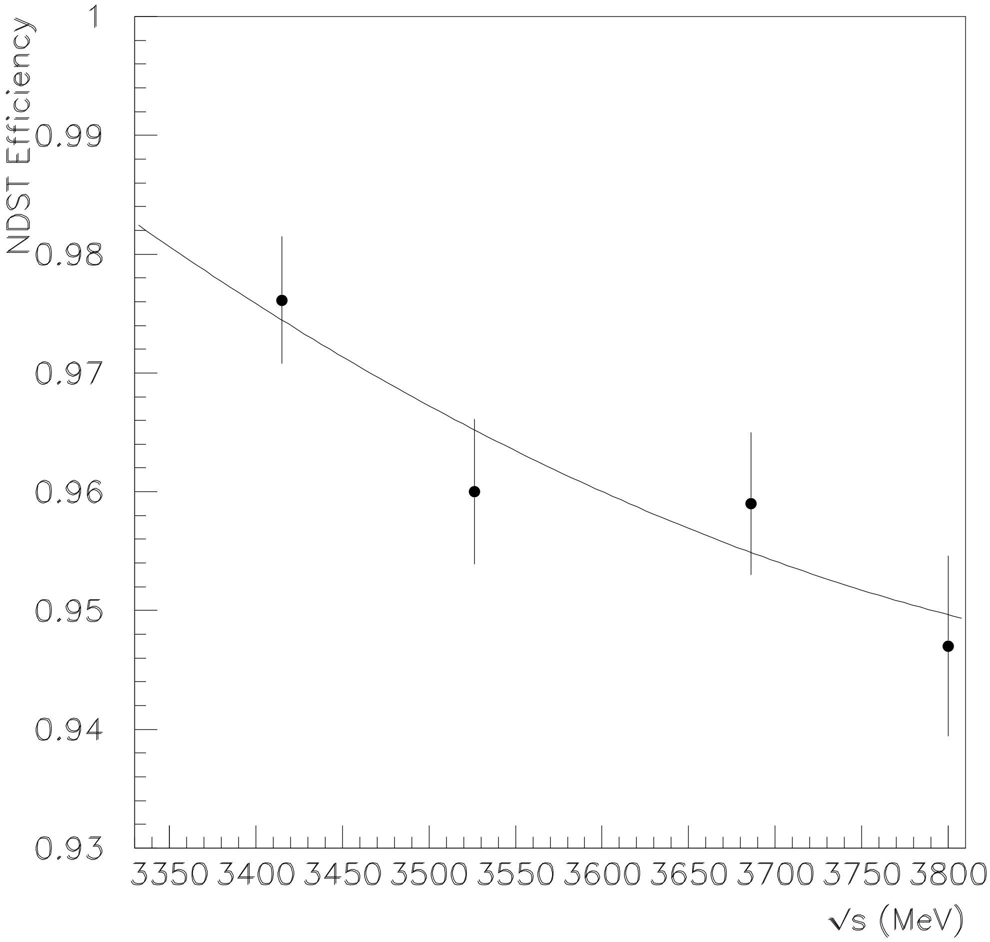

Figure B.2: The energy dependence of the Neutral DST efficiency over large regions of $\sqrt{s}$ .The value of the efficiency at the χ_{c0} is calculated as the luminosity weighted average of all of the efficiencies in the χ_{c0} region. the fitted equation is: $\epsilon_{NDST} = 2.08 - 5.6 \times 10^{-4}\sqrt{s} + 6.8 \times 10^{-8}(\sqrt{s})^2$

Appendix C

Angular Dependence of the Differential Cross Section

The Lorentz invariance of the helicity operator ($\lambda = \vec{S} \cdot \hat{p}$) makes the helicity formalism the favored method of calculating the angular dependence in multi-particle relativistic scattering processes. The helicity formalism was developed by Jacob and Wick in 1959 [68] and it's power arises from the ability to define reference frames that are at rest with respect with one another, unlike the spin-orbit formalism. The definition of these reference frames allows the formation of basis states that are eigenstates of either linear or total angular momentum and helicity [69].

The following offers a brief introduction to the important D-functions and two-body decays in the helicity formalism. The differential cross section of $p\bar{p} \to \pi^0\pi^0$ is then calculated using the helicity formalism using the phase conventions of Jacob and Wick.

C.1 Introduction to D-Functions

The D-functions are matrix elements of the quantum mechanical rotation operator and are defined as the expectation that an angular momentum state, $|J, M\rangle$, will be rotated into the state $|J, M'\rangle$:

$$D^J_{M',M}(\alpha\beta\gamma) \equiv \langle J, M'|\, R(\alpha\beta\gamma)\, |J, M\rangle \tag{C.1}$$

Using the definition of the rotation operator, $R(\alpha\beta\gamma) \equiv e^{\imath\alpha J_z} e^{\imath\beta J_y} e^{\imath\gamma J_z}$ the D-functions may be written as:

$$D^J_{M',M}(\alpha\beta\gamma) \equiv e^{\imath\alpha M'} d^J_{M',M}(\beta) e^{\imath\gamma M} \tag{C.2}$$

Where the rotation is governed by the Euler angles $(\alpha\beta\gamma)$. The rotation of the angular momentum state with respect to the $\hat{y}$ axis, $d^J_{M',M}(\beta) = \langle J, M'| \, e^{\imath\beta J_y} \, |J, M\rangle$, is given by the Wigner formula:

$$\begin{aligned} d^J_{M',M}(\beta) = \sum_n \Bigg\{ & \frac{(-1)^n \left[(J+M)!(J-M)!(J+M')!(J-M')!\right]^{\frac{1}{2}}}{(J-M-n)!(J+M-n)!(n+M'-M)!n!} \\ & \times \left(\cos\frac{\beta}{2}\right)^{2J+M-M'-2n} \left(-\sin\frac{\beta}{2}\right)^{M'-M+2n} \Bigg\} \end{aligned} \tag{C.3}$$

C.2 Two-Body Decays in the Helicity Formalism

In the helicity formalism the decay amplitude for a simple two-body decay, $a \to b + c$, is:

$$A = \langle \theta, \phi, \lambda_b, \lambda_c | \, H \, |J, M\rangle \tag{C.4}$$

Where H is the Hamiltonian and represents the coupling of a single particle in a definite momentum state, $|J, M\rangle$, to a two particle composite state with decay angles, θ, ϕ and helicities λ_b, λ_c. Additionally, in the center of momentum frame, the determination of the decay amplitude is not dependent upon the magnitude of the final state momentum, $|\,\vec{p}\,|$. Furthermore, due to the conservation of angular momentum, there should be no dependence in the amplitude on the coupling between the initial and final state angular momenta. This dependence is removed explicitly by introducing a complete set of two particle helicity states into equation C.4:

$$\begin{aligned} A &= \sum_{j,m} \langle \theta, \phi, \lambda_b, \lambda_c | \, j, m, \lambda_b, \lambda_c\rangle \, \langle j, m, \lambda_b, \lambda_c| \, H \, |J, M\rangle \\ &= \sum_{j,m} \langle \theta, \phi, \lambda_b, \lambda_c | \, j, m, \lambda_b, \lambda_c\rangle \, \delta_{J,j}\delta_{M,m} A_{\lambda_b,\lambda_c} \\ &= \langle \theta, \phi, \lambda_b, \lambda_c | \, J, M, \lambda_b, \lambda_c\rangle \, A_{\lambda_b,\lambda_c} \end{aligned} \tag{C.5}$$

Where A_{λ_b,λ_c} represents the coupling of the initial state's helicity to the final state helicities. It has been shown [69] that the transformation of a plane wave basis into a spherical wave basis is:

$$\langle \theta, \phi, \lambda_b, \lambda_c \mid J, M, \lambda_b, \lambda_c \rangle = \kappa_J D^{J*}_{M,\lambda_b - \lambda_c}(\phi, \theta, -\phi) \tag{C.6}$$

Where the $*$ implies the complex conjugate, κ_J is a normalization constant, $\kappa_J = \sqrt{\frac{2J+1}{4\pi}}$, and γ is arbitrary and is chosen as $-\phi$. Substituting equation C.6 into C.5 the amplitude for a simple two body decay becomes:

$$A = \sqrt{\frac{2J+1}{4\pi}} D^{J*}_{M,\lambda_b - \lambda_c}(\phi, \theta, -\phi) A_{\lambda_b,\lambda_c} \tag{C.7}$$

C.3 Calculation of the $\pi^0\pi^0$ Differential Cross Section

The angular distribution for the process $\bar{p}p \to \pi^0\pi^0$ is now calculated by dividing the interaction into 2 two-body decays. The helicity amplitudes for the individual processes are:

$$A_1^J(\bar{p}p \to J^{PC}) = F^{J,\sqrt{s}}_{\lambda_p,\lambda_{\bar{p}}} D^J_{M,\lambda_i}(\phi_{\bar{p}}, \theta_{\bar{p}}, -\phi_{\bar{p}}) \tag{C.8}$$

$$A_2^J(J^{PC} \to \pi^0\pi^0) = B^{J,\sqrt{s}}_{\lambda_{\pi_1^0},\lambda_{\pi_2^0}} D^{J*}_{M,\lambda_f}(\phi_{\pi_1^0}, \theta^*, -\phi_{\pi_1^0}) \tag{C.9}$$

$$\tag{C.10}$$

Where the normalization constant, $\sqrt{\frac{2J+1}{4\pi}}$, has been absorbed into the coefficients, $\lambda_i = \lambda_p - \lambda_{\bar{p}}$, $\lambda_f = \lambda_{\pi_1^0} - \lambda_{\pi_2^0}$, and all helicities are summed over.

The interaction amplitude for a state with total angular momentum J is given by:

$$A^J(\bar{p}p \to \pi^0\pi^0) = \prod_{i=1}^{4} A_i^J \tag{C.11}$$

The spinless π^0 has no helicity. Thus, the decay amplitude becomes:

$$A^J(\bar{p}p \to \pi^0\pi^0) = F^{J,\sqrt{s}}_{\lambda_p,\lambda_{\bar{p}}} B^{J,\sqrt{s}}_{0,0} D^J_{M,\lambda_i}(\phi_{\bar{p}}, \theta_{\bar{p}}, -\phi_{\bar{p}}) D^{J*}_{M,0}(\phi_{\pi_1^0}, \theta^*, -\phi_{\pi_1^0}) \tag{C.12}$$

The $\pi^0\pi^0$ azimuthal quantization axis is chosen as $\phi_{\pi_1^0} = 0$. This implies:

$$A^J = F^{J,\sqrt{s}}_{\lambda_p,\lambda_{\bar{p}}} B^{J,\sqrt{s}}_{0,0} D^J_{M,\lambda_i}(\phi_{\bar{p}}, \theta_{\bar{p}}, -\phi_{\bar{p}}) P_J(\cos\theta^*) \tag{C.13}$$

Where the Legendre polynomials, $P_J(\cos\theta^*) = D^J_{M,0}(0,\theta^*,0)$. Similarly, if the initial $p\bar{p}$ state's polar quantization axis is chosen as $\theta_{\bar{p}} = 0$:

$$A^J = F^{J,\sqrt{s}}_{\lambda_p,\lambda_{\bar{p}}} B^{J,\sqrt{s}}_{0,0} D^J_{M,\lambda_i}(\phi_{\bar{p}}, 0, -\phi_{\bar{p}}) P_J(\cos\theta^*) \tag{C.14}$$

With the use of equation C.2, the amplitude simplifies to:

$$\begin{aligned} A^J &= F^{J,\sqrt{s}}_{\lambda_p\lambda_{\bar{p}}} B^{J,\sqrt{s}}_{0,0} e^{i\phi_{\bar{p}}(M-\lambda_i)} \delta_{M,\lambda_i} P_J(\cos\theta^*) \\ &= F^{J,\sqrt{s}}_{\lambda_p,\lambda_{\bar{p}}} B^{J,\sqrt{s}}_{0,0} P_J(\cos\theta^*) \end{aligned} \tag{C.15}$$

For a 2 body strong decay, $a \to b + c$, with energy dependent decay amplitude, $A_{\lambda_b\lambda_c}$, and angular momentum, J, parity and charge parity are conserved. In the helicity formalism, the expression for C-parity conservation is:

$$A_{\lambda_b,\lambda_c} = (-1)^J A_{\lambda_c,\lambda_b} \tag{C.16}$$

The above implies the total angular momentum of the $\pi^0\pi^0$ final state must be even and the C-parity eigenvalue is +1, from $B^{J,\sqrt{s}}_{0,0} = (-1)^J B^{J,\sqrt{s}}_{0,0}$. Additionally, due to the spinless π^0 and the even total angular momentum, the final state orbital angular momentum must be even. This implies that the parity of the $\pi^0\pi^0$ final state must also have an eigenvalue of +1. The expression for parity conservation is:

$$A_{\lambda_b,\lambda_c} = P_a P_b P_c (-1)^L A_{-\lambda_b,-\lambda_c} \tag{C.17}$$

The final state quantum numbers are $J^{PC} = even^{++}$. Using expressions C.16 and C.17, J^{PC} conservation, the initial state orbital angular momentum is found to be odd, implying the initial state spin, $S_{p\bar{p}} = 1$. Furthermore, the following identities are obtained:

$$F^{J,\sqrt{s}}_{\frac{1}{2},\frac{1}{2}} = -F^{J,\sqrt{s}}_{-\frac{1}{2},-\frac{1}{2}} \quad \text{and} \quad F^{J,\sqrt{s}}_{\frac{1}{2},-\frac{1}{2}} = F^{J,\sqrt{s}}_{-\frac{1}{2},\frac{1}{2}} \tag{C.18}$$

These identities imply the initial state contribution to the decay amplitude, A_J, is fully determined by the initial state helicities, $\lambda_i = 0, 1$, rather than $\lambda_i = 0, \pm 1$. The differential cross section is given by:

$$\frac{d\sigma}{d\Omega} = \left| \sum_{J,\lambda_i} A^J \right|^2 = \left| \sum_{J,\lambda_i} C_J(\sqrt{s}) P_J(\cos\theta^*) \right|^2 \tag{C.19}$$

Where, $C_J(\sqrt{s}) \equiv F^{J.\sqrt{s}}_{\lambda_p,\lambda_{\bar{p}}} B^{J,\sqrt{s}}_{0,0}$. Therefore, after summing over initial helicity states, the differential cross section becomes:

$$\frac{d\sigma}{d\Omega} == \left| \sum_{J=0}^{even} C_J(\sqrt{s}) P_J(\cos\theta^*) \right|^2 + \left| \sum_{J=2}^{even} C^1_J(\sqrt{s}) P^1_J(\cos\theta^*) \right|^2 \tag{C.20}$$

Where the first term is due to an initial state with transverse polarization and the second term is attributed to an initial state with longitudinal polarization. The associated Legendre polynomial appears due to the spin-orientation change associated with a longitudinally polarized initial state.

References

[1] Obtained from http://particleadventure.org/particleadventure/

[2] M. Gell-Mann, "A Schematic Model Of Baryons And Mesons," Phys. Lett. **8** (1964) 214.

[3] G. Zweig, "An SU(3) Model For Strong Interaction Symmetry And Its Breaking. 2," CERN-TH-412.

[4] M. Gell-Mann, "Symmetries Of Baryons And Mesons," Phys. Rev. **125**, 1067 (1962).

[5] Y. Hara, "Unitary Triplets And The Eightfold Way," Phys. Rev. **134**, B701 (1964).

[6] J. D. Bjorken and S. L. Glashow, "Elementary Particles And SU(4)," Phys. Lett. **11**, 255 (1964).

[7] N. Cabibbo, "Unitary Symmetry And Leptonic Decays," Phys. Rev. Lett. **10**, 531 (1963).

[8] S. L. Glashow, J. Iliopoulos and L. Maiani, "Weak Interactions With Lepton - Hadron Symmetry," Phys. Rev. D **2**, 1285 (1970).

[9] J. J. Aubert *et al.*, "Experimental Observation Of A Heavy Particle J," Phys. Rev. Lett. **33**, 1404 (1974).

[10] J. E. Augustin *et al.*, "Discovery Of A Narrow Resonance In E+ E- Annihilation," Phys. Rev. Lett. **33**, 1406 (1974).

[11] T. Appelquist and H. D. Politzer, "Heavy Quarks And Longlived Hadrons," Phys. Rev. D **12**, 1404 (1975).

[12] G. S. Abrams *et al.*, "The Discovery Of A Second Narrow Resonance In E+ E- Annihilation," Phys. Rev. Lett. **33**, 1453 (1974).

[13] T. Appelquist and H. D. Politzer, "Orthocharmonium And e^+e^- Annihilation," Phys. Rev. Lett. **34**, 43 (1975).

[14] S. Okubo, "Phi Meson And Unitary Symmetry Model," Phys. Lett. **5**, 165 (1963).

[15] J. Iizuka, "Systematics And Phenomenology Of Meson Family," Prog. Theor. Phys. Suppl. **37**, 21 (1966).

[16] G. J. Feldman *et al.*, "Psi-Prime (3684) Radiative Decays To High Mass States," Phys. Rev. Lett. **35**, 821 (1975) [Erratum-ibid. **35**, 1184 (1975)].

[17] W. Braunschweig and et al. [DASP Collaboration], "Observation Of The Two Photon Cascade 3.7-Gev $\rightarrow$ 3.1-Gev + Gamma Gamma Via An Intermediate State P - Charm," Phys. Lett. B **57**, 407 (1975).

[18] E. Eichten, K. Gottfried, T. Kinoshita, K. D. Lane and T. M. Yan, "Charmonium: Comparison With Experiment," Phys. Rev. D **21**, 203 (1980).

[19] J. Pumplin, W. Repko and A. Sato, "Fine Structure Corrections And Electromagnetic Decays Of Charmonium," Phys. Rev. Lett. **35**, 1538 (1975).

[20] H. J. Schnitzer, "The P - States Of Charmonium And The Forces That Confine Quarks," Phys. Rev. Lett. **35**, 1540 (1975).

[21] A. B. Henriques, B. H. Kellett and R. G. Moorhouse, "Radiative Transitions And The P Wave Levels In Charmonium," Phys. Lett. B **64**, 85 (1976).

[22] K. Seth, Based on a plot provided by Kamal Seth.

[23] S. Van Der Meer, "Stochastic Cooling And The Accumulation Of Anti-Protons," Rev. Mod. Phys. **57**, 689 (1985).

[24] C. Baglin *et al.*, "J / Psi Resonance Formation And Mass Measurement In Anti-Proton - Proton Annihilations," Nucl. Phys. B **286**, 592 (1987).

[25] C. Baglin *et al.*, "Direct Observation And Partial Width Measurement Of $\gamma\gamma$ Decay Of Charmonium States," Phys. Lett. B **187**, 191 (1987).

[26] C. Baglin *et al.* [R704 Collaboration], "Search For The P Wave Singlet Charmonium State In Anti-P P Annihilations At The Cern Intersecting Storage Rings," Phys. Lett. B **171**, 135 (1986).

[27] A comprehensive list of all publications from experiments E760, E835, and E835$'$ can be found at: http://www.e835.to.infn.it.

[28] K. Hagiwara *et al.* [Particle Data Group Collaboration], "Review Of Particle Physics," Phys. Rev. D **66**, 010001 (2002).

[29] R. A. Lee, "Radiative Decays Of The Psi-Prime To All Photon Final States," SLAC-0282.

[30] J. Z. Bai *et al.* [BES Collaboration], "Radiative decay of the psi(2S) into two pseudoscalar mesons," arXiv:hep-ex/0109040.

[31] Michelle D. Stancari, "Two Photon Decay Widths of Charmonium Resonances Formed in Proton-Antiproton Annihilations," PhD Dissertation, University of California, Irvine, (1999).

[32] D. Allspach *et al.*, "The Variable Density Gas Jet Internal Target For Experiment 835 at Fermilab,"Nucl. Instrum. Meth. A **410**, 75 (1998).

[33] D. Joffe, "A Search for the Singlet P State of Charmonium in Proton-Antiproton Annihilations at Fermilab Experiment E835′," PhD Dissertation, Northwestern University, To be published.

[34] S. Bagnasco *et al.*, "A Straw Chambers' Tracker For The High Rate Experiment 835 At The Fermilab Accumulator,"Nucl. Instrum. Meth. A **409**, 75 (1998).

[35] M. Ambrogiani, W. Baldini, D. Bettoni, R. Calabrese, E. Luppi, R. Mussa and G. Stancari, "Results From The E835 Scintillating Fiber Detector," Nucl. Instrum. Meth. A **419**, 632 (1998).

[36] W. Baldini, D. Bettoni, R. Calabrese, E. Luppi, R. Mussa, M. Negrini and G. Stancari, "The New Scintillating Fiber Detector Of E835 At Fermilab," Nucl. Instrum. Meth. A **461**, 219 (2001)

[37] S. Bagnasco *et al.*, "The Threshold Gas Cherenkov Counter Of Charmonium Experiment 835 At Fermilab," Nucl. Instrum. Meth. A **424**, 304 (1999).

[38] M. Ambrogiani *et al.* [E835 Collaboration], "Measurements of the magnetic form factor of the proton in the timelike region at large momentum transfer," Phys. Rev. D **60**, 032002 (1999).

[39] James E. Fast, "Two Photon Decays of Charmonium States Produced in Proton-Antiproton Annihilations," PhD Dissertation, University of California, Irvine, (1992).

[40] M. Graham, private communication.

[41] Keith E. Gollwitzer, "The Charmonium $^1P_1$ State (h_c) Produced in Antiproton-Proton Annihilations," PhD Dissertation, University of California, Irvine, (1993).

[42] M. Ambrogiani *et al.* [E835 Collaboration], "Experiment E835 at Fermilab," To be published.

[43] M. Graham and S.H. Seo, "Modifications to the FCAL2000 Clusterizer," E835 Internal Memo.

[44] The FNAL Beams Division, "The Big Picture in Hardware and Software," http://www-bd.fnal.gov/controls/overview/overview.html.

[45] G. Oleynik *et al.*, "Fermilab DART run control," IEEE Trans. Nucl. Sci. **43**, 20 (1996).

[46] DART Collaboration and FNAL Computing Division, "DYC3 Write-Up v1.0," http://fnphyx-www.fnal.gov/elec/dyc3/dyc3nov.html.

[47] W. Baldini *et al.*, "The Charged Trigger of the Experiment E835 at Fermilab," Nucl. Instrum. Meth. A **449**, 331 (2000).

[48] R. Ray *et al.*, "A Trigger for the Fermilab E760 Lead Glass Calorimeter," Nucl. Instrum. Meth. A **307**, 254 (1991).

[49] S. Jin and J.L. Rosen, "E835 Neutral Trigger," E835 Internal Memo.

[50] T. A. Armstrong *et al.* [Fermilab E760 Collaboration], "Two body neutral final states produced in anti-proton - proton annihilations at 2.911 GeV$\leq \sqrt{s} \leq$3.686 GeV," Phys. Rev. D **56**, 2509 (1997).

[51] M. Obertino, "Studio dei decadimenti dello sato $^3P_0$ (χ_{c0}) del charmonio: $\chi_{c0} \rightarrow J/\psi\gamma \rightarrow e^+e^-\gamma$ $\chi_{c0} \rightarrow \gamma\gamma$ nel'ambito dell/esperimento E835 del Fermilab," PhD Dissertation, Universita delgi Studi di Torino, Italia, (2001).

[52] J. Kasper, "Search for Two Omega Meson Decays of Charmonium Resonances Produced in Proton-Antiproton Annihilations," PhD Dissertation, Northwestern University, (2002).

[53] M. Graham, "Measurement of the Two-Photon Decay Width of the χ_{c0}," PhD Dissertation, University of Minnesota, (2002).

[54] The CERN API Group, "GEANT-Detector Description and Simulation Tool," http://wwwinfo.cern.ch/asd/geant/.

[55] W.E. Burcham and M. Jobes, "Nuclear and Particle Physics," Longman Group Limited, (1995).

[56] P. R. Bevington and D. K. Robinson, "Data Reduction and Error Analysis for the Physical Sciences," McGraw-Hill, Inc. (1992).

[57] S. Bagnasco *et al.* [Fermilab E835 Collaboration], "New Measurements Of The Resonance Parameters Of The $\chi_{C0}(1^3P_0)$ State Of Charmonium," Phys. Lett. B **533**, 237 (2002).

[58] T.K. Pedlar, "A Study of Two Photon Decays of Charmonium Resonances formed in Proton-Antiproton Annihilations," PhD Dissertation, Northwestern University, (1999).

[59] C. Patrignani, "On the particle data group evaluation of chi/c(1P) and psi'(2S) branching ratios," Phys. Rev. D **64**, 034017 (2001) [arXiv:hep-ex/0104003].

[60] S. Bagnasco *et al.* To be published.

[61] M. Anselmino, R. Cancelliere, and F. Murgia, "Mass corrections to "forbidden" charmonium decays: $\eta_c, \chi_{c0} \rightarrow p\bar{p}$," Phys. Rev. D **46**, 5049 (1992)

[62] V. L. Chernyak and A. R. Zhitnitsky, "Exclusive Decays Of Heavy Mesons," Nucl. Phys. B **201**, 492 (1982) [Erratum-ibid. B **214**, 547 (1983)].

[63] G. T. Bodwin, E. Braaten and G. P. Lepage, "Rigorous QCD analysis of inclusive annihilation and production of heavy quarkonium," Phys. Rev. D **51**, 1125 (1995) [Erratum-ibid. D **55**, 5853 (1997)] [arXiv:hep-ph/9407339].

[64] P. Kroll, "Higher fock states and power counting in exclusive charmonium decays," Acta Phys. Polon. B **29**, 2789 (1998), [arXiv:hep-ph/980747].

[65] S. M. Wong, "Color octet contribution in exclusive P-wave charmonium decay," Nucl. Phys. Proc. Suppl. **93**, 220 (2001) [arXiv:hep-ph/0009016].

[66] T. Vidnovic III, P. Rumerio, "E835′ Neutral DST Format and Production Streaming," E835 Internal Memo.

[67] T. Vidnovic III, "NDST Efficiency in the $\pi^0\pi^0$ Analysis," E835 Internal Memo.

[68] M. Jacob and G. C. Wick, "On The General Theory Of Collisions For Particles With Spin," Annals Phys. **7**, 404 (1959) [Annals Phys. **281**, 774 (2000)].

[69] J. D. Richman, "An Experimenter's Guide To The Helicity Formalism," CALT-68-1148.